

PALEOSEISMOLOGY OF THE AKATORE FAULT, EAST OTAGO

Briar Taylor-Silva



A thesis submitted for the degree of
Master of Science
at the University of Otago, Dunedin,
New Zealand

April 2017

ABSTRACT

My thesis documents the first-ever paleoseismic trench investigation of the Akatore Fault, which has long been considered the most active fault to exist near Dunedin City. Two trenches were excavated across the fault in order to investigate the late Quaternary activity (timing, magnitude and recurrence of large ground rupturing earthquakes).

Trenching investigations at Big Creek and Rocky Valley have concluded that there have been three ground-rupturing earthquakes in the Holocene. An antepenultimate event has been constrained between $10,400 \pm 1,700$ and $1,326 \pm 22$ cal. yr BP, while, the penultimate and most recent events have been constrained between $1,326 \pm 22$ and 776 ± 22 cal. yr BP. These events resulted in 5 m of dip slip, hence 1 - 2 m of surface displacement per event, which may to have produced earthquakes with moment magnitudes 6.8 - 7.4.

Further studies at Taieri Mouth provided information on the longer term behaviour of the Akatore Fault. We estimated only 2 – 3 m of scarp development since the 125 ka marine terrace was formed. Since the Big Creek trench results indicated similar displacements achieved over three Holocene earthquakes, it is plausible that the scarp development has happened by way of these same three Holocene events. This would imply that there has been no activity along the Akatore Fault for a long period prior to these Holocene events i.e. little to no movement between 125,000 – 10,000 cal. yr BP. Furthermore, the Holocene slip rate along the Akatore Fault is significantly greater than the long term slip rate. This suggests the fault does not act in a characteristic fashion. It has an episodic / irregular behaviour. Similar behaviours have been determined for other Otago faults, which is problematic for forecasting future earthquakes. If inception of uplift along the Akatore Fault occurred ~1 Ma, the implied long-term slip rate is such that the fault may not yet have slipped enough in these Holocene events to accommodate the accumulated slip over the previous ~110 ka. The Akatore Fault needs to become the focus of a time-dependent seismic hazard calculation for Dunedin.

ACKNOWLEDGEMENTS

First and foremost I would like to thank my supervisors, particularly Mark Stirling. Your support and enthusiasm has been amazing, and knowledge invaluable. This has been an incredible project; thank you for being so patient with me and allowing me to be part of your work. Also, thanks to my co-supervisor Nicola Litchfield. I am inspired by your dedication to your work. Thank you for giving up your time for fault trenching and many emails to and fro. Your knowledge and previous research was key to this project.

Secondly, I would like to thank David Barrel for sharing all of his valuable knowledge and reviewing the trenches, also well as Ningsheng Wang and her team at the GNS Science who processed my radiocarbon and OSL ages.

Furthermore, I would like to acknowledge the land owners who allowed us to study the fault within their land; Kevin Duggan (Taieri Mouth), Joanne Davies (Rocky Valley) and the Fischli family (Big Creek).

Thanks to all of the staff from the Geology Department, University of Otago for being so kind and helpful. It's been great being part of the 'geology family'. Partially, Andrew Gorman, Hamish Bowman, Luke Easterbrook and Sebastian Clar who helped me at various stages of this project, as well as Sean Fitzsimons from the Geography Department, for allowing me to borrow his GPR equipment.

I've been lucky to have progressed through my degree with such a great group of peers and roommates. Particularly, Rebecca Parker she's been a great girl pal throughout the years. Also, the Otago University Canoe Club who were a great stress relief, taking me on incredible trips on the weekends.

Last but not least, I would like to thank my family and Joe for giving me tremendous support, emotionally and financially, throughout my whole time at university. Without them I wouldn't have gotten this far. You've all been amazing.

TABLE OF CONTENTS

ABSTRACT	i
ACKNOWLEDGMENTS	ii
TABLE OF CONTENTS	iii
FIGURES	vi
TABLES	ix
Chapter 1 INTRODUCTION	1
1.1 INTRODUCTORY REMARKS	2
1.2 FAULTS AND EARTHQUAKES	2
1.2.1 Global reverse fault rupture characteristics	7
1.3 REGIONAL GEOLOGY AND TECTONIC SETTING	12
1.3.1 Study area - SE Otago	15
1.3.2 Late Quaternary fault motion	19
1.4 AKATORE FAULT - PREVIOUS WORK	21
1.4.1 Onshore and offshore extent.....	21
1.4.2 Seismological investigations	22
1.5 REVIEW OF METHODS.....	24
1.5.1 Paleoseismic techniques	24
1.5.2 Dating techniques	30
1.6 AIMS AND OBJECTIVES	31
Chapter 2 PALEOSEISMOLOGY	33
2.1 INTRODUCTORY REMARKS	34
2.2 SITE SELECTION	34
2.2.1 Big Creek.....	36
2.2.2 Rocky Valley Creek	40
2.3 TRENCHING PROCEDURE	44
2.3.1 Excavating	44
2.3.2 Logging and sampling	47
2.4 TRENCH DESCRIPTION	52
2.4.1 Big Creek trench.....	53
2.4.2 Rocky Valley trench	60

2.5	RADIOCARBON AND OSL DATING RESULTS	63
2.5.1	Comparing OSL and radiocarbon ages with previous work	66
2.6	BIG CREEK HOLOCENE EVENT HISTORY	71
2.6.1	Pre event stratigraphy and age	71
2.6.2	Antepenultimate event	71
2.6.3	Penultimate event.....	72
2.6.4	Most recent event.....	73
2.6.5	Modern day	73
2.6.6	Comparison with Litchfield and Norris (2000)	73
2.7	GRAPHICAL SUMMARY OF HOLOCENE EVENTS	75
Chapter 3 FAULTED MARINE TERRACES AT TAIERI MOUTH		81
3.1	INTRODUCTORY REMARKS.....	82
3.2	MARINE TERRACES	83
3.2.1	Previous work	83
3.3	FIELD WORK	87
3.3.1	Site geomorphology.....	87
3.3.2	Geological observations.....	90
3.3.3	Magnetic Intensity	95
3.3.4	Ground penetrating radar (GPR).....	98
3.4	SUMMARY	107
Chapter 4 SEISMIC HAZARD IMPLICATIONS.....		109
4.1	INTRODUCTORY REMARKS.....	110
4.2	SUMMARY OF HOLOCENE EVENTS	111
4.3	RUPTURE CHARACTERISTICS	111
4.3.1	Single event displacement.....	112
4.3.2	Slip rate	112
4.3.3	Recurrence interval	116
4.3.4	Magnitude	118
4.3.5	Modified Mercalli Intensity (MMI)	119
4.4	COMPARISON WITH OTHER OTAGO FAULTS	121
4.5	SUMMARY	122

Chapter 5 CONCLUSIONS AND FUTURE WORK	123
5.1 PALEOSEISMOLOGY.....	124
5.2 SEISMIC HAZARD.....	124
5.3 FUTURE WORK	125
 REFERENCES	 126
 APPENDICES.....	 143
Appendix 1: Reference List for Table. 1.1	143
Appendix 2: Compiled trench photos	144
Appendix 3: OSL and Radiocarbon Reports	149
Appendix 4: Modified Mercalli Intensity Scale	172

FIGURES

Chapter 1

1.1	The rheology of the lithosphere with annotations of key geological and seismological features. Modified from Scholz (1988).....	3
1.2	Schematic representation of compressional stress, comparing normal (A), reverse (B), and strike-slip (C) faults. The three planes of pressure are at 90° to one another and include the, vertical stress direction, σ_v , and the two horizontal stress directions, σ_H and σ_h . The different magnitudes of stress include the principle (red + longest arrow), intermediate (yellow) and weakest (blue + shortest arrow). New Zealand fault examples and their rake values, λ , are given. Stress data from Lisle et al. (2006).	6
1.3	Plot of linear earthquake scaling relationships, illustrating the two Akatore fault ruptures. The yellow star corresponds to the minimum value (onshore portion only) and the red star, the maximum value (entire length). Data from Table.1.1. Fault width has been calculated based on an assumed seismogenic width of 12 km (Stirling et al. 2012)..	11
1.4	Tectonic setting of Otago, New Zealand A . Onshore known active faults in the South Island are marked in red (source: gns.cri.nz). B . A schematic diagram of the Alpine Fault ramp encompassing the Otago faults (modified from Stern and McBride, 1998). C . A profile of the Otago fault - fold belt (modified from Litchfield and Norris, 2000).	14
1.5	Study Area, North-East Otago. A . Regional geology, highlighting major faults. B . A topographic profile across the Akatore and adjacent faults showing their senses of motion. Modified from Bishop and Turnbull (1996) and Bull (2009).	17
1.6	The Akatore Fault onshore expression. Red arrows illustrate the fault's location (Digital terrain model from GNS Science).	17
1.7	Graphical representation of wave propagation principles used in ground penetrating radar and seismic reflection..	17
1.8	Illustration of cores collected on the downthrown side of a fault. Dammed sediments can provide information of past ground rupture events.	17
1.9	Simplified illustration of a magnetic intensity survey. The abrupt change in the magnetic intensity along the graph suggests a change in the underlying geology.....	17

Chapter 2

2.1	Location of sites along the Akatore fault and key transportation routes.....	35
2.2	View of Big Creek antecedent gorge (facing east). The Akatore Fault scarp is marked by stripes.....	37
2.3	View of the Akatore Fault scarp at Big Creek (facing north / perpendicular to the fault scarp). The fault scarp is marked by stripes.....	38
2.4	Annotated down core profile of an auger core collected on the footwall of the Akatore Fault at Big Creek.....	39
2.5	Lidar image of the Rocky Valley site. The Akatore Fault is clearly marked by the change in elevation from the south-west to the north-east of the image (Lidar image sourced from the Otago Regional Council). Lidar uses laser scanners to produce detailed 3d images of structures by measuring the distance between the object and the receiver (Glennie et al., 2013).....	41
2.6	View of Rocky Valley and the Akatore fault (in red), facing south-east. The fault is trace is not clear throughout the valley.....	42
2.7	View of Rocky Valley site facing east. The Akatore fault (in red) is not clear through the site.	43
2.8	Rocky Valley trench after excavation (facing south-east).	45
2.9	Folding lithology (red dashed lines) on the south wall of Rocky Valley trench.	45
2.10	Big Creek trench after excavation. The red dashed lines denote where the trench intercepts the Akatore fault. A. View of the trench looking east, perpendicular to the scarp. B. The Akatore fault on the south wall of the trench.	46
2.11	Big Creek trench divided into 1 x 1 m quadrants with important features highlighted. A. The different lithologies with coloured nails are being marked on the south wall in the image. B. View of the Akatore Fault (schist overlying sediments) on the north wall. Writing in orange corresponds to radiocarbon sample locations... ..	48
2.12	Preparing Rocky Valley trench for logging (facing south-west). A. on arrival the trench was completely filled with water. B. hours later, majority of the water was pumped from the trench and the south wall was divided up into 1 x 1 m quadrants.....	50
2.13	The coloured nails highlight the folding over of lithology on the southern wall of Rocky Valley trench.....	51
2.14	Collecting an OSL sample (BCK04) in the north wall of the Big Creek trench.	52
2.15	Legend for digitised trench logs at Big Creek and Rocky Valley sites.....	52
2.16	Graphical representation of Big Creek trench (north wall), during field work early March, 2016. Refer to Fig. 2.15 for legend.	55
2.17	Graphical representation of Big Creek trench (south wall), during field work early March, 2016. Refer to Fig. 2.15 for legend and Fig. 2.16 for unit descriptions previously described.....	57
2.18	The Akatore Fault exposure on a hill to the south of the Big Creek site.	59

2.19	Graphical representation of Rocky Valley trench (south wall), during field work early March, 2016. Refer to Fig. 2.15 for legend.	61
2.20	Comparison between Litchfield and Norris (2000) (orange) and our study's radiocarbon ages (blue) from the Akatore Fault.	68
2.21	Comparison between McKellar's gravel age (orange) and our study's OSL ages (blue) from the Akatore fault.	70
2.22	Schematic diagrams illustrating the tectonic evolution of Big Creek.....	76

Chapter 3

3.1	Location of the Taieri Mouth site along the Akatore fault (red).....	82
3.2	Sample locations and corresponding logs of Pleistocene terraces, <i>h</i> (larger numbers are associated with older terraces). Text in bold indicates the sample number. The red dashed line is the Akatore Fault.	86
3.3	Bird's eye view of the Taieri mouth site (original image sourced from Google Maps). A. The Taieri site with the Akatore Fault scarp annotated in red. B. The black box highlights where the fieldwork was conducted. The fault can be projected offshore (arrow) by the exposed schist outcrops. The schist outcrops and Taieri Island are on the hanging wall of the fault.	88
3.4	Close up of the distinctive ~ 2 m Akatore fault scarp at the Taieri mouth site. A. View is to the south. B. View is to the north.	89
3.5	A close up of the gritty, iron cement separating the loess (above) from the underlying (presumably Tertiary) sands.	91
3.6	Beach outcrop south of Taieri Mouth; GR: -46.07, 170.20, facing south-west. Key features are annotated on the log. "Fat Lamb" for scale.	92
3.7a	Loess and sands within road cuttings primarily on the east side of the fault (hanging wall), south of Taieri Mouth. The slope of the scarp can be observed in the skyline and the fault is annotated by black dashed lines.....	93
3.7b	Loess and sands within road cuttings on the west side of the fault (footwall), south of Taieri Mouth.	94
3.8	Magnetic survey lines which collected magnetic data over four days at the Taieri Mouth site. Data collected by students on the GEOL 261/361 field school and compiled by Hamish Bowman.	96
3.9	Annotated magnetic intensity results from the lines collected in Fig. 3.8 (above). The dark red and dark purple areas are associated with high and low magnetic anomalies, respectively.	97
3.10	The setup of our GPR survey. A 140 m long tape is laid out across the fault scarp and the paddles are placed 1 m apart.....	99
3.11	Lidar image of Taieri Mouth paddock. The fault scarp is well defined from the sudden change in elevation. The two GPR lines are annotated with black dots highlighting their extent. The lines were collected right (east) to left (west). The Lidar image is sourced from the Otago Regional Council.	100

3.12	GPR profile of the fault zone suggesting ~ 4 m of offset of the bedrock across the fault (assuming the deepest reflection on the hanging wall and footwall are from the top of the schist).....	102
3.13a	GPR Line 01 Profile with topography corrected. Exported from EkkoView. .	103
3.13b	Annotated diagram of GPR Line 01 profile (Fig. 3.13a), showing key features.	104
3.14a	GPR Line 02 Profile with topography corrected. Exported from EkkoView ..	105
3.14b	Annotated diagram of GPR Line 02 profile (Fig. 3.14a), showing key features	106

Chapter 4

4.1	Schematic diagram of the drainage patterns along the Akatore Fault (fault plane illustrated in red).....	114
------------	--	-----

TABLES

Chapter 1

1.1	Compilation of global reverse faults and their associated earthquake source parameters. References listed in Appendix 1..	9
1.2	Compiled paleoseismology data for Otago active faults.....	20
1.3	Advantages and disadvantages of paleoseismic techniques.....	29

Chapter 2

2.1	Big Creek and Rocky Valley radiocarbon ages from this study. Detailed reports are in Appendix 3.	64
2.2	Big Creek OSL ages from this study. Detailed report is in Appendix 3..	65
2.3	Litchfield and Norris (2000) radiocarbon ages along the Akatore fault.	67
2.4	McKellar (unpublished) radiocarbon age along the Akatore fault.	68

Chapter 3

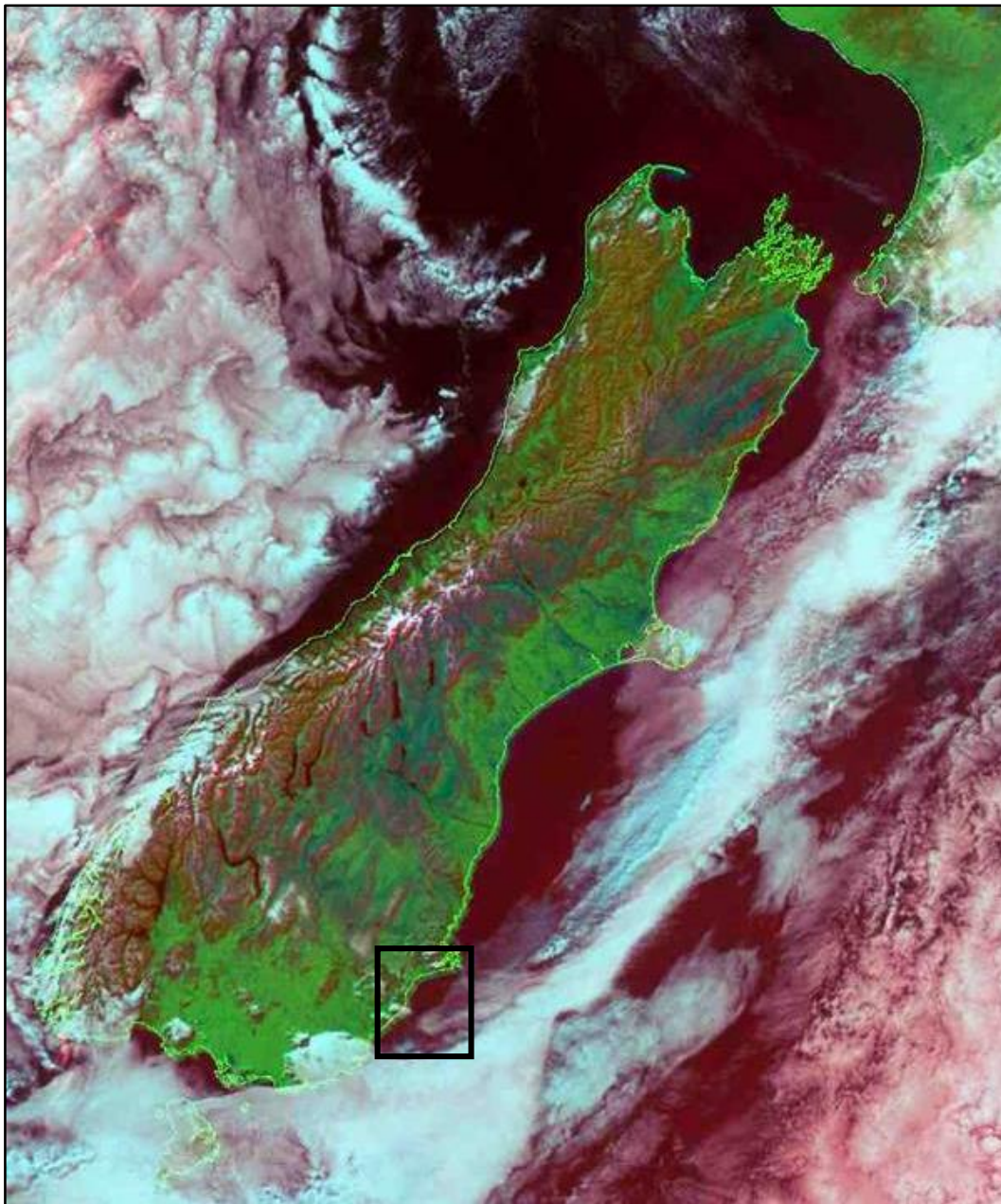
3.1	Luminescence ages of sands and loess south of Taieri Mouth, East Otago. Samples are in stratigraphic order... ..	85
------------	--	----

Chapter 4

4.1	Modified Mercalli Intensity Scale, VII- IX, for Dunedin (Murashev et al., 2006, Wood and Neumann, 1931). The complete MMI scale can be found in Appendix 4.	120
------------	--	-----

Chapter 1

INTRODUCTION



Study Area

Source: Landcare Research Ltd 2012

1.1 INTRODUCTORY REMARKS

The present work has been undertaken to assess the timing and occurrence of Holocene earthquakes on the Akatore Fault, East Otago, and the hazard it poses to Dunedin City and elsewhere. In this introductory chapter, I have introduced the basic foundations of faults and reverse rupture characteristics. Next, I have described the regional geology and tectonic setting of the study area. Finally, I have reviewed previous work and paleoseismic methods, followed by the aims and objectives of this study.

1.2 FAULTS AND EARTHQUAKES

Fault zones are features of the Earth's lithosphere that accommodate local deformation, they are associated with altered rheological properties relative to the host rock (Ben-Zion, 2008). These zones are generally constrained from surface expression, and most commonly occur in the active boundary zones of tectonic plates. When the build-up of strain across the fault plane becomes too great, energy is released as an earthquake (Yeats et al., 1997). This sudden motion generates seismic waves (earthquakes) which propagate outwards from the fault plane. Earthquake size is measured in units of magnitude (M), and a range of methods are utilised to develop different magnitude scales, such as the Richter and moment magnitude. The Richter scale was developed in 1935 and is the basis of all magnitude scales (Richter, 1935). The Richter magnitude scale is a logarithmic curve of the amplitude of seismic waves recorded by a seismograph (Boore, 1989). Moment magnitude was developed in the 1970's and succeeded the Richter scale (Hanks, 1979). Moment magnitude (M_w) is a magnitude scale that is derived from the seismic moment (M_o) of an earthquake, it is a measure of energy released during an earthquake. The following equation (Eq. 1.1) by Kanamori and Anderson (1975), provides an estimate of seismic moment from the rupture dimensions (L and W), rupture displacement (D), and rigidity modulus (μ) of the faulted rock mass.

$$M_o = \mu LWD \quad (1.1)$$

The depth at which earthquakes initiate, the hypocentre, is a function of temperature, pressure and rock type. The majority of crustal earthquakes occur in the upper crust, where rocks have brittle “stick-slip” behaviour. In the mid crust, the rock strength decreases with increasing temperature and the material transitions from brittle to ductile behaviour (Fig. 1.1; Yeats et al., 1997). This transition is dependent on the geothermal gradient and lithology, it usually occurs around a depth of 15 km and defines the base of the seismogenic (earthquake) layer. The seismogenic zone is where deformation occurs by frictional sliding, while the deeper ductile layer is where deformation occurs by plastic flow (Scholz, 1988). Large, destructive earthquakes typically nucleate at 10 – 15 km depth (Fukuyama, 2009). Earthquakes do not often nucleate in the upper 2 km of the crust; but are capable of rupturing to the surface in large events (Fig. 1.1; Scholz, 1988).

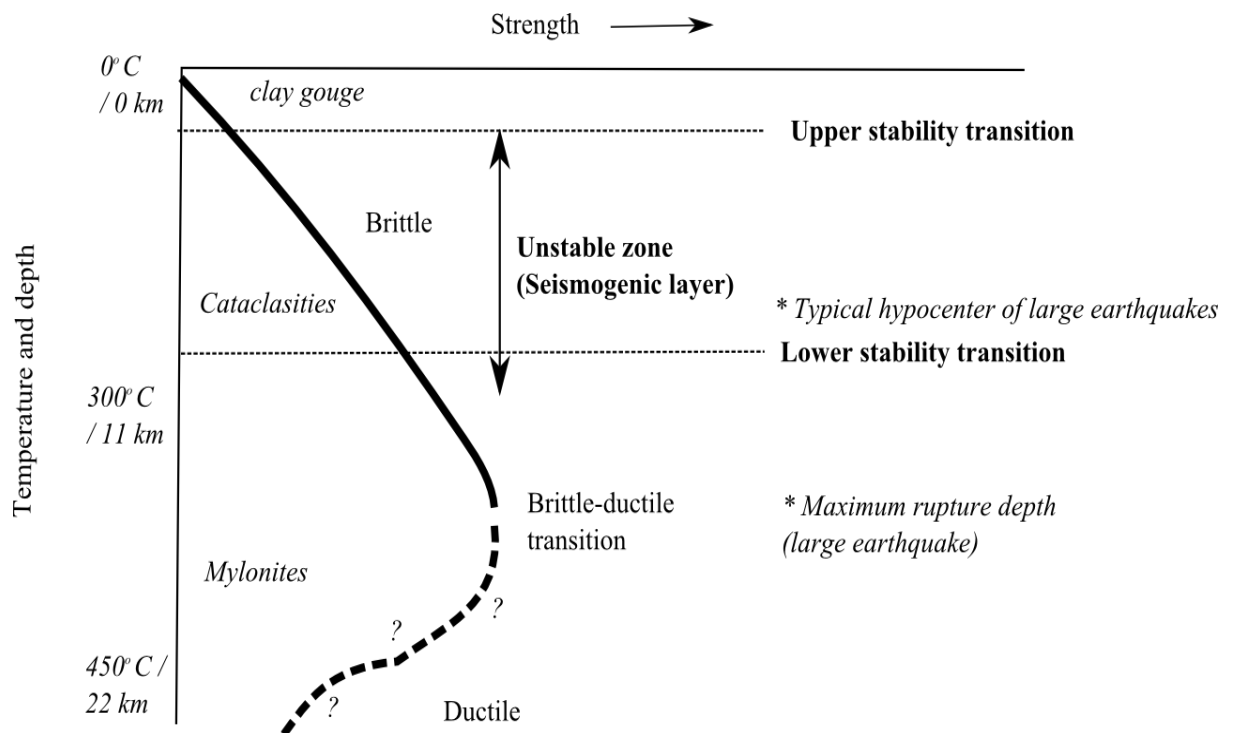


Fig. 1.1 The rheology of the lithosphere with annotations of key geological and seismological features. Modified from Scholz (1988).

During a large earthquake, a fault will generally produce displacement at the Earth's surface, and it is from the features of these displacements that the different types of faults can be recognised. There are three primary types of faults, normal, reverse and strike-slip; each of these faults has developed from different physical conditions. These can be characterised mathematically as “any system of forces, acting within a rock, resolves itself at any particular point into three pressures or tensions, acting across three planes which are at right angles to one another” (Anderson, 1951). The three principle compressional stresses can be defined as the principle vertical stress (σ_v) and the principle horizontal stress which is in two directions (σ_H, σ_h ; Lisle et al., 2006). The resulting fault motion is a function of the magnitude and direction of applied principle stress, this is shown in Fig. 1.2.

Reverse faults are recognised by their characteristic displacement, which is uplift of the hanging wall relative to the footwall (Fig. 1.2B). The hanging wall is the block on top of the fault which forms an acute angle with the ground surface, while the footwall forms an obtuse angle with the ground surface (Oglesby et al., 1998). This movement results from the principle compressional stress in the horizontal direction. When the pressure becomes too great the fault will release energy by rupturing, moving in the direction of the least resistance, which in the case of reverse faults is the vertical direction. Reverse faults occur in compressional settings; they are often accompanied by broader folding. Folding is common within unconsolidated deposits and shallow dips (McCalpin, 2009). Reverse faults dip at angles less than 90° ; common dip angles are between 25° to 35° and 45° to 55° , the latter are more common for reactivation of former normal faults (Sibson and Guoyuan, 1998). When reverse faults dip at or less than 45° they can be classified as a thrust fault. In this thesis for simplicity or unless specified, reverse faults refer to reverse and thrust faults.

An example of an historical reverse fault in New Zealand is the White Creek Fault, which ruptured during the M7.8, 1929 Murchison Earthquake. The maximum surface displacement of the rupture was 2.5 m (Berryman, 1980; Yeats et al., 1997).

Normal faults are characterised by the opposite sense of movement to reverse faults, a rupture produces movement in the horizontal direction and the footwall is uplifted relative to the hanging wall (Fig. 1.2A; Anderson, 1951; Yeats et al., 1997). They usually

occur in extensional settings, and generally have steeper dip angles than reverse faults. An example of an historical normal fault in New Zealand is the Edgecumbe Fault which ruptured during the M6.5, 1987 Edgecumbe Earthquake. The maximum surface displacement of the rupture was 3.1 m (Beanland et al., 1989).

Strike-slip faults are the third major type of fault. Strike-slip faults can take place in a variety of tectonic settings, but they occur mainly in zones of translation, transtension and transpression (Yeats et al., 1997). These faults dip sub-vertically and the movement is wholly or dominantly horizontal (Fig. 1.2C). Strike-slip faults can be further classified depending on the direction of horizontal motion. Strike-slip faults with left lateral motion are named sinistral, while those with right lateral motion are named dextral. An example of a major recent strike-slip earthquake is the M7.1 2010 Darfield earthquake, caused by rupturing of the Greendale Fault. Maximum displacements were ~5 m horizontally (dextral) and ~1.5 m vertically (Gledhill et al., 2011; Quigley et al., 2012).

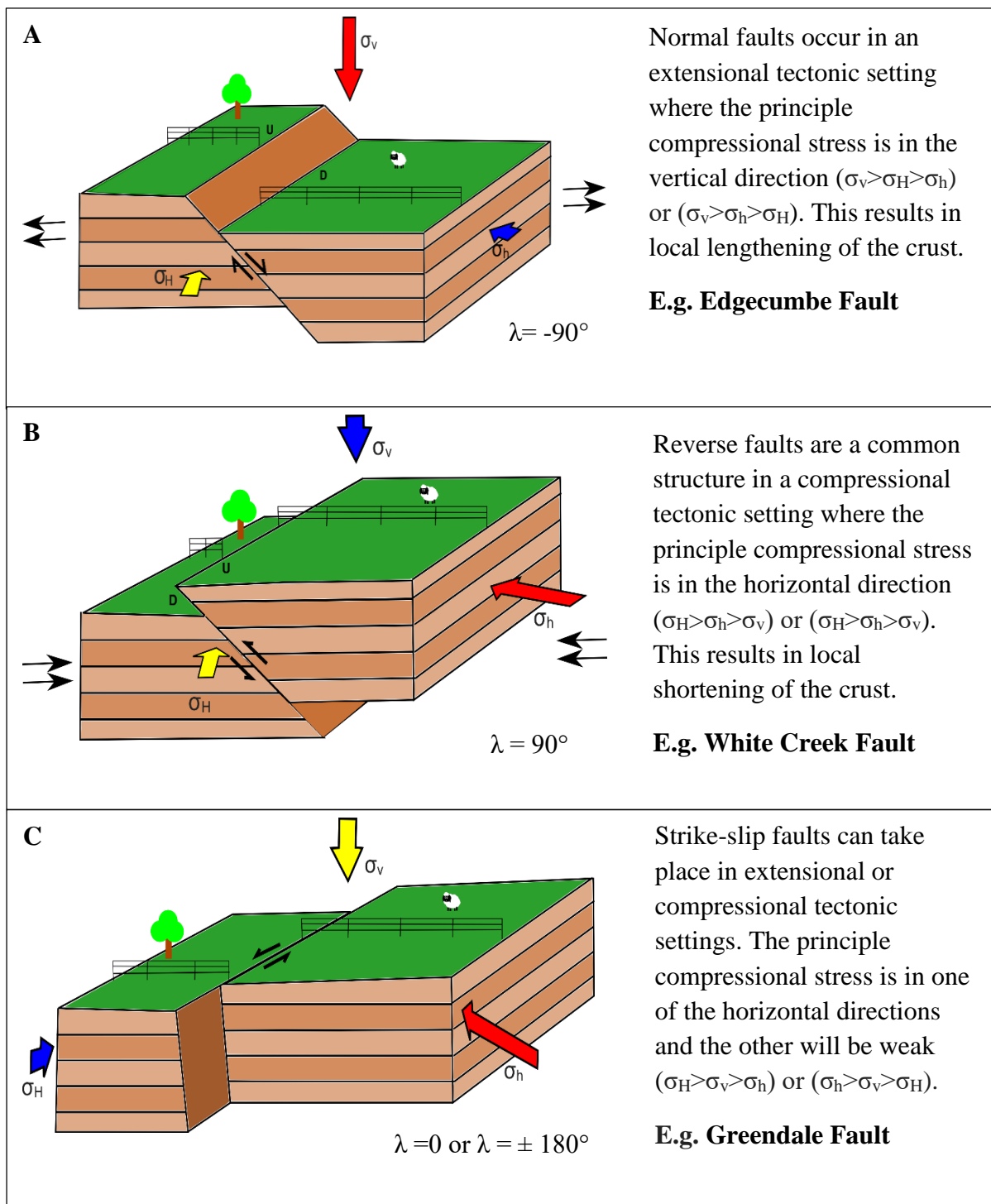


Fig. 1.2 Schematic representation of compressional stress, comparing normal (A), reverse (B) and strike-slip (C) faults. The three planes of pressure are at 90° to one another and include the vertical stress direction, σ_v , and the two horizontal stress directions, σ_H and σ_h . The different magnitudes of stress include the principle (red + longest arrow), intermediate (yellow) and weakest (blue + shortest arrow). New Zealand fault examples and their rake values, λ , are given. Stress data from Lisle et al. (2006).

1.2.1 Global reverse fault rupture characteristics

Earthquake hazard and risk models are key to reducing fatalities and damage; however the way earthquakes are initiated is poorly understood, large and very destructive earthquakes can occur without warning (Fukuyama, 2009). Observation of the characteristics of historical fault ruptures can be used to determine the possible behaviour of future events. I have compiled data for past worldwide reverse fault ruptures in Table.1.1 in order to understand the range of rupture lengths and associated displacements that characterise reverse faults, and to give my paleoseismic studies of the Akatore Fault greater context. The earthquake rupture data comes from earthquakes in thrust belts (e.g. Algeria, 1980), collision zones between continental boundaries (e.g. Iran, 1978), transform boundaries (e.g. California, 1971), and from stable continental areas (e.g. Australia, 1979 & 1988; McCalpin, 2009). The global earthquake rupture data shows that an earthquake typically must have a moment magnitude (M_w) greater than about 6 in order to rupture to the ground surface (Yeats et al., 1997). The magnitude of recorded ruptures on reverse faults range between M_w 6 and 7.9 (Table.1.1). The majority of the faults are thrust, with an average dip of 35° . Reverse faults often develop from low angle dips since the main compressional stress is in the horizontal direction. Furthermore, reverse faults undergo greater ground motion and fault weakening if they rupture at shallow dip angles (Oglesby et al., 1998; Oglesby et al., 2000).

The average slip on a reverse fault rupture is about 2 m, however the data compiled in Table.1.1 shows that slips ranging from 0.13 to 5.5 m are common. However, the average value is not particularly useful, as the slip on reverse faults are often irregular and they show 50% more variability than normal and strike-slip faults. Part of this irregularity may be from the complex interaction between folding and faulting (McCalpin, 2009). While the slips on reverse faults are irregular, the compilation of reported values still provides a range that can be used in assessing the reliability of future slip data. Furthermore, relationships between slip and other rupture information can be useful for assessing future seismic hazard. I have used the dataset from Table.1.1 to estimate the likely displacements that would be expected for ruptures along lengths similar to the Akatore Fault.

Specifically, the length of the onshore portion of the Akatore Fault is ~22 km; this is the minimum length of the active fault. If the onshore portion of the fault ruptured on its own, our data (Table 1.1) shows that we can expect a resulting average slip of ~1 m (Fig. 1.3). Assuming the fault extends ~62 km from Kaitangata, in the south to Kaikorai Estuary in the north, our data shows that a rupture of this length would result in an average slip of ~2 m (Fig. 1.3). These expected displacements have been used later in the thesis to interpret my trench data.

Table. 1.1 Compilation of global reverse faults and their associated earthquake source parameters. References listed in Appendix 1.

#	Date	Earthquake & Location	Hypocentre (km)	Moment Magnitude	Seismic Moment ($\times 10^{19}$ Nm)	Rupture Length (km)	Rupture Width (km)	Average Slip (m)	Maximum Slip (m)	Strike	Dip	Rake
1	3/07/2015	Pishan, China	8.00	6.40	0.61	22.10	10.10	0.20	0.89	114.00	25.00	97.00
2	25/04/2015	Gorkha, Kathmandu	15.00	7.90	77.00	130.00	80.00	5.50	7.50	287.00	7.00	98.70
3	31/10/2014	Rueisuei, Taiwan	14.98	6.36	0.34	30.00	30.00	0.13	0.56	205.00	42.00	57.00
4	18/08/2014	Mormori, Iran	7.00	6.20	0.35	27.00	19.00	0.20	0.60	304.00	29.00	101.00
5	20/04/2013	Lushan Earthquake	16 \pm 2	6.66	1.01	35.00	16.00	0.25	1.50	209.00	44.00	91.00
6	28/10/2012	Haida Gwaii	15.90	7.80	69.00	150.00	30.00	3.30	7.70	317.10	18.50	103.30
7	23/10/2011	Van, Turkey	16.00	7.10	6.10	70.00	40.00	1.85	3.5 - 4.5	241.00	51.00	58.00
8	10/09/2008	Qeshm Island, Iran	6.00	6.20		10.00	6.00	0.90	0.90	34.00	50.00	55.00
9	12/05/2008	Wenchuan, China	19.00	7.90	120.00	285.00	30.62	5.13	10.30	229.00	33.00	141.00
10	27/11/2005	Qeshm Island, Iran	6.10	6.00	0.13	9.00	3.00	1.70	1.70	73.00	36.00	66.00
11	8/10/2005	Kashmir	5-15	7.60	24.00	100.00	30.00	5.10	9.60	331.00	31.00	108.00
12	21/03/2003	Zemmouri, Algeria	8.00	6.80	2.80	54.00	15.00	0.55	0.75	54.00	50.00	90.00
13	26/01/2001	Gujarat, India	22.00	7.60	36.00	25.00	15.00	3.00	12.40	82.00	51.00	77.00
14	26/01/2001	Bhuj, India	23.00	7.70	36.00	75.00	22.50	2.50	8.50	82.00	51.00	77.00
15	21/09/1999	Chi-Chi, Taiwan	8.00	7.60	18.00	72.00		2.00	7.50	20.00	30.00	85.00
16	17/01/1994	Northridge, California	17.50	6.70	1.30	16.00	22.50	1.30	3.20	122.00	40.00	101.00
17	22/01/1988	Tennant Crk, Australia	8.00	6.60	1.10	30.00		1.00	2.50	100.00	40.00	85.00
18	10/10/1980	El Asnam, Algeria	12.00	7.10	2.50	27.00	14.00	2.20	6.50	210.00	50.00	82.00
19	2/06/1979	Cadoux, Australia	6.00	6.10	0.20	28.00	12.00	0.60	2.40	166.00	26.00	71.00
20	16/09/1978	Tabas, Iran	<20	7.09	13.00	85.00	23.00	2.25	3-3.5	332.00	31.00	114.00
21	6/03/1976	Friuli, Italy	7.00	6.50	0.57	18.50	11.20	0.33	0.50	288.00	29.00	112.00

Table. 1.1 Continued.

#	Date	Earthquake & Location	Hypocentre (km)	Moment Magnitude	Seismic Moment ($\times 10^{19}$ Nm)	Rupture Length (km)	Rupture Width (km)	Average Slip (m)	Maximum Slip (m)	Strike	Dip	Rake
22	6/09/1975	Lice, Turkey	15-25	6.70	7.40	26.00	13.00	0.50	0.63	72.00	15.00	-
23	9/02/1971	San Fernando, Ca	12.00	6.70	1.00	15.00		0.95	2.50	67.00	52.00	72.00
24	1/12/1945	Mikawa, Japan	10.00	6.60	1.00	20.00	15.00	1.10	2.10	135.00	30.00	65.00
25	7/12/1944	Tonankai	30.00	7.90	100.00	140.00	80.00	3.00	4.40	225.00	15.00	79.00
26	31/08/1896	Rikuu, Japan	15.00	7.20	8.20	37.00		3.50	8.80	-	45.00	-

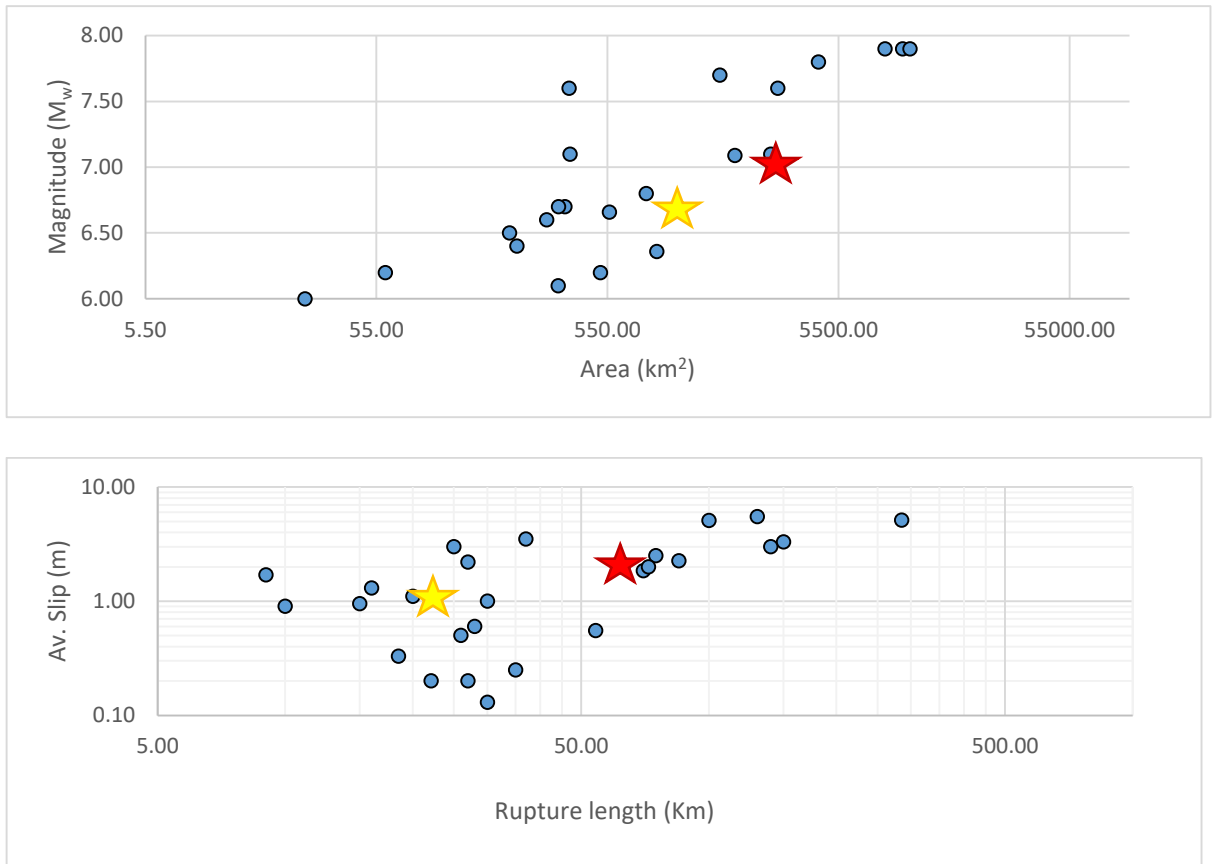


Fig. 1.3 Plot of linear earthquake scaling relationships illustrating the two Akatore Fault ruptures. The yellow star corresponds to the minimum value (onshore portion only) and the red star, the maximum value (entire length). Data from Table.1.1. Fault width has been calculated based on an assumed seismicogenic width of 12 km (Stirling et al. 2012).

1.3 REGIONAL GEOLOGY AND TECTONIC SETTING

The tectonically active Southern Alps lie in the South Island of New Zealand; they are a 700 km long mountain belt that currently show uplift rates of 5 mm / yr (Molnar et al., 2007). Rocks are being actively exhumed from a 20 - 25 km depth (Stern and McBride, 1998). The Southern Alps rise over 3000 m and create a barrier against the predominantly westerly winds, influencing the regions precipitation patterns. This results in up to 12 m per year of rain on the west coast of the South Island and only 1 m to the east of the Alps (Griffiths and McSaveney, 1983; Koons, 1990). The landscape here evolves rapidly, and weathering of the Southern Alps provides more than 4,000 tonnes k^2 per year of sediment (Bull, 2009).

The Southern Alps mark the transpressive continental boundary between the Australian and Pacific plates, with the principal element of the plate boundary being the Alpine Fault (Davey et al., 1998; Norris and Cooper, 2001). The present rate of plate motion in the central South Island is 37 mm/ yr Wallace et al. (2007). Motion before 6.4 Ma was predominantly strike-slip, however after 6.4 Ma the motion transformed to oblique compressional movement. Since 6.5 Ma, 230 km of dextral strike-slip motion and 90 km of shortening has occurred along the fault (Walcott, 1998). The Alpine Fault zone dips to the south-east at about 40°, producing steep topographic gradients in the west and more gradual gradients in the east (Fig. 1.4; Davey et al., 1998; Norris et al., 1990). The Alpine Fault accommodates 60 - 70% of the relative plate motion between the Pacific and Australian plates. The rest is primarily distributed to the east, in a 200 km wide area which includes the entire Otago region (Fig. 1.4; Norris, 2004; Norris et al., 1990). Within this region lies the Otago fault-fold belt, which is an imbricate system of parallel reverse faults, trending north-east (Barker, 2005; Beanland and Berryman, 1989; Jackson et al., 1996; Norris, 2004). The Otago fault –fold belt is thought to be a zone of back thrusting to the east of the Alpine Fault, and is interpreted to control the extent of the Otago reverse fold-fault province (Norris, 2004). Associated faults accommodate several mm/yr of oblique convergence (Jackson et al., 1996). These faults uplift Tertiary sediments which overlie an erosion surface, named the Waipounamu Erosion surface, also known as the Otago Peneplain (Landis et al., 2008). This erosion surface is a sub-

horizontal regional unconformity between basement rock, schist, and overlying diachronous Cretaceous - Tertiary marine sediments (Landis et al., 2008; Markley and Norris, 1999). This surface signifies an extended period of time (Cretaceous - Miocene period) when erosion was the dominant process as a result of marine transgression and regression. In much of Otago, the terrestrial sediments have been eroded away, however, remnants are preserved in syncline and footwall blocks. The Haast Schist basement rock has been exposed throughout Otago, as a result of faulting and folding (Jackson et al., 1996).

The active faults of the Otago region are shown in Fig. 1.4. An active fault in New Zealand has been defined by Langridge et al. (2016) as “a fault that shows evidence of surface rupture or ground deformation within the last 125,000 years”. Many of the Otago region faults are blind thrusts, which dip towards the west with little surface expression except for large anticlinal mountain ranges (Landis et al., 2008; MacKenzie and Craw, 2005). The Southern Alps create a rain shadow over the East Coast of the South Island, which results in low rates of erosion; therefore the total deformation is often determined from interpreting uplift and deformation of the peneplain surface and associated drainage patterns (MacKenzie and Craw, 2005; Youngson, 2005; Jackson et al., 1996).

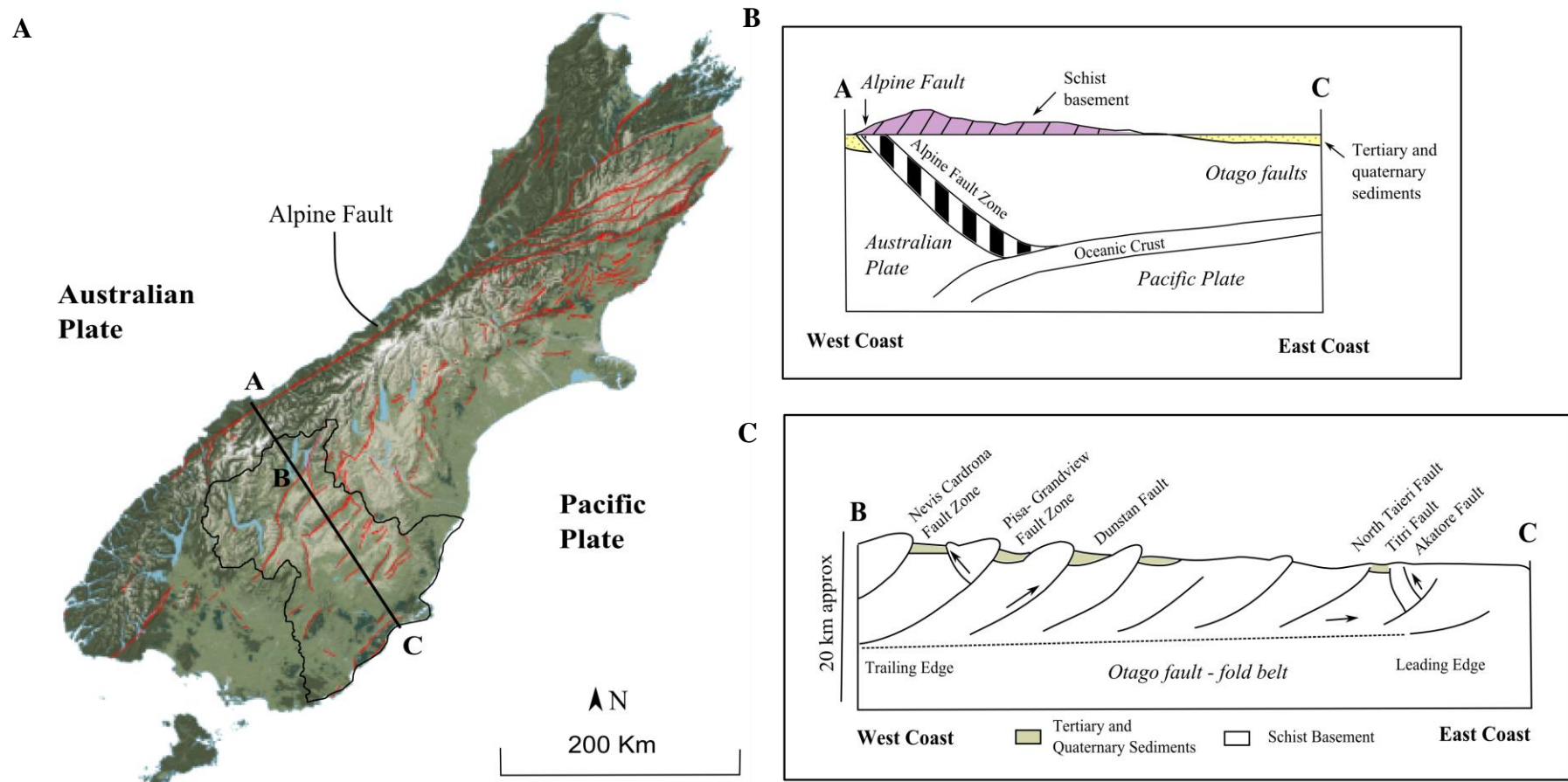


Fig. 1.4 Tectonic setting of Otago, New Zealand **A.** Onshore known active faults in the South Island are marked in red (source:gns.cri.nz) **B.** A schematic diagram of the Alpine Fault ramp encompassing the Otago faults (modified from Stern and McBride, 1998). **C.** A profile of the Otago fault - fold belt (modified from Litchfield and Norris, 2000).

1.3.1 Study area - SE Otago

This study focuses on an area located within south-east Otago. Most of the region has low relief, with hill country generally underlain by the Otago Schist (Fig. 1.5). These rocks range from non-schistose volcanoclastic sandstone and mudstone to the south-west, and strongly foliated and segregated schist to the north-east (Bishop and Turnbull, 1996).

In this region, mapped active faults include the Maungatua, North Taieri, Titri and Akatore Faults (Fig. 1.5). The Maungatua and North Taieri Faults have progressively uplifted the Maungatua Ridge on the west side of the Taieri Basin, and to the east, the Titri Fault and Akatore Fault have uplifted two ranges of coastal hills which slope gently to the east and steeply to the west (Bishop and Turnbull, 1996; Litchfield et al., 2002; Litchfield and Lian, 2004).

The Akatore Fault is the eastern-most onshore component of the Otago reverse fault-fold belt, it strikes north-east to south-west and dips 45° - 060° E/SE (Litchfield and Norris, 2000). The southernmost extent of the fault travels offshore near Measly Beach and splits into multiple strands near Wangaloa, before terminating near the Clutha River mouth, at the Castle Hill Fault Zone (Fig. 1.5). The fault is observed onshore between Taieri Mouth and Tokomairiro Mouth (~22 km) by the displacement of the subhorizontal peneplain surfaces (Fig. 1.6). Exposures of the fault are observed in road cuttings and within a Quarry near Big Creek (Litchfield and Norris, 2000).

Tertiary sediments have deposited along the downthrown side of the Akatore Fault. These sediments consist primarily of non-marine sands and gravels to the north-east and marine sands and silt to the south-west. South-west of Crystals Beach the peneplain is obscured by the Taratu Formation (Bishop and Turnbull, 1996), whereas to the north-east it is exposed. Rivers and creeks have cut through these hills, creating antecedent gorges at Akatore Creek, Big Creek, Bull Creek and Nobles Stream (Litchfield and Norris, 2000). Voluminous Quaternary alluvial terrace and flood plain deposits are found at the mouth of Tokomairiro and Taieri Rivers, comprising of loose sands and gravel, many of which are capped with loess. At Taieri Mouth a sequence of marine terraces are preserved along the coast (Bishop and Turnbull, 1996). The marine terraces appear to be

displaced across the Akatore Fault, based on the difference in terrace heights on east and west fault blocks (Litchfield and Norris, 2000).

Hills along the coastal range vary in elevation from 190 m around the centre onshore portion of the fault (e.g. Big Creek), to less than 50 m at the ends (e.g. Tokomairiro and Taieri Mouth). The maximum slip of dip-slip faults typically occurs in the centre of the fault and tapers towards the edges (Scholz, 2002). Towards the southern end of the Akatore Fault, near Tokomairiro Mouth, the fault scarp is poorly expressed. This may be due to the soft Taratu and Wangaloa Formations cover in the area, which would mute the fault expression. The fault may also break up into small strands with different strikes (north-south to south-west) as it transitions offshore in the vicinity of Tokomairiro Mouth (Johnstone, 1990; Litchfield and Norris, 2000).

In contrast, there is a distinctive fault expression from Nobles Stream to the north-east near Taieri Mouth. At the north-eastern end of the fault, south of Taieri Mouth, there is a ~ 2 m high scarp which is the last evidence of the fault before it strikes offshore. Offshore postglacial sediments are unconformably underlain by Cretaceous and Tertiary sediments. These sediments are faulted and folded from a sequence of offshore faults which trend parallel to the Otago faults (Johnstone, 1990).

The northern end of the fault has not been well constrained, however, it is observed in marine geophysical data approximately 15 km south of Dunedin, and may strike onshore near Kaikorai Valley, Dunedin (Bruce, 2010). The possible close proximity of the fault to the city means that it is considered to be Dunedin's most significant local seismic hazard (Glassey et al., 2003). The Dunedin Earthquake (M 5) in 9th April 1974 was centred only ~10 km south of Dunedin City at ~20 km depth; it is believed to have been the result of movement on the Akatore Fault or one of related parallel offshore faults (Adams and Kean, 1974; Bishop, 1974a).

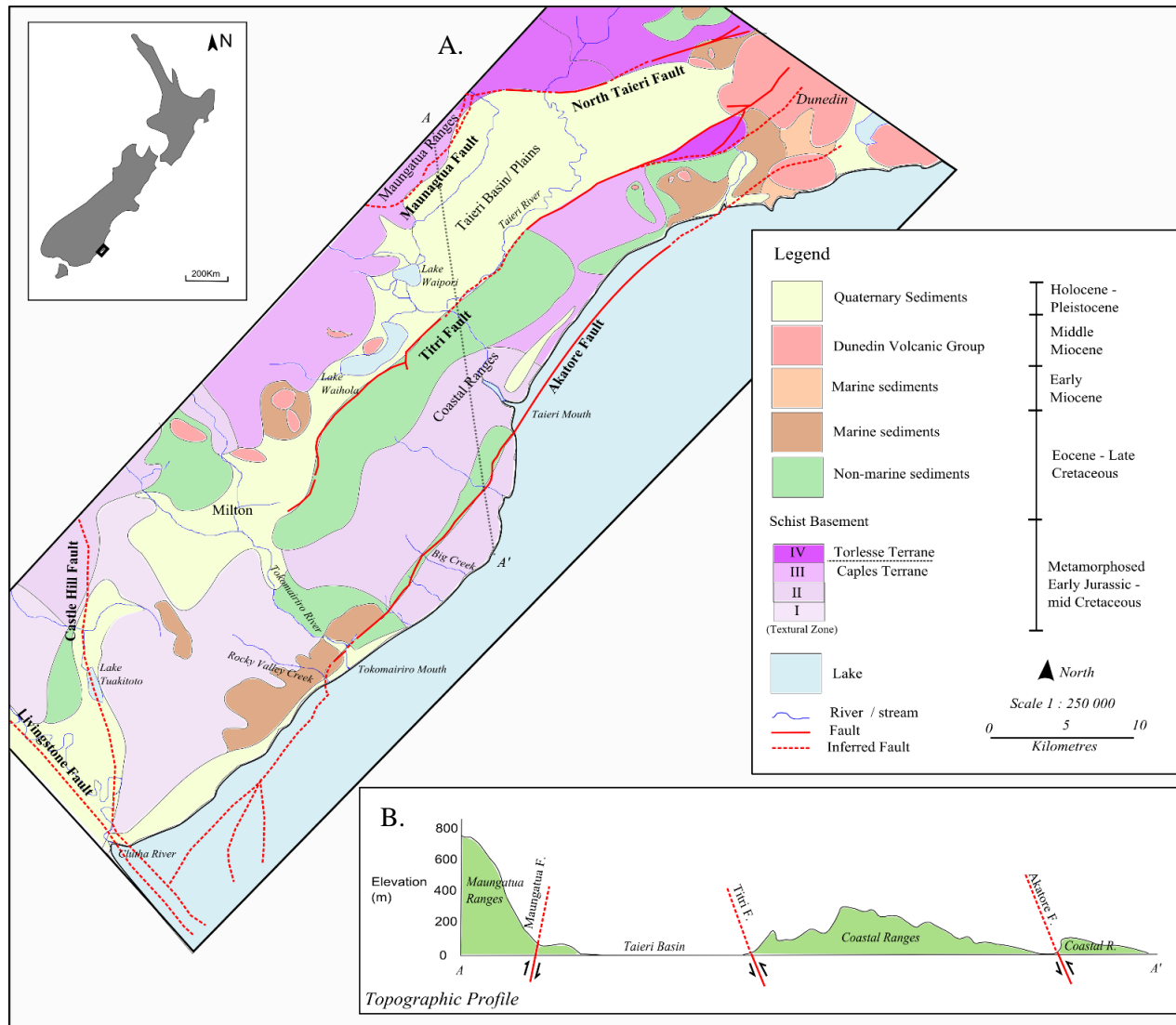


Fig. 1.5 Study Area, North-East Otago. **A.** Regional geology, highlighting major faults. **B.** A topographic profile across the Akatore and adjacent faults showing their senses of motion. Modified from Bishop and Turnbull (1996) and Bull (2009).

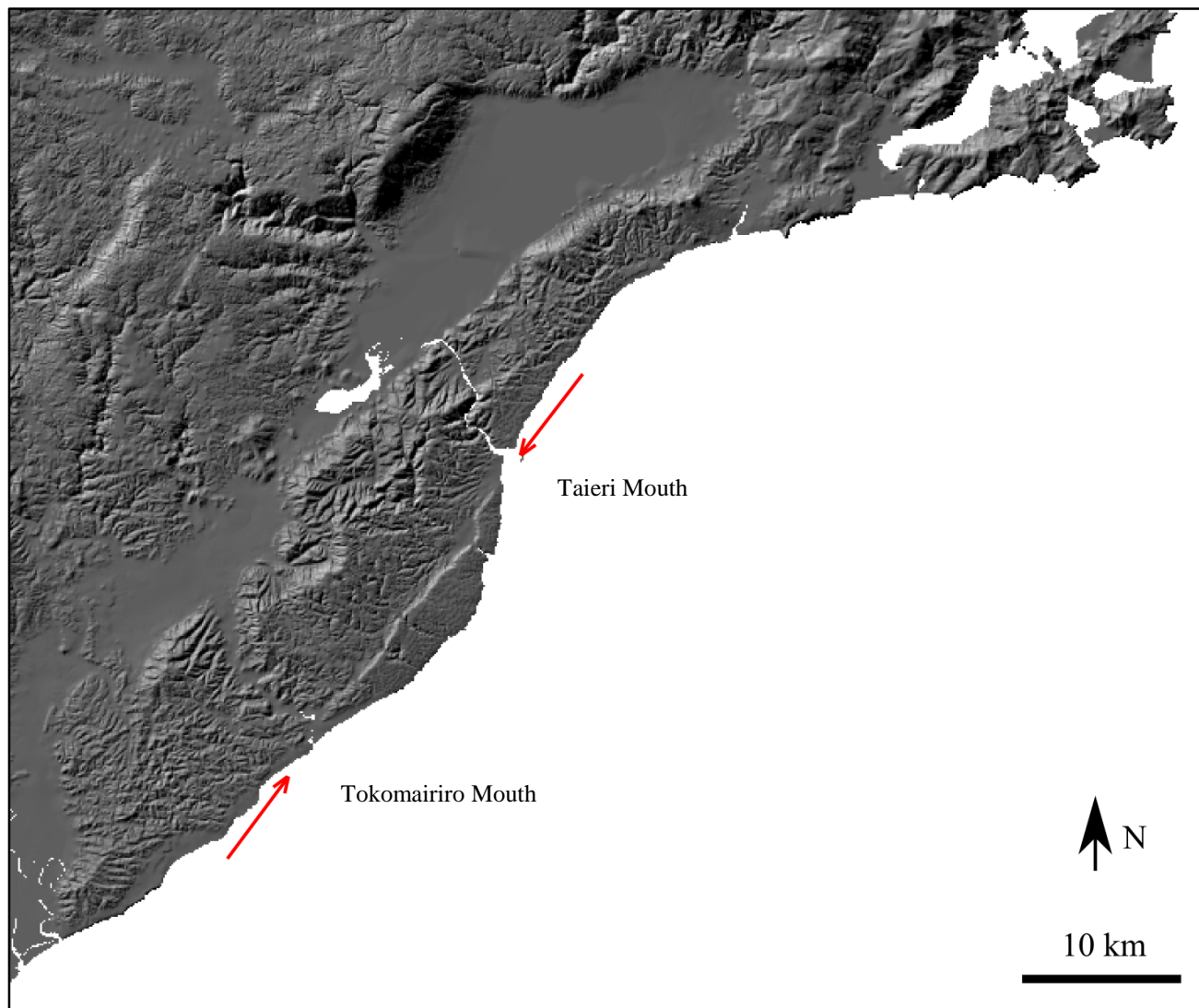


Fig. 1.6 The Akatore Fault onshore expression. Red arrows illustrate the fault's location (Digital terrain model from GNS Science).

1.3.2 Late Quaternary fault motion

The Late Quaternary faults of Otago are characterised by low slip rates, long recurrence intervals and low rates of historical seismicity (Anderson and Webb, 1994; Beanland and Berryman, 1989; Berryman and Beanland, 1991; Norris, 2004). Overall, Central Otago shows less than 5 mm per year of shortening across the Late Quaternary faults (Beavan and Haines, 2001; Jackson et al., 2002).

The Otago faults have an average length of 24 km and relatively steep dips, such as the $\sim 65^\circ$ dips which have been measured on sections of the Titri and Pisa Faults (Beanland and Berryman, 1989; Litchfield, 2001). Some of the Otago faults are shown to have been reactivated normal faults, which may explain the high dip values. Evidence of Cretaceous normal faults is often suggested by greywacke and semischist juxtaposed, which occurs along the St Bathans, Hawkdun and Kakanui Ranges (Bishop, 1974b; Markley and Norris, 1999). During the Quaternary, north-east striking mountain ranges throughout Otago have been uplifted, with an average vertical displacement of 1000 m, this has been measured from the offset of ranges from the Otago wide Waiponamu erosional surface (Landis et al., 2008; Norris, 2004).

The Otago faults show clear evidence of Late Quaternary activity from field mapping and paleoseismic investigations (Table.1.2); however, limited paleoseismic data is available to establish the behaviour of many of the Otago faults.

Table. 1.2 Compiled paleoseismology data for Otago active faults.

Fault	Length (km)	Recurrence interval	Slip rate (mm/ year)	Recent movement	Paleoseismic method	Reference
Pisa- Grandview Fault zone	-	20,000– 30,000	1	> 23, 000	Fault history was constrained through preserved glacial geomorphology features	(Beanland and Berryman, 1989)
Nevis -Cardrona Fault system	Continuous 10 km faults	<3600	-	< 10,000	Trenching and field mapping	(Beanland and Barrow-Hurlbert, 1988)
Dunstan Fault		8,000	-	< 23,000	Trenching and field mapping	Berryman, 1991 #248}
Akatore Fault	> 40	6000 - 12000	-	1150 – 1000 year	Coring of swamps and uplift of marine terraces	(Litchfield and Norris, 2000, Norris et al., 1994)
Hyde Fault	-	4000-5000	0.4-0.5	<14,000	Coring, seismic surveys , field investigation	(Norris et al., 1994)
South Rough Ridge Fault	20-30	6000 – 10,000	0.1 – 0.15		In situ cosmogenic ¹⁰ Be measurements in quartzites	(Jackson et al., 2002)
Titri Fault	58	-	-	Evidence for late Quaternary activity	Trenching	(D. Barrell, pers. comm.)

1.4 AKATORE FAULT - PREVIOUS WORK

The Akatore Fault was first identified by Benson (1935), he suggested there was evidence of crustal movement from landforms around coastal NE Otago, such as uplifted marine terraces, coastal cliffs and geological discontinuities. Since Benson's discovery, much work has gone into mapping the extent and assessing past movement along the Akatore Fault, encompassing many disciplines, such as geomorphology, paleoseismology, and archaeology (e.g. McFadgen, 2008). Investigating the Akatore Fault's seismic hazard potential has become of importance due to its close vicinity to populated areas, such as the Dunedin City, Milton and Balclutha.

1.4.1 Onshore and offshore extent

The Akatore Fault was named by Ongley (1939) who mapped the fault as extending 12 miles from the mouth of the Taieri River to Tokomairiro River. The Akatore Fault was initially mapped as a simple configuration with a south-west strike. It was noted by Ongley (1939) that the Akatore Fault is "clearly marked with steep escarpment on the east and gentle back slope of the inland block on the west". The ends of the fault were further constrained by McKellar (1966), where the entire onshore extent of the Akatore Fault was first published within a geological map of Dunedin.

Since then, it has been suggested by many authors, that the Akatore Fault strikes offshore to the south of Taieri Mouth. The offshore extent of the fault has not been well constrained as seismic reflection methods cannot be used to image in shallow waters, such as near Taieri Mouth (Bruce, 2010). Offshore investigations have been conducted by Johnstone (1990), later published by Gorman et al. (2013), who used high resolution sub-bottom profiled and side scan sonar images to map the Akatore Fault, 12 km offshore between Blackhead and Mitchells Point. In places, the fault has a clear surface expression where it offsets the sea floor. Johnstone (1990) discovered that once the fault extends

offshore, it follows parallel to the coast for some time, striking at 040 - 050°, before it bends back towards the shore, near Bruce's Rock. From here it may project back onshore north of the Kaikorai Estuary, where shallow dipping (15°) bedding in road cuttings at Waldronville may be interpreted as being faulted (Johnstone, 1990). This idea was also proposed by Robertson (1958) who suggested that the fault possibly strikes towards Dunedin along Kaikorai Valley.

Later, Bishop and Turnbull (1996) published a map of the 'Geology of the Dunedin Area' which contained the onshore and offshore extent of the Akatore Fault. The offshore material is provided by the Geology Department of Otago University, and is dashed with uncertainty (see Fig. 1.5). This is the most recently published map of the Akatore Fault. Later, however, Bruce (2010) and Gorman et al. (2009) revised the offshore extent by investigating the fault between Taieri Mouth and Blackhead using Boomer, CHIRP and side scan sonar data. Bruce (2010) determined that the Akatore Fault runs parallel to the coast 800 – 1000 m offshore near Taieri Mouth, south of Brighton it bends around and strikes offshore at 40° - 50°. Here it may be associated with the offshore Green Island Fault, therefore it may not propagate back onshore (Bruce, 2010).

1.4.2 Seismological investigations

In 1979, the 'Akatore Fault Monitoring Pattern' was established. It is one of many fault monitoring networks within New Zealand installed by New Zealand Geological Survey (NZGS) / Earth Deformation Studies (EDS) to monitor earth deformation, as past studies have indicated that elastic deformation occurs before large earthquakes (Blick, 1981; Brill, 1981; Farrier, 1990). The Akatore Fault was monitored due to its close vicinity to the city, and because the Dunedin earthquake on the 9th of April in 1974 (M5), is believed to have occurred on this fault or one of its associated offshore faults (Adams and Kean, 1974; Bishop, 1974a). The Akatore Fault was classified as Class 1 active, indicating it has a recurrence time of ≤ 2000 years; evidence has come from one to three metre high scarps along the fault (Brill, 1981). Since these early projects took place, multiple subsequent surveys have been carried out but little informative data has been retrieved due to measurement uncertainties (Farrier, 1990).

A report on the North East Otago faults was compiled by Norris et al. (1994) to assess the potential earthquake hazard in Dunedin. From field observations the fault was characterised as relatively young, generally striking NE-SW and dipping 60° E, and with a reverse sense of slip. They determine the total offset of the fault to be 120 - 130 m, which was measured from the Cretaceous erosion surface near Big Creek. The Akatore Fault was mapped from Taieri Mouth to Tokomairiro River mouth, where five cores were taken and radiocarbon dated. From these results, it is evident that at least two events have occurred since ~14,000 years BP, and the last event occurred ~1,200 years BP with an estimated single event displacement of ~2 m per event (Norris et al., 1994).

Later, Litchfield and Norris (2000) performed a comprehensive investigation of Holocene movement along the Akatore Fault. Along the fault, uplift has caused temporary blockage of the drainage along antecedent rivers. Blockage of the streams often causes a build-up of silt, clay and peat which can be dated and correlated to recent movement. Ten auger cores were collected from gorges along the fault and radiocarbon dates, along with the geomorphology of uplifted marine terraces, were used to interpret past fault activity. Results determined that the last event along the fault is constrained between 1,150 and 1,000 years BP and there has been no fault movement between 80 ka and > 3800 year BP (the penultimate event). The marine terraces suggested an average single event displacement of 3 m (Litchfield and Norris, 2000). These terraces have been dated by OSL dating by Rees-Jones et al. (2000) and Litchfield and Lian (2004). Their ages suggest that no activity has occurred on the Akatore Fault between 125 and 3.8 ka.

Since Litchfield and Lian (2004), few studies have been conducted on the Akatore Fault. Recently, Denys et al. (2016) analysed the geodetic data and found irregular velocities that have been measured in close vicinity to the Akatore Fault, which indicate contraction of about 1 mm/yr. Additional investigations were clearly required to further assess the activity and potential hazard of the Akatore Fault.

1.5 REVIEW OF METHODS

1.5.1 Paleoseismic techniques

Paleoseismology is a multidisciplinary science, which utilises geomorphology, sedimentology and stratigraphy to study the location, timing, geometry, and size of historical ground-rupturing earthquakes. This information can be used for earthquake forecasting by assessing the probability and severity of future seismic events, and increasing public awareness (Kondo and Owen, 2013; McCalpin, 2009; Štěpančíková et al., 2010; Van Arsdale, 2000). This section will evaluate several paleoseismology techniques for fault investigations that are common throughout the literature. These methods include subsurface imaging techniques, coring and drilling, fault trenching and magnetic intensity surveying. By assessing their advantages and disadvantages, the most suitable method can be selected for the site being study (Table. 1.3). Although these methods can be used in a variety of contexts this section will focus on their application to paleoseismology.

Seismic reflection (SR) and Ground Penetrating Radar (GPR) are two subsurface imaging techniques which are based on wave propagation principles. When an energy source is released reflected waves are recorded by the receivers. The difference in density between two layers changes the angle at which the wave reflects. The offset distances provides information on the underlying geology (Fig. 1.7). SR is a long established technique which provides high quality spatial resolution of geological features (Feng and McEvelly, 1983; Woodward and Sloss, 2013). It uses seismic waves at low frequencies to measure the variations in elastic properties of materials, such as pressure, composition and water content (Everett, 2013; Guéguen and Palciauskas, 1994; Hildebrand et al., 2002; McCalpin, 2009; Murray et al., 2005; Zoback et al., 2010). SR has been utilised on the San Andreas Fault Zone, California, to analyse the crustal structure, which requires a deep-imaging survey (Feng and McEvelly, 1983). GPR has gained popularity since the 1980s as it can accurately identify discontinuity and heterogeneity in the shallow subsurface (<10 m; Murray et al., 2005; Rashed et al., 2003). GPR uses electromagnetic waves at high frequencies to measure variations in dielectric properties of materials, such

as clay composition, water content and compaction (Everett, 2013; Hildebrand et al., 2002; Murray et al., 2005). For example, the Uemachi Fault in Japan, consists of alternating clay and sand layers which have strong differences in their dielectric properties making them ideal for GRP analysis (Rashed et al., 2003). Subsurface imaging is a common technique for identifying fault induced deformation of the strata such as, tilting, folding and fault block offset (McCalpin, 2009). They are mainly utilised for identifying displacement and orientation of dip-slip faults with high contrasts in the physical and chemical properties of the unit contacts, and when fault identification at depth is necessary (McCalpin, 2009).

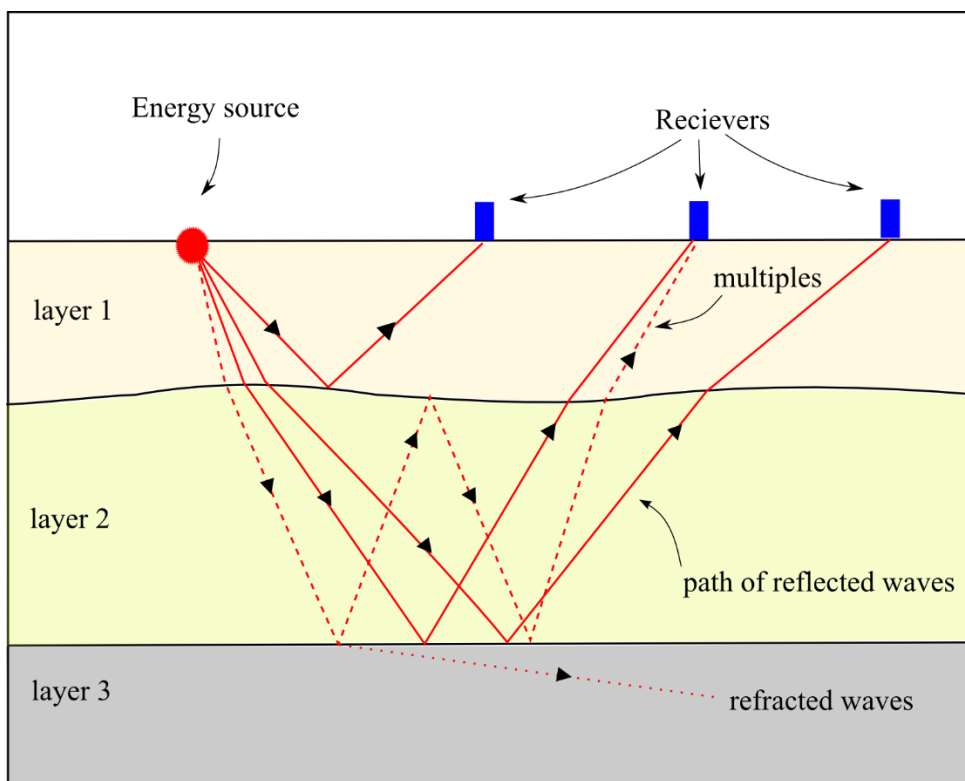


Fig. 1.7 Graphical representation of wave propagation principles used in ground penetrating radar and seismic reflection.

Drilling and coring are common techniques where a continuous sample is collected below the earth's surface by forcing a tube into sediment manually, e.g. hand augers, or mechanically e.g. vibra-coring (Woodward and Sloss, 2013). Once collected, strata can be correlated to tectonically induced sedimentation in a continuous core (Fig. 1.8). Coring and drilling are mainly utilised for gaining samples at great depths and in settings where other techniques are not practical (McCalpin, 2009). For example, the Hollywood

reverse fault and Compton blind thrust fault are underlying heavily urbanised areas in Los Angeles. Coring boreholes was the most practical option to gain information on the most recent movement (Dolan et al., 1997; Leon et al., 2009). Coring and drilling are particularly useful techniques in difficult water logged settings, where there are few other options. For example, Hubert-Ferrari et al. (2012) cored a sag-pond on the North Anatolian Fault and identified four past earthquakes from disturbed sedimentary sequences presumed to be caused by earthquake shaking.

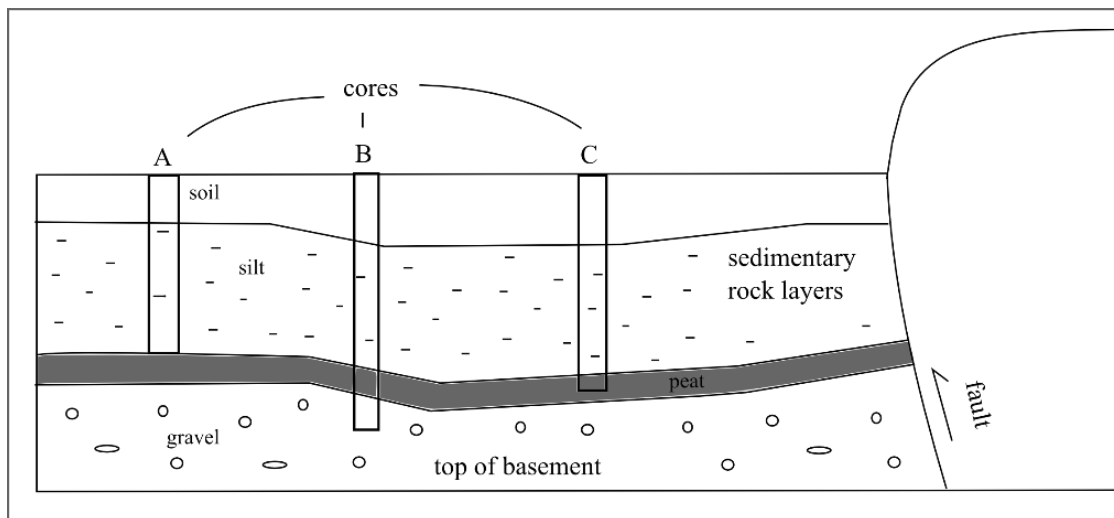


Fig. 1.8 Illustration of cores collected on the downthrown side of a fault. Dammed sediments can provide information of past ground rupture events.

Fault trenching is a more invasive technique which is commonly used in paleoseismology. Trenching involves excavating the ground across the path of an active fault to create near-surface geological exposures of the fault. The stratigraphy and deformation is mapped along the trench walls and often dated to constrain the paleoearthquake history, and hence recurrence information (McCalpin, 2013). The size of a trench can vary, although a bench must be created every few metres for accessibility and safety (McCalpin, 2009). Trenching is the most effective technique for near surface fault investigations as it gives a three dimensional view of a deformed zone, therefore providing an ability to see the relationships between sediments and faulting (McCalpin, 2009; Štěpančíková et al., 2010). A recent trenching study on the Alpine Fault by Berryman et al. (2012), involved trenching five sites along the trace of the Alpine Fault, New Zealand. The trenches were located on strath terraces and exposed evidence for the

most recent seismic events on the Fault. By trenching they were able to record the orientation of the fault, and determine that five events had occurred within the last 1,000 years, each event resulting in dextral displacements of up to 8 – 9 m and vertical displacements of 1 m (Berryman et al., 2012). However, in older surfaces, interpretations can be difficult, as a trench may show complex faulting such as cross cutting, inter-faulting and shearing. Younger events can obscure the older events and can make rupture events difficult to reconstruct (McCalpin, 2009).

A less commonly used method is a magnetic intensity survey. This technique is often used when locating structures prior to trenching (McCalpin, 2009). Surveys can be done aerially, for detecting large scale faulting (e.g. Grauch et al., 2001) or on the ground to detect smaller features using a magnetometer (e.g. Bailey, 1974). The magnetometer measures fluctuations in the earth's magnetic field, resulting from rocks with different magnetic properties (Fig. 1.9). High magnetic intensities are associated with materials with higher magnetic properties. An abrupt change in magnetic properties is often associated with a dip slip fault, where there is thickening of more magnetic, syntectonic sediments on the uplifted side. Magnetic surveys are effective at detecting faults as they are not limited by moisture and salinity, which effect GPR, however they can easily produce false signals due to metal objects in the vicinity of the survey (McCalpin, 2009).

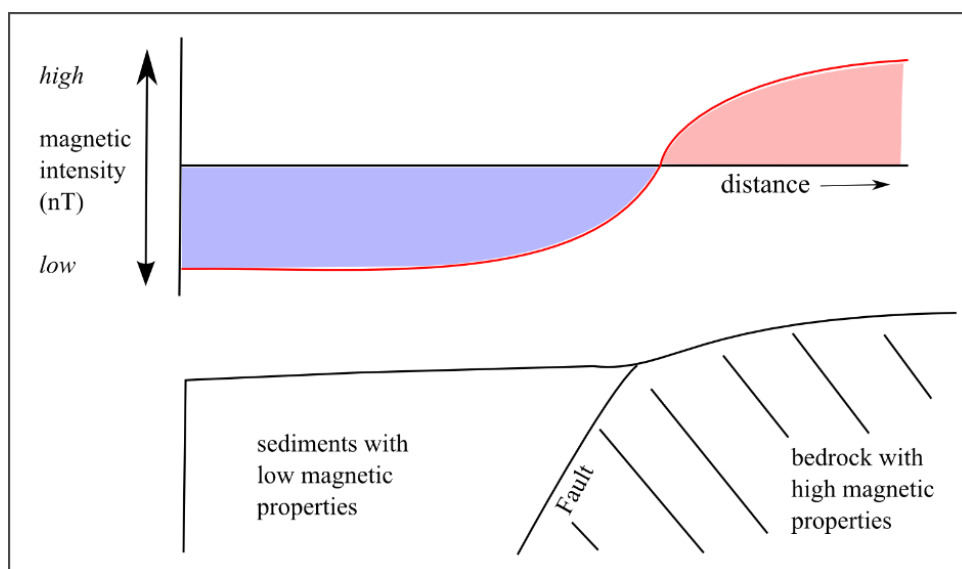


Fig. 1.9 Simplified illustration of a magnetic intensity survey. The abrupt change in the magnetic intensity along the graph suggests a change in the underlying geology.

Each of these techniques have their advantages and disadvantages in their application to paleoseismology. Using a combination of techniques is the most advantageous way to produce quality data, however circumstances (expense, limited equipment and time) do not always make this possible. In favourable site conditions, trenching is the best technique to gain more comprehensive and definitive information as it typically produces a 3D exposure of the fault. This generally leads to the least ambiguous of fault interpretations (Hatheway and Leighton, 1979).

Table. 1.3 Advantages and disadvantages of several paleoseismic techniques.

Technique	Advantages	Disadvantages
Subsurface imaging	<ul style="list-style-type: none"> • Detailed imaging of structural features in the subsurface • Fault identification at depth • Non-intrusive/ destructive • Time efficient • Easy to operate • Easy to transport 	<ul style="list-style-type: none"> • Expertise is required for processing and interpretation, which can be time consuming • Large amounts of data • Subsurface samples as often required for calibration • Data decays exponentially with distance from source
Reflection	<ul style="list-style-type: none"> • High resolution at depths >100 m 	<ul style="list-style-type: none"> • Cannot penetrate through inelastic layers • Need a large number of receivers and acquisition equipment • expensive
Ground Penetrating Radar	<ul style="list-style-type: none"> • High resolution in the upper subsurface (<10m) 	<ul style="list-style-type: none"> • Cannot penetrate through electrically conductive materials e.g. below the water table • Material with the same dielectric properties may be indistinguishable
Coring and drilling	<ul style="list-style-type: none"> • Continuous record • Gaining samples at depth • Portable • Can be used in waterlogged setting 	
Coring	<ul style="list-style-type: none"> • Inexpensive • Simple to use • They can be used in most sedimentary units 	<ul style="list-style-type: none"> • Cores are often disturbed so may not be representative • Cannot penetrate through coarser material
Drilling	<ul style="list-style-type: none"> • Greater penetration depth (km scale) • Can provide information on the stress on the fault and physical and chemical processes 	<ul style="list-style-type: none"> • Expensive • Size and weight of equipment • need a power source • limited access to sites
Paleoseismic trenching	<ul style="list-style-type: none"> • Three dimensional view of deformed zone • Strike and dip information • More reliable and definitive interpretations • High precision in measurements • Easy acquisition of dating materials 	<ul style="list-style-type: none"> • invasive • difficult to interpret complex faulting • site dependant • require space, landowner cooperation, environmental consenting, equipment • Money and time consuming • require a number of people • cannot trench under high water conditions
Magnetic intensity surveying	<ul style="list-style-type: none"> • Can detecting large and small scale faulting • Depth is not limited by moisture, salinity or clays 	<ul style="list-style-type: none"> • False signals are common from metals objects, especially in urban areas

Source: Guéguen and Palciauskas (1994), McCalpin (2009), Murray et al. (2005), Štěpančíková et al. (2010), Van Arsdale (2000), Woodward and Sloss (2013) and Zoback et al. (2010)

1.5.2 Dating techniques

Ages of past earthquakes can be obtained by measuring and dating faulted materials within exposures (McCalpin, 2009). The numbers are obtained by defining maximum and minimum ages for each event. Maximum ages are determined from materials which were deposited or emplaced before the earthquake and minimum ages are determined from materials which were deposited or emplaced after the earthquake. The most common technique for obtaining a materials age in paleoseismology is radiocarbon dating, however, where no carbon material is present Optical Stimulated Luminescence (OSL) dating is one of the techniques that is often utilised.

Radiocarbon dating is the most popular and reliable method for determining the absolute age of sediment during the Quaternary (Vittori et al., 1991). The radiocarbon dating method was first published in December 1949 and utilises the properties of the carbon isotope C^{14} to deduce the age of a material containing organic material (carbon). (Broecker, 2014). C^{14} decays exponentially over time and has a half life is 5,568 years, which is the time taken for the half of the atoms to decay (Jull and Burr, 2015). Measuring the remaining C^{14} in a sample allows the age to be determined. This technique cannot be used on samples which are greater than ~50,000 years in age, therefore it is commonly used on late Quaternary aged carbon (Jull and Burr, 2015). After dating materials the age is usually shown in calibrated years before present (cal. yr BP) or years after death (AD), which uses a base year of 1950 (Jull and Burr, 2015). This date was selected as after 1950 major nuclear testing altered the atmospheres carbon isotope ratio (Arnold and Libby, 1949). Dating C^{14} is not very straight forward, the activity and number of the atoms varies, and it is therefore necessary to calibrate the samples with environmental factors, such as CO^2 and water content (McCalpin, 2009). Also, radiocarbon dates can over or underestimate ages if older or younger carbon contaminates the sample.

OSL is an alternative method for geological dating of sediments, often utilised when there is little in-situ material available for radiocarbon dating, such as alluvial and fluvial deposits. OSL is related to the stimulation of luminescence of a substance by the absorption of radiation; it became popular in the literature of the 21st century (Yukihara and McKeever, 2011). In geological dating, OSL measures the materials background radioactivity, and the length of time since the material was last exposed to sunlight (Le

Dortz et al., 2011). OSL dating can be applied to materials that have undergone large levels of bleaching which is absorbed by minerals such as quartz and feldspar. Quartz is a reliable material for OSL application in geology as it is abundant within sedimentary deposits and has a simple crystal structure (Yukihara and McKeever, 2011). Samples containing quartz can be dated up to 350,000 years (Murray and Olley, 2002). Feldspar is also common in many sedimentary deposits, and it can store a high amount of luminescence, therefore has the potential for even longer term dating (Rhodes, 2011; Yukihara and McKeever, 2011). OSL is often utilised for dating alluvial layers, however natural materials have a wide variety of properties and incomplete bleaching can be associated with errors (Le Dortz et al., 2011).

Radiocarbon and OSL dating are best used together to gain the most accurate results; for example, both techniques were utilised on samples collected and dated from along the surface rupture of the 1999 Chi-Chi, Taiwan earthquake to obtain a slip rate on the causative fault (Chen et al., 2003).

1.6 AIMS AND OBJECTIVES

Previous studies identified that augering sediments that have been dammed behind Akatore Fault scarps can be used to gain information on past events (Litchfield and Norris, 2000; Norris et al., 1994). Trenching the Akatore Fault has allowed us to build on previous work and provides a 3D exposure of the fault, which augering does not. Hence, we are able to gain more definitive and comprehensive information on past events.

Along the Akatore Fault, each uplift event has caused blocking of drainage of antecedent streams resulting in the build-up of silt, clay and often peat, therefore swamp sediments can be correlated to fault motion. Several sites along the Akatore Fault, which show evidence of stream blockage, appear to have trenching potential. In this study, we have

selected two sites to trench, at Big Creek and Rocky Valley Stream. Suitable layers within the trenches have been dated using radiocarbon and OSL methods, to investigate the timing and magnitude of prehistoric ruptures in the Holocene.

Furthermore, we have utilised geophysical techniques (GPR and magnetic intensity) to image the Akatore Fault at a site south of Taieri Mouth. Previous efforts to date marine terraces have suggested that the fault has offset the 125 ka marine terrace (Litchfield and Lian, 2004), therefore it will constrain the longer term behaviour of the fault.

Our findings have allowed us to assess the hazard implications of the Akatore Fault for Dunedin and comparison to other Otago faults.

My research questions have been as follows:

1. When did the Akatore Fault produce the most recent large earthquakes and how often do they occur?
2. What are the estimates of magnitude and recurrence interval for large Akatore Fault earthquakes?

Chapter 2

PALEOSEISMOLOGY



Big Creek antecedent gorge and trench site across the Akatore Fault scarp, the prominent step in the valley floor in the right-centre of the image. View is to the northeast.

2.1 INTRODUCTORY REMARKS

For this study, we trenched the Akatore Fault at two antecedent streams (Big Creek and Rocky Valley Stream) to constrain the timing of past earthquakes. In this chapter, I have described the process of selecting the site, the trenching procedure and the resulting trench logs. Then I have compiled the results to form a Holocene event history at Big Creek.

2.2 SITE SELECTION

Potential sites for trenching investigations were selected based on two criteria: A stream must cross the fault and the hanging wall must be in the downstream direction. In these situations a fault rupture would dam the stream and cause it to pond. Over time the stream will cut its way back into the uplifted side and continue to flow out towards the ocean. A number of sites meeting these criteria have been identified along the Akatore Fault, generally on the upstream sides of antecedent gorges. These sites may contain distinctive sedimentary successions from stream blockage, and provide useful stratigraphic relationships for paleoseismic fault trenching.

Site selection was also based on non-geological conditions such as amount of ground water, access and land owner permission. Two sites were selected. Site one at Big Creek and Site two at Rocky Valley Creek (Fig. 2.1).

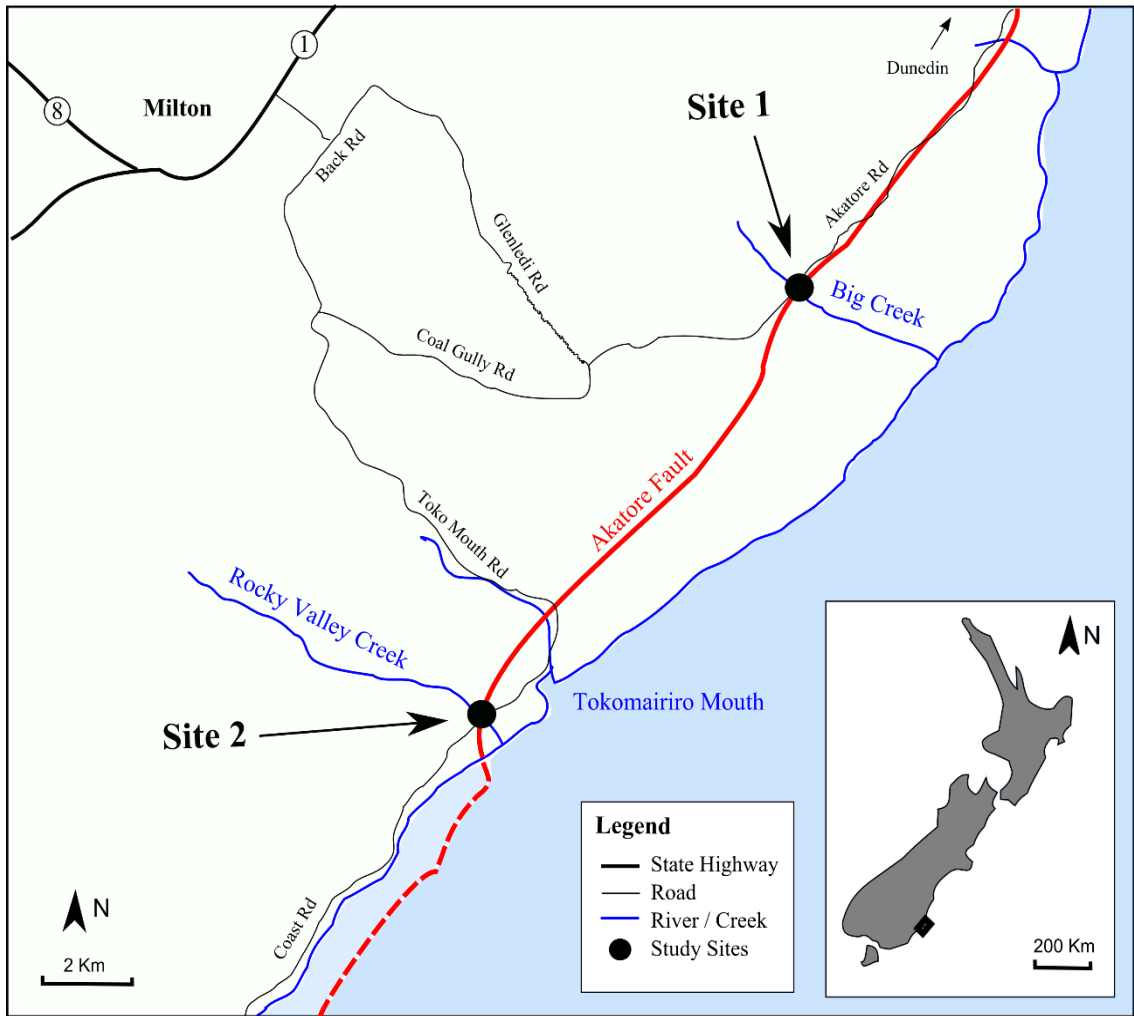


Fig. 2.1 Location of sites along the Akatore Fault and key transportation routes.

2.2.1 Big Creek

The Big Creek site is located on the south-east side of Akatore Road, GR: 46° 08' 51.887" S / 170° 07' 06.738" E (Fig. 2.1). The site is situated at the north-western side of an antecedent gorge, where Big Creek intersects an onshore section of the Akatore Fault (Fig. 2.2). The antecedent gorge and fault scarp can be clearly viewed from the road.

Previous investigations including mapping, coring, and shallow seismic refraction have been undertaken at this site by Norris et al. (1994) and Litchfield and Norris (2000). Sediments from coring consisted of silt and clays which are favourable indicators of stream blockage. On viewing the site, the fault has a distinctive ~ 2 m high scarp which cross cuts Big Creek (Fig. 2.3). This scarp protrudes out from a grass paddock, which can be accessed through a gate onto Akatore Road. The vegetation below the scarp (on the footwall) suggests a swamp environment with high water percolation, which may be problematic for fault trenching. The main stream, Big Creek, cross cuts the scarp along the edge of the valley wall to the north-east. To minimise the flow of water into the trench, the site was selected ~100 m down the scarp to the south-west. An auger core was collected ~ 4 m from the scarp, on the footwall side, to assess the underlying near-surface geology. Cores looked promising as they consisted primarily of grey silt and peat until 2.15 m in depth, where the sediment gradually transformed into consolidated, gritty silt with schist clasts. The cores contacted gravel at ~ 2.4 m, which gave some idea of the potential depth the trench would need to be excavated to (Fig. 2.4).

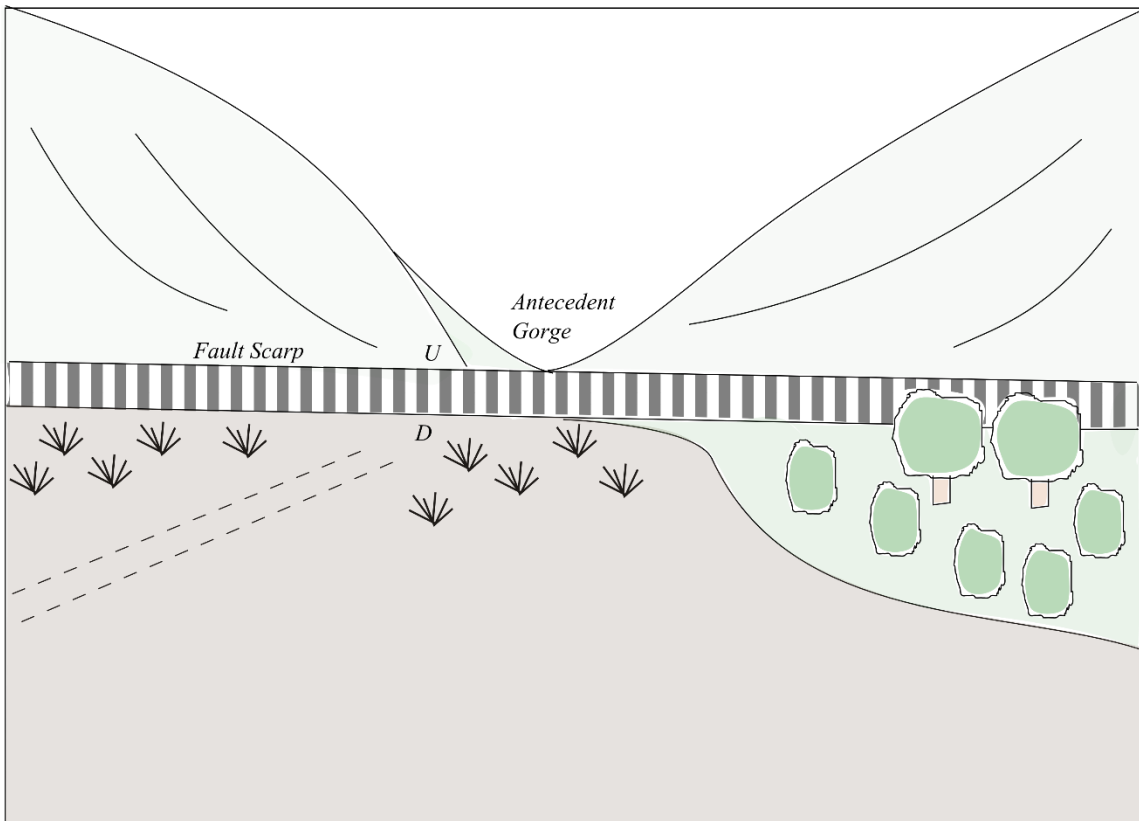


Fig. 2.2 View of Big Creek antecedent gorge (facing east). The Akatore Fault scarp is marked by stripes.

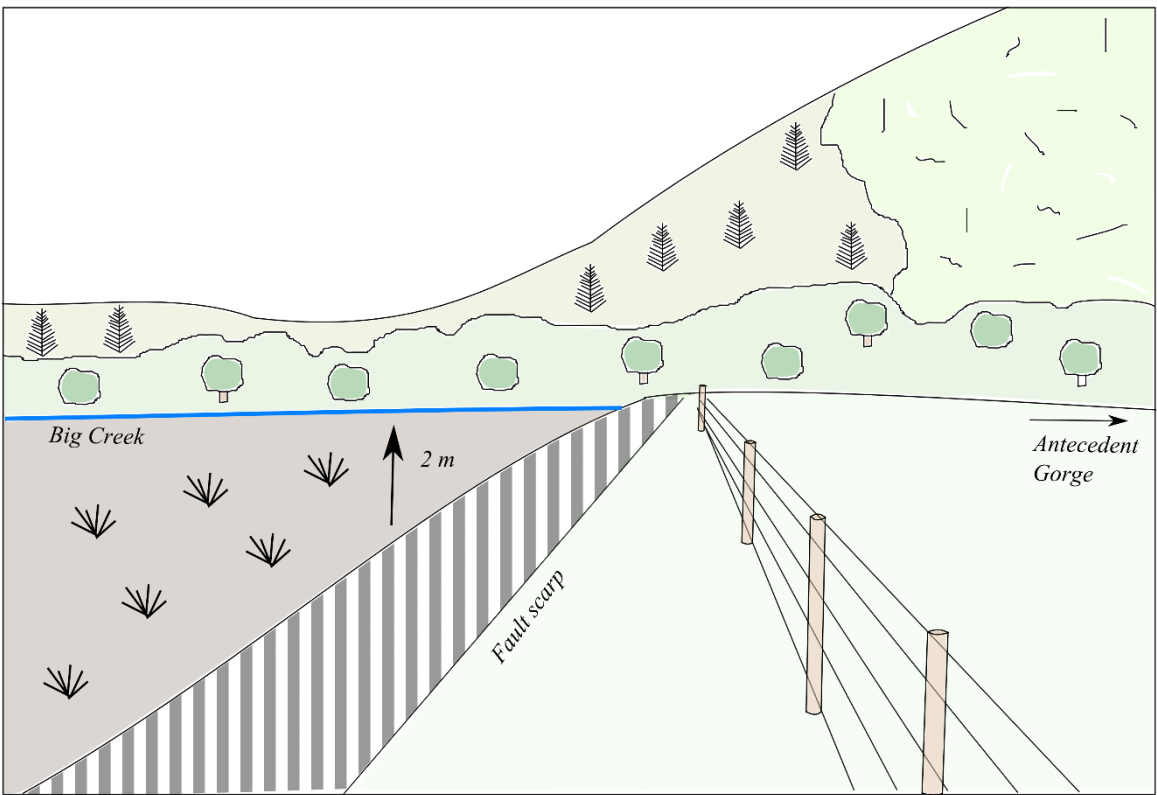


Fig. 2.3 View of the Akatore Fault scarp at Big Creek (facing north / perpendicular to the fault scarp). The fault scarp is marked by stripes.

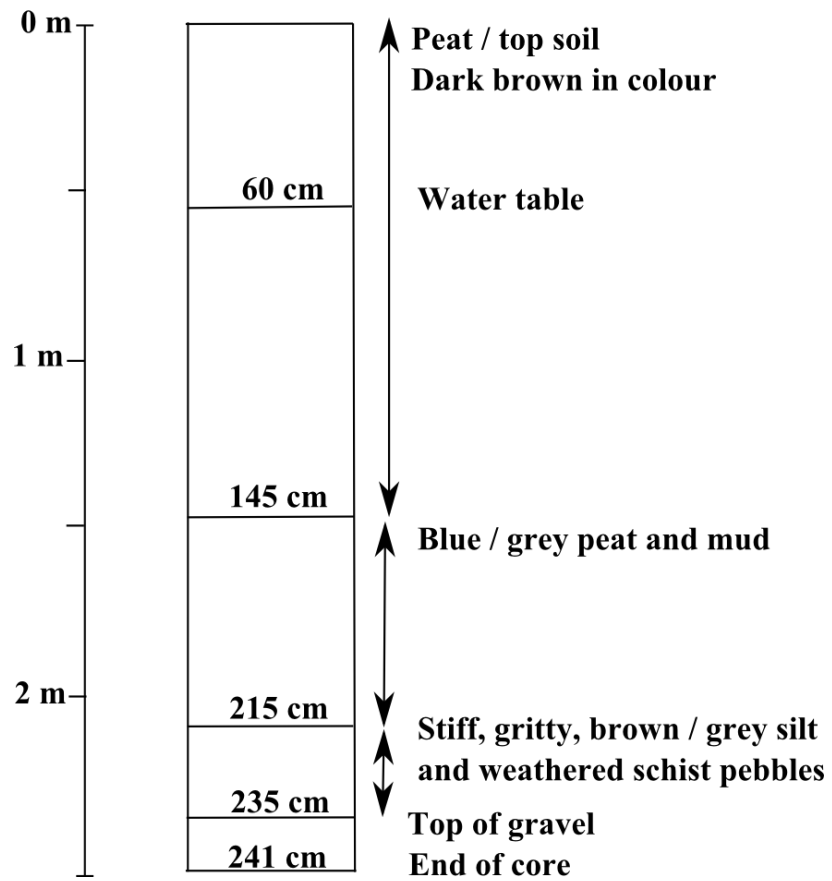


Fig. 2.4 Annotated down-core profile of an auger core collected on the footwall of the Akatore Fault at Big Creek.

2.2.2 Rocky Valley Creek

The Rocky Valley Creek site is located on the north-west side of Coast Road, at GR: 46° 13' 16.479" S / 170° 01' 45.404" E (Fig. 2.1). Light Detecting and Ranging (Lidar) images capture the southern onshore end of the Akatore Fault before it trails offshore. There is a distinctive trace of the Akatore Fault from depressions in the elevation, shown on the Lidar image (Fig. 2.5). Due to the lack of topography the trace of the fault is not as clear as through the valley. The Akatore Fault is expected to cross the path of the Rocky Valley Stream which should produce distinctive sedimentary sequences associated with uplift events.

Previous investigations have been undertaken at Rocky Valley Stream by Litchfield and Norris (2000). Ten auger cores were collected which contained peat, grey silt layers and sandy basal gravels, which suggested Rocky Valley as a promising site for fault trenching. The site was not as easily accessible as the Big Creek site, 4WD farm tracks provided access from Coast Road (Fig. 2.1).

Some difficulties emerged when viewing the site. The trace of the fault was not clear and potential trenching locations were limited by many obstacles such as farm crops, pine trees, fences, creeks/streams and swamp settings (Fig. 2.6). In addition, to the north, multiple valleys have transported young sediment into the site which could interfere with the interpretation of sediment deposition, therefore will not give a true representation of faulting events. Taking these factors into consideration, the trenching site was selected on a low lying paddock to the northern side of Rocky Valley Stream (Fig. 2.7).

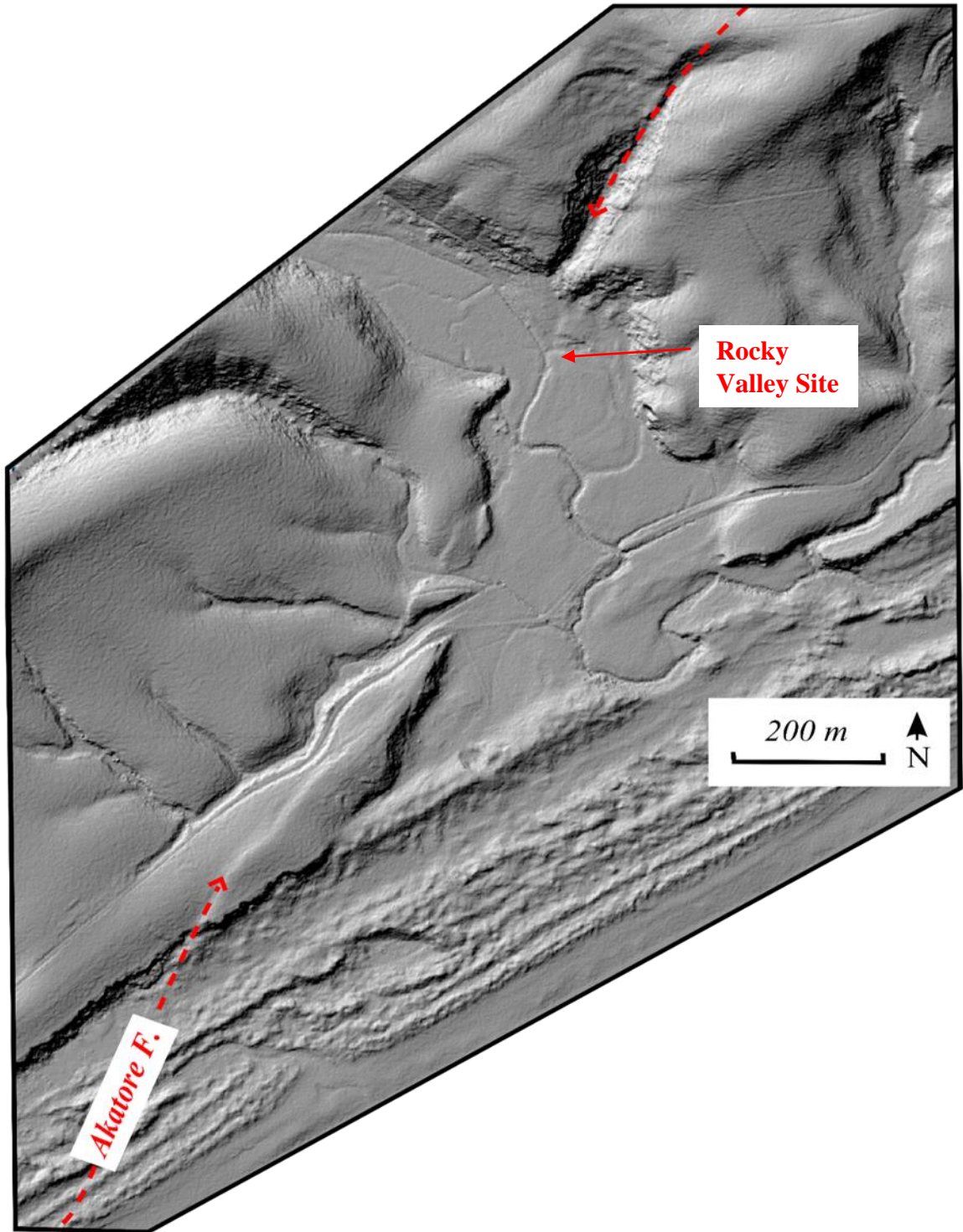


Fig. 2.5 Lidar image of the Rocky Valley site. The Akatore Fault is clearly marked by the change in elevation from the south-west to the north-east of the image (Lidar image sourced from the Otago Regional Council). Lidar uses laser scanners to produce detailed 3d images of structures by measuring the distance between the object and the receiver (Glennie et al., 2013).

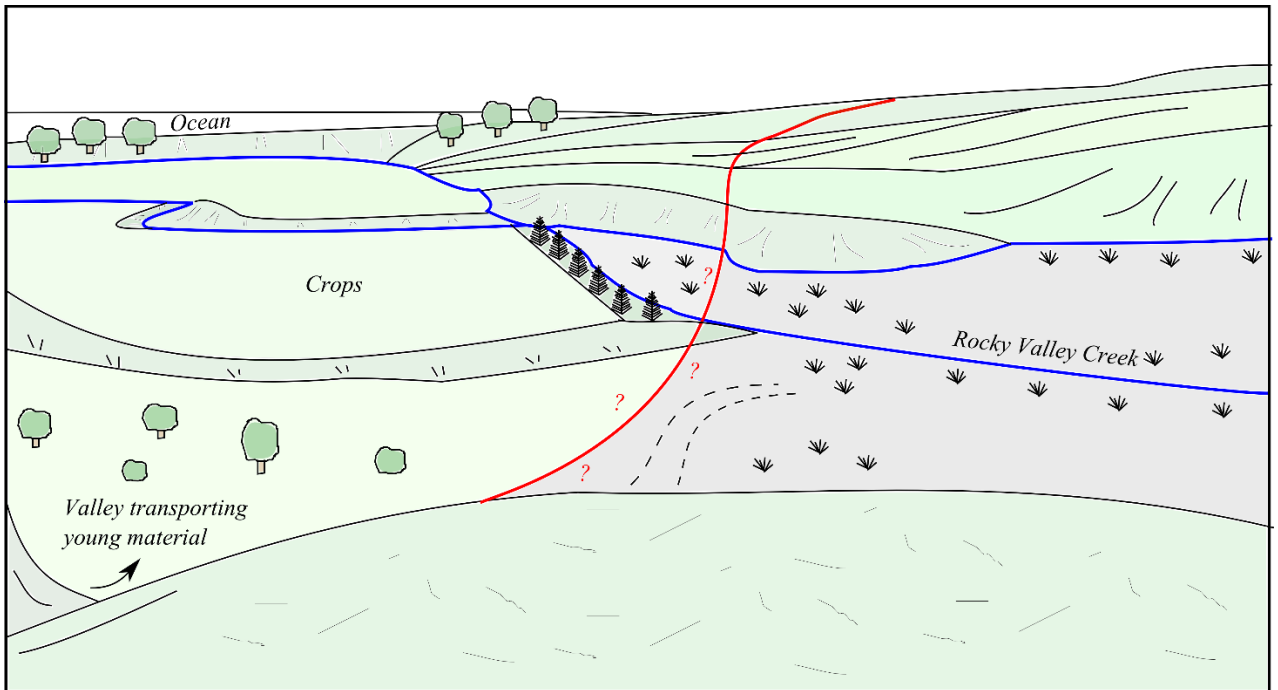


Fig. 2.6 View of Rocky Valley and the Akatore Fault (in red), facing south-east. The fault trace is not clear throughout the valley.

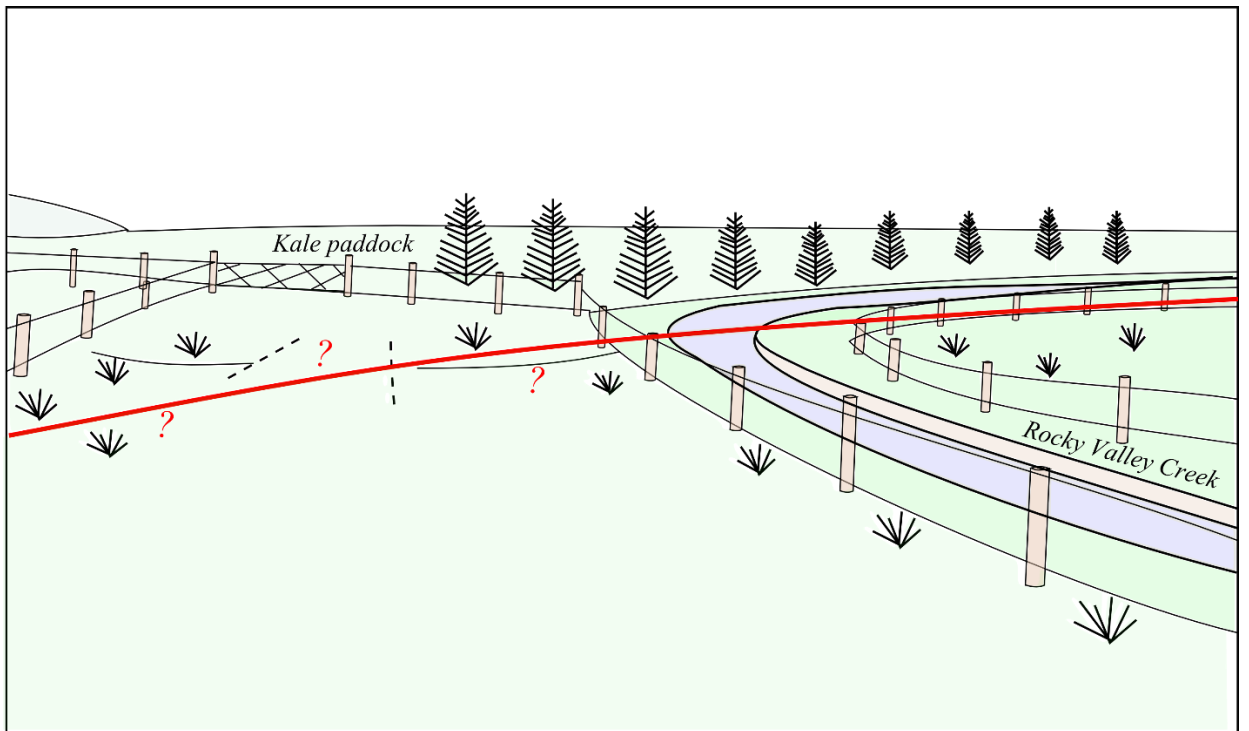


Fig. 2.7 View of Rocky Valley site facing east. The Akatore Fault trace (in red) is not clear through the site.

2.3 TRENCHING PROCEDURE

2.3.1 Excavating

Once the sites were selected, digger excavation was undertaken on the 2nd of March 2016. The Rocky Valley site was excavated starting at 9 am, 5.5 m above sea level. The trench was ~15 m long, ~ 3.5 m deep and several metres wide to accommodate a ~ 1 m deep bench on either side of the trench. The trench was dug across what appeared to be, a small scarp within the paddock near Rocky Valley Stream. Ground water was problematic as the trench quickly filled up with water, resulting in the collapse of the bench on the north wall. As a result the trench was not excavated deep enough to expose the fault plane or schist bedrock (Fig. 2.8). The walls of the trench were cleaned by removing the top layer of sediment which was disrupted by the digger. The aim was to search for any discontinuities in the stratigraphy or folding which may suggest that the trench has intersected the fault. Folding of layers towards the western end of the Rocky Valley trench were apparent (Fig. 2.9), which suggested the trench encompassed the hanging wall and that the fault was close. We would like to have trenched deeper towards the south but were unable to because of the Rocky Valley Stream. The trench contained a substantial amount of peat and pieces of wood, which would be useful for radiocarbon dating.

Excavation began at Big Creek at 1 pm. Big Creek is ~11 km north-east of the Rocky Valley site, ~100 m above sea level. The trench was excavated across the ~ 2 m scarp and was dug ~ 30 m long, ~ 4 m deep, and several metres wide to account for the 1 m deep benches. It was clear from the excavation that there was a distinct change in lithology as the digging commenced over the scarp. Here the lithology changed from hard schist bedrock to consolidated sediment which indicated the trench had intercepted the fault (Fig. 2.10). Further digging of the footwall exposed underlying schist, which suggested that the trench contained the entire package of sediment. After cleaning down the walls of the trench, initial observations identified one or two colluvial wedges, which

correlated to faulting events. A peat layer was apparent where the trench exposed the fault.



Fig. 2.8 Rocky Valley trench after excavation (facing south-east).



Fig. 2.9 Folding lithology (red dashed lines) on the south wall of Rocky Valley trench.



Fig. 2.10 Big Creek trench after excavation. The red dashed lines denote where the trench intercepts the Akatore Fault. **A.** View of the trench looking east, perpendicular to the scarp. **B.** The Akatore Fault on the south wall of the trench.

2.3.2 Logging and sampling

Considerable work was carried out at the Big Creek site as it contained the most useful paleoseismic information. This took place over five consecutive days. When visiting Big Creek the second day (3rd of March) some of the walls had caved in and the water level had risen. The water was pumped out every morning prior to working in the trench.

Firstly, the trench had to be prepared for logging. A 1 m quadrant string grid was constructed on the trench walls. Next, the different units / horizons and interesting features were marked with coloured nails (Fig. 2.11).

Once all features had been marked, such as lithology, liquefaction features, colluvial wedges, bedding and faults, the trench walls were logged onto graph paper. Caving in of the trench walls had caused the schist on the footwall to be concealed. Two schist outcrops were exposed from digging 50 cm into the bottom of the trench. Once both the north and south wall had been logged, descriptions of each of the units were compiled. Finally, the site was surveyed with a Leica GNSS Smart Antenna to obtain a profile of the trench and the scarp. The perimeter of the trench was surveyed every few metres and several measurements were collected of the strath and fault. In addition, the scarp was surveyed by collecting measurements at 1 m increments.

Once the site had been surveyed, samples were collected for radiocarbon dating (Fig. 2.11). Samples were selected on horizons that correspond to time before and after faulting events, and to correlate the two ends of the trench. Various sized samples were excavated, placed inside zip lock bags and labelled. Four radiocarbon samples (BC01-BC04) were collected consisting of peat, wood fragments and sediment containing small pieces of organic material. BC01 and BC02 were both collected from a layer of peat in the north wall. BC01 was a peat sample, while BC02 was a wood sample, 2.5 cm in diameter. BC03 and BC04 were also from the peat layer but were collected on the south wall. BC03 was a peat sample while BC04 was a wood sample, 2 cm in diameter.



Fig. 2.11 Big Creek trench divided into 1 x 1 m quadrants with important features highlighted. **A.** The different lithologies with coloured nails are being marked on the south wall in the image. **B.** View of the Akatore Fault (schist overlying sediments) on the north wall. Writing in orange corresponds to radiocarbon sample locations.

Only one day (8th March), was spent at Rocky Valley Stream, as the trench was completely full of water, and it took a large portion of the day to drain by way of flexi pump (Fig. 2.12A). The bench on the north side was completely collapsed so only the south side was logged. Similar procedures took place as at the Big Creek Site (Fig. 2.12B; 2.13). Radiocarbon samples were selected to best characterise the earthquake history of the fault. Ten radiocarbon samples (RV01-RV10) were collected consisting of wood fragments and silt with small pieces of organic material. Samples RV01 – RV05 were collected on the same layer within faulted sediment (organic rich silt). RV01, RV04 and RV05 were sample of wood, while RV02 and RV03 were samples of plant material. Above this layer RV10 was collected from unfaulted-faulted sandy silt and RV06 – RV09 were collected from the unfaulted subsoil.

On the 9th of March, David Barrell from GNS Science visited the Big Creek trench to review the trench and initial interpretations. Optically stimulated luminescence (OSL) samples were collected for dating. Samples were collected from fine grain sands and silts. All of the samples were collected from vertical faces. The faces were excavated to a 30 cm depth before sampling to gain a ‘fresh sample’. Samples were collected by hammering a plastic piston core into the sediment (Fig. 2.14). Once the core was well immersed it was removed along with the sediment. The ends of the core were packed with aluminium foil and then wrapped extensively in black tape. Samples were labelled and placed in a black bag. These methods were used to minimise light exposure. Seven OSL samples were collected from silt and soil horizons (BCK01-BCK07). BCK01-BCK06 were collected in the north wall. BCK01 was collected from a silt lens within the gravel. BCK02 and BCK03 were collected from silt above the gravel on the hanging wall, while BCK04 and BCK05 were collected from silt above the gravel on the footwall to see if the silts on both walls are correlated. BCK06 was collected in silt above the peat and BCK07 was collected from silt within the colluvial wedge in the south wall.

Several of the radiocarbon and OSL samples from the trenches were sent to the laboratory at GNS science in Lower Hutt to be dated. The OSL samples were dated using a fine grained method which involves dating K-feldspar. Details can be found in the OSL report (Appendix 3).



Fig. 2.12 Preparing Rocky Valley trench for logging (facing south-west). **A.** On arrival the trench was completely filled with water. **B.** Hours later, the majority of the water was pumped from the trench and the south wall was divided up into 1 x 1 m quadrants.



Fig. 2.13 The coloured nails mark the folding over of lithology on the southern wall of the Rocky Valley trench.



Fig. 2.14. Collecting an OSL sample (BCK04) in the north wall of the Big Creek trench.

2.4 TRENCH DESCRIPTION

This section describes the lithology, stratigraphy and initial interpretations of Big Creek and Rocky Valley trenches. Detailed unit descriptions can be found alongside the digitised logs (Fig. 2.16; 2.17; 2.19).

These trench logs were constructed based on a colour and labelling scheme developed by GNS science (D. Barrell, pers. comm.). The simple colour scheme is shown in Fig. 2.15. Units are labelled based on the degree of deformation and their sedimentary characteristics. Each unit is assigned a number/s which refers to their degree of deformation; 1 is given for top soil, 2 is given to un-deformed sediments below the top soil, 3, 4 and 5 are given to deformed units, in order of the degree of deformation. Where the deformation is unclear a range of numbers were given. Next, each unit is assigned a letter which is used to distinguish its sedimentary characteristics. In addition some letters are assigned an exponent, where they have slight variations in their sedimentary characteristics but overall have been interpreted as the same unit.





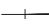










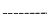

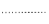

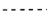








Unit Material	Symbols	
 No description	 Top of trench	 Individual cobble sized clast
 Topsoil	 Bench in trench	 Orientation of clasts
 Silt / sand	 Bottom of trench	 Radiocarbon dating sample
 Fine alluvial gravel	 End of trench	 Optically stimulated luminescence dating sample
 Coarse alluvial gravel	 Unit boundary	
 Colluvium	 Unit boundary (approximate)	
 Schist	 Interpolated unit boundary below trench	
 Mixed zone	 Bedding	
<i>Layers</i>	 Late Quaternary Fault	
 Collapsed zone	 Strike / dip and dip direction (measured on fault)	
 Clay accumulation	 Free face	
 Organic rich	 Inferred free face	
 Peat		

Fig. 2.15 Legend for digitised trench logs at Big Creek and Rocky Valley sites

2.4.1 Big Creek trench

Logs from both the north and south walls of the Big Creek trench were digitised using Arc GIS and Inkscape software (Fig. 2.16; 2.17). Also, field photos were compiled to produce a detailed picture of the trench walls (Appendix 2).

On the hanging wall, schist bedrock was exposed that has overthrust the sediments in the footwall. Schist was also exposed at the base of the trench in the footwall and has a flat surface (strath) cut into it. Overlying the schist unconformably was a unit of gravel, which has also been offset. The gravel had faint imbrication orientated west-east. Tilting of the sediments was observed in the hanging wall, and was most evident on the south wall. Within the gravel were lenses of silt, unit 5d. Overlying the gravel, in an erosional contact, was a sediment package that largely consisted of silt (unit 5b¹ and 5a¹). Towards the surface the silt transitioned into soil horizons (unit 2a, 2b and 1a). Here there were fissures and possible evidence of liquefaction, most noticeably on the north wall.

On the footwall the schist bedrock was exposed during excavation, however it was buried the following day due to collapsing of the trench walls and the infilling by ground water. The schist was dug out on the north wall at two locations, illustrated on the trench logs (Fig. 2.16; 2.17.). Overlying the schist was gravel, similar to the hanging wall, however the upper contact was much more undulating. A unit of silt (5b²) overlaid the gravel. The silt on the hanging wall and footwall (unit 5b¹ and 5b² respectively) were similar with some variations in the percentage of schist gravel and mottling. Above this unit was another package of silt (unit 5a²), which had a mottled appearance on the north wall of the trench. This in turn was overlaid by peat (unit 4a), silt (unit 3c) and modern organic material (unit 2d), which was consistent with the present day swamp setting. The wet, swamp setting had restricted the formation of the soil horizons; in the hanging wall, no soil horizons were observed on the south wall of the trench, and only the top soil was apparent on the north wall, with a small amount of subsoil (unit 2a) near the fault.

The fault zone contained multiple units of colluvial gravel, which are described in detail on the trench logs (Fig. 2.16; 2.17.). These ranged from silt to gravel.

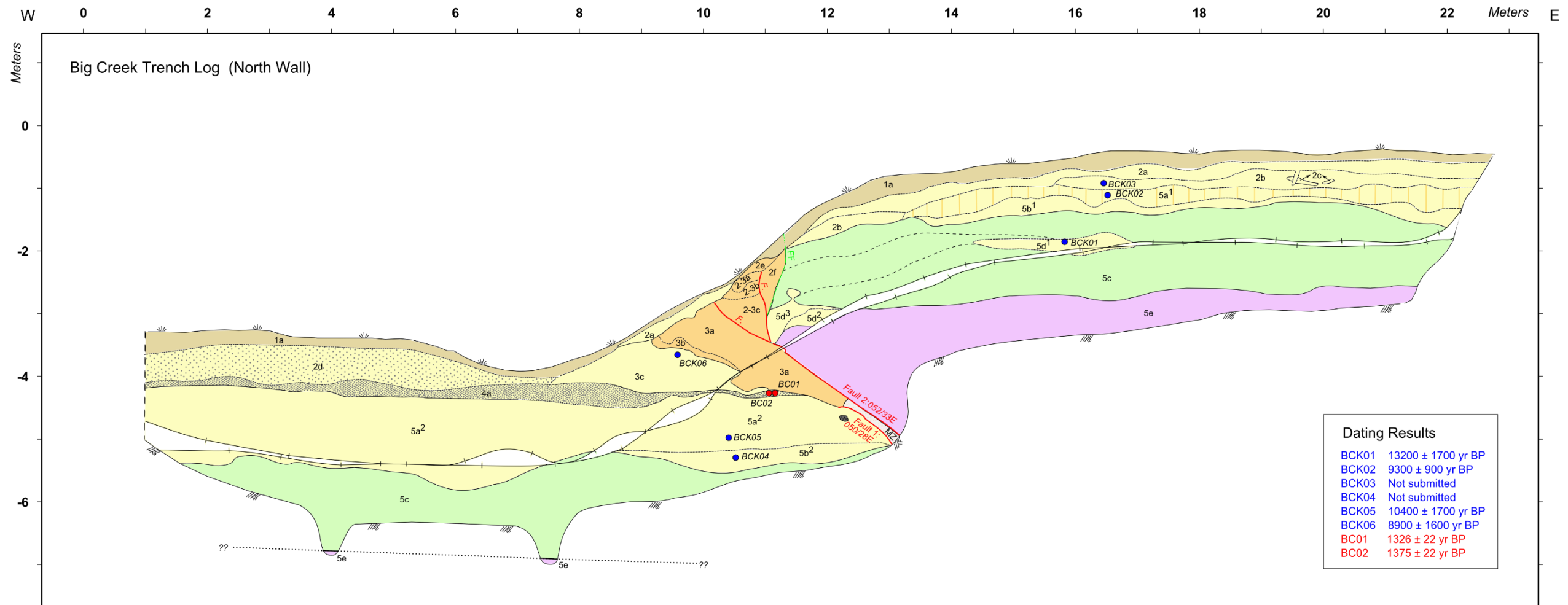
From observing the different sedimentary packages, multiple faulting events were interpreted from the trench. Each fault trace has been marked along the trench log in red.

The antepenultimate event was defined on the basis of the displacement of the basal unit, (schist, unit 5e) and the deposition of the peat (unit 4a). Uplift of the hanging wall during the first earthquake would have displaced the schist across the fault. This would have dammed Big Creek, resulting in ponding on the footwall. As the peat was only on the footwall, it was likely to have developed in response to this preserved fault rupture event. The fault plane had a strike and dip of: 050/ 28 E (north wall; Fig. 2.16).

A colluvial wedge (unit 3a) overlay the peat (unit 4a) which suggested a second event. This means an unstable scarp had to have been formed above and beside the peat. The penultimate and most recent event were separated by a mixed zone (Mz), which was a combination of gravel and silt. The fault plane had a strike and dip of: 052/ 33° E (north wall; Fig. 2.16) and 064 / 49° E (south wall; Fig. 2.17) for the second event.

The colluvial gravel (unit 3a), was in faulted contact with the schist, which suggested a third event in the trench (i.e. faulting of the colluvial wedge). Distinguishing any additional colluvial wedges, proved to be difficult, as some of them had been faulted, while others were deposited after the last event. The fault plane for this third event was not well defined, therefore a strike and dip was not measured. For the rest of this study 41° was used for the dip of the fault, which is the average dip calculated in the Big Creek trenches for the penultimate event. Using this dip and the offset between the top of the gravels, resulted in a total displacement of ~5 m.

In addition to the trench, the fault was also exposed on the south side of the Big Creek Valley (Fig. 2.18). Here the fault had a strike and dip of 018/ 28 E.

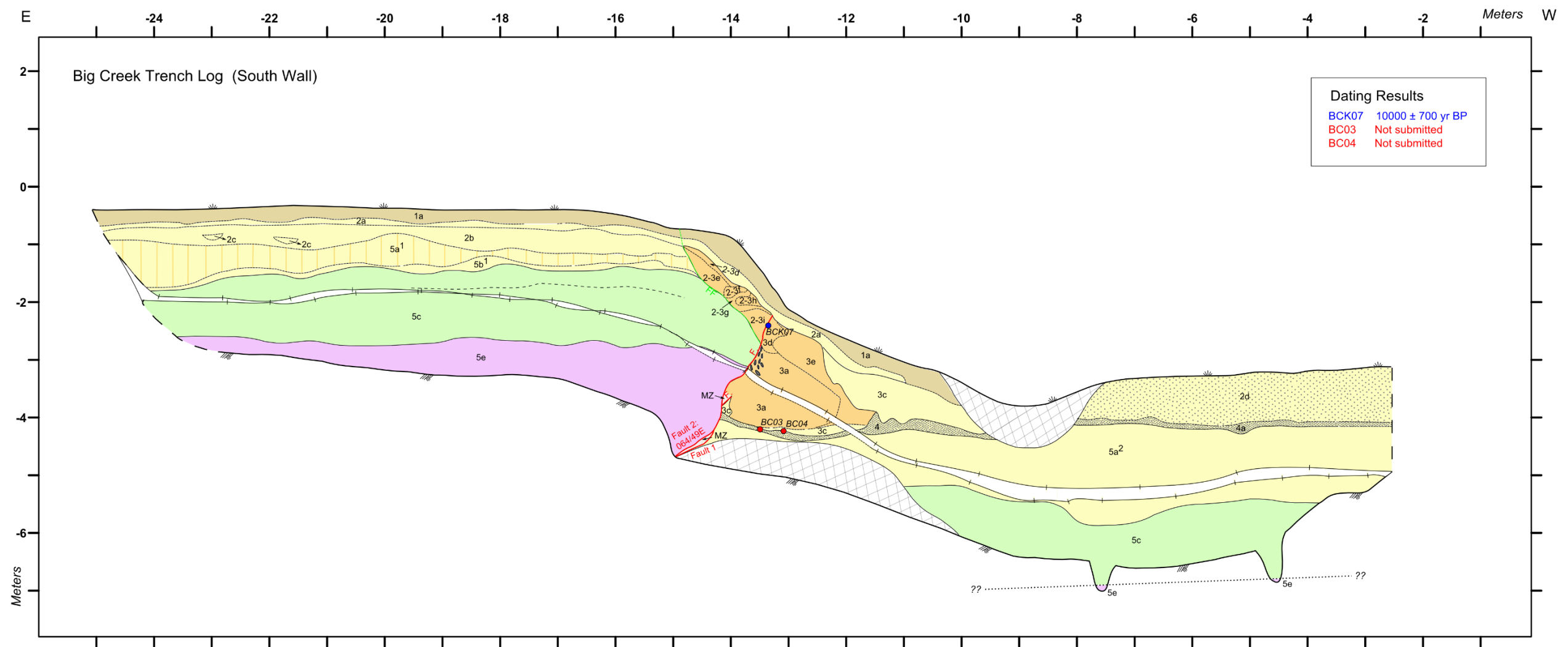


Dating Results	
BCK01	13200 ± 1700 yr BP
BCK02	9300 ± 900 yr BP
BCK03	Not submitted
BCK04	Not submitted
BCK05	10400 ± 1700 yr BP
BCK06	8900 ± 1600 yr BP
BC01	1326 ± 22 yr BP
BC02	1375 ± 22 yr BP

Unit Descriptions (Big Creek Trench)

- | | | | |
|--|--|--|---|
| <p>1a Light grey to brown coloured silt with abundant roots. Silt has a crumbly texture. 1 = topsoil</p> <p>2a Light yellow to brown coloured silt with grey to brown coloured burrows. 2a = subsoil.</p> <p>2b Massive, creamy grey to orange coloured silt, which has some mottling. Towards the east there is evidence of liquefaction from a 20 cm long fissure in the north wall which has been infilled with very fine sediment. 2b = leached soil</p> <p>2c Within unit 2b, lenses of grit are evident, composed of subangular schist ≤ 3 mm in size. Some bedding is present.</p> <p>2d Chocolate brown coloured organic silt which becomes lighter at the top (drier). The organic silt has abundant plant material, primarily roots with no visible traces of wood.</p> <p>2e Creamy light yellow to orange mottled silt. The silt is massive with sparse clasts of subangular to subrounded schist with a maximum size of 3 cm.</p> <p>2f Creamy orange to brown pebble sized schist gravel. The gravel is subangular to subrounded with a maximum clast size of 13 cm. The gravel is clast supported with a sandy matrix. It is poorly sorted and has a chaotic appearance.</p> | <p>2-3a Creamy grey pebble sized schist gravel. The gravel is subangular to subrounded with a maximum clast size of 8 cm. It is clast supported with a silt matrix. The gravel is moderately sorted with a chaotic appearance.</p> <p>2-3b Creamy orange to brown mottled silt. The silt is massive with sparse clasts of subangular to subrounded schist ≤ 5 cm in size.</p> <p>2-3c Grey-orange to brown pebble to cobble sized gravel. The gravel is poorly sorted, subangular to subrounded schist with a maximum clast size of 26 cm. It is massive in structure.</p> <p>3a Same as 2-3c</p> <p>3b Mottled blue-grey to orange-brown coloured silt with small pebbles which have a maximum clast size of 3 cm. It is massive in structure.</p> <p>3c Blue-grey to orange-grey coloured massive silt which grades into a very fine sand. Modern roots are abundant. Some mottling is evident.</p> <p>4a Dark brown to black coloured fibrous peat with abundant roots and wood. One log was measured 10 cm in diameter.</p> | <p>5a Massive grey-orange to brown coloured silt with sparse subrounded schist clasts.</p> <p>5a¹ <i>Hanging wall:</i> Mottled silt with clasts ≤ 4 cm in size. When dry, subvertical cracks form.</p> <p>5a² <i>Foot wall:</i> The top 20 cm of the silt contains abundant plant material and charcoal. The silt is mottled on the north wall where one large (12 x 9 cm) clast was observed.</p> <p>5b Blue-grey to orange-brown coloured silt with gravel. Gravel is composed of subangular to subrounded schist.</p> <p>5b¹ <i>Hanging wall:</i> Massive silt composed of 20 % schist gravel with a maximum clast size of 13 cm.</p> <p>5b² <i>Foot wall:</i> Mottled silt composed of 5% schist gravel with a maximum clast size of 11 cm.</p> <p>5c Subrounded to subangular cobble gravel which is creamy grey, orange to chocolate brown in colour. The gravel is moderately sorted with a maximum cobble size of 20 cm. Crude bedding is evident on a decimeter scale. This is often highlighted by iron staining (limonite) which follows the bedding plane. Also, there are some finer beds which consist of pebble gravels with an average clast size of 3 cm; clasts are predominantly schist. The gravel is clast supported with a sand matrix.</p> | <p>5d On the north wall, within the gravel (5c) there are lenses of light green-grey to orange coloured medium sand with grit. The grit is composed of subrounded to subangular schist.</p> <p>5d¹ Some faint bedding is evident on the cm scale. Here, the silt is composed of 30% grit.</p> <p>5d² Towards the fault the grit composition increases to 60%, where the clasts are ≤ 3 cm in size.</p> <p>5d³ At the fault these lenses become poorly sorted and chaotic. Here, clasts are ≤ 12 cm in size</p> <p>5e Predominantly dark to light grey in colour, however the top 20-30 cm is weathered an orange colour. The schist has a fractured appearance and there are no obvious quartz veins observed. The schist becomes increasingly friable and shears sub-parallel within 2 m of the fault. Along the fault is a 2.7 cm thick greyish black gouge.</p> <p>MZ Blue-grey to orange coloured pebble to cobble sized gravel. Clasts are subrounded to subangular schist with a maximum clast size of 13 cm, on the north wall. The gravel is moderately sorted and massive in structure with sparse silt lenses. It is clast supported with a silt matrix.</p> |
|--|--|--|---|

Fig. 2.16 Graphical representation of Big Creek trench (north wall), during field work early March, 2016. Refer to Fig. 2.15 for legend.



Unit Descriptions (Big Creek Trench) *

- | | |
|--|---|
| <ul style="list-style-type: none"> 2-3d Yellow-brown to orange coloured silt. The silt is massive and very fractured. 2-3e Light yellow to brown-orange coloured silt with small pebbles with a maximum clast size of 3 cm. It is massive in structure. 2-3f Chocolate brown coloured fibrous silt with abundant roots. 2-3g Creamy grey to orange coloured mottled silt, which is massive in structure. 2-3h Yellow-brown to orange coloured pebble sized gravel. Clasts are moderately sorted, subrounded to subangular silt with a maximum clast size of 10 cm. The gravel is clast supported with a silt matrix. It is massive in structure. 2-3i Creamy grey to orange coloured pebble to cobble sized gravel. Clasts are moderately sorted, subrounded to subangular silt with a maximum clast size of 10 cm. The gravel is clast supported. It is massive in structure. | <ul style="list-style-type: none"> 3d Creamy grey to orange coloured very fine sand to silt. It is mottled and massive in appearance with sparse clasts ≤ 5 cm in size. 3e Creamy grey to orange-brown coloured massive silt with clasts ≤ 5 cm in size. Clasts are subangular to subrounded and compose 5% of the colluvium. Modern roots are abundant. Generally, fractures occur along modern roots. <p>* Only includes descriptions of units which have not previously been described (see North Wall).</p> |
|--|---|

Fig. 2.17 Graphical representation of Big Creek trench (south wall), during field work early March, 2016. Refer to Fig. 2.15 for legend and Fig. 2.16 for unit descriptions previously described.

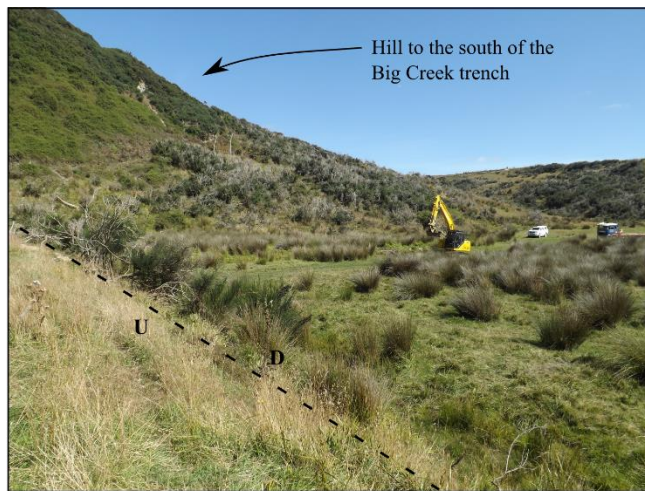


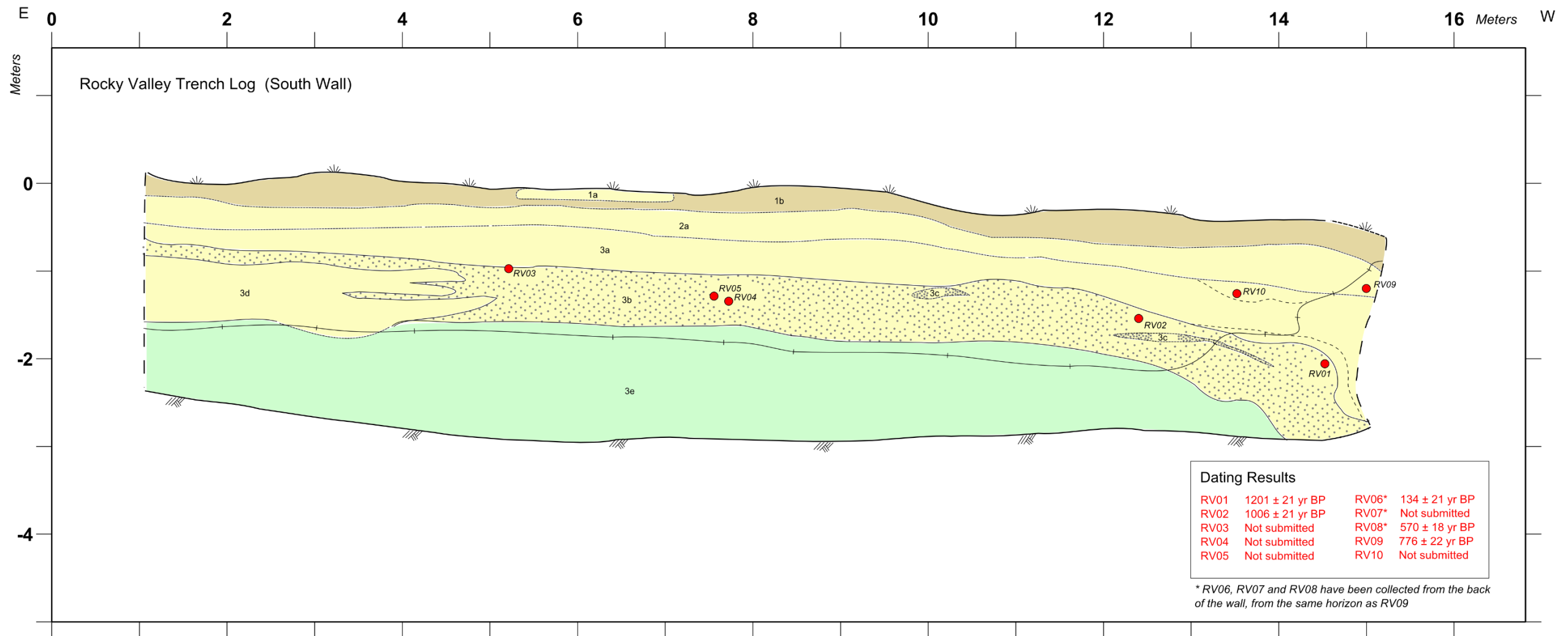
Fig. 2.18 The Akatore Fault exposure on a hill to the south of the Big Creek site.

.4.2 Rocky Valley trench

A log from the south wall of Rocky Valley trench was digitised using Arc GIS and Inkscape software (Fig. 2.19). Field photographs were also compiled to produce a detailed picture of the south trench wall (Appendix 2).

The Rocky Valley trench only exposed the uppermost portion of the hanging wall of the fault, and only the south wall was logged. Roll over tilting of the sediments indicated close proximity of the footwall at the end of the trench, however rapid influx of water into the trench prevented further excavation. As the fault was not exposed in the trench the extent of deformation of the units is unclear. For this reason, all units which have undergone deformation have been labelled with a 3, regardless of the level of deformation (Fig. 2.19).

Schist bedrock was not exposed in the Rocky Valley trench. The oldest unit visible was a quartz gravel (unit 3e), likely either primary, or reworked gravel from the Taratu formation. Overlying the gravel was an organic rich silt which may represent an ancient swamp deposit (unit 3b). Within the silt were lenses of peat which showed rollover tilting towards the western end on the trench. The organic rich silt progressively became drier towards the east (away from the fault) where it fingered into a gritty sand (unit 3d). This unit was interbedded with sand and silt, and was interpreted as an old channel deposit. Overlying these units was a mottled sandy silt (unit 3a). Towards the western end of the trench, sand beds also showed rollover tilting. This unit gradually transitioned into sub soil and top soil towards the surface, 2a and 1b respectively. These were unfaulted sediments. Within the top soil there was a large overbank deposit (unit 1a), suggesting this was a modern floodplain setting.



Unit Descriptions (Rocky Valley Trench)

- | | |
|--|---|
| <p>1a Irregular and gravelly Overbank deposit.</p> <p>1b Grey to brown silt with abundant modern roots. Occasional subangular to subrounded quartz clasts ≤ 3 cm in size. 1b = topsoil</p> <p>2a Yellow-grey to brown mottled silt, with few modern roots. Widely spaced, irregular fractures are observed. 2 = subsoil</p> <p>3a Mottled, grey coloured sandy silt with yellow to brown staining, which increases towards the top. The mottling also increases towards the surface. Bedding is present.</p> <p>3b Organic rich blue to grey coloured sandy silt which becomes mottled towards the top. Abundant organic material is observed throughout, which consists of roots, twigs and charcoal. The silt is interbedded with lenses of yellow to brown coloured coarse sand to fine gravel. These interbedded sediments are ~10 cm in thickness.</p> <p>3c Inconsistent lenses of dense, organic rich silt.</p> | <p>3d Yellow-brown to yellow-grey coloured coarse sand to gravel with occasional thin sandy gravel lenses. The sediment is clast supported with a fine matrix. Clasts are well sorted and subrounded. The maximum clast size is 1 cm in diameter. Towards the west the gritty sand is interbedded with a sandy silt (cm thickness). The sediment fines upwards.</p> <p>3e Quartz rich sandy-silty gravel which is yellow to grey in colour. Clasts are subrounded to rounded with a maximum size of 5 cm. The gravel is moderately to well sorted and fines towards the top. It is clast supported with a sand matrix. Faint bedding is observed.</p> |
|--|---|

Fig. 2.19 Graphical representation of Rocky Valley trench (south wall), during field work early March, 2016. Refer to Fig. 2.15 for legend.

2.5 RADIOCARBON AND OSL DATING RESULTS

Sediment samples were selected for OSL and radiocarbon dating. Sampling locations can be observed in Fig. 2.16, 2.17 and 2.19. Sample information and their corresponding ages are shown in Table 2.1, 2.2. Detailed reports can be found in Appendix 3.

Multiple samples from the same units provided varying radiocarbon ages. We chose preferred ages, to use for sequential work, for units 4a, 3b and 2a for the following reasons:

- Wood is often disturbed and not in its original growth position. Dating wood only provides the maximum age of the sediment, as the wood may have died and been re-deposited in younger material (Bartsch-Winkler and Schmoll, 1992). We used samples with the least wood such as BC01 (for unit 4a; Fig. 2.16) and RV02 (for unit 3b; Fig. 2.19).
- Samples of plant material in the upper layers of a trench can often be contaminated by younger roots. Within the subsoil (unit 2a; Fig. 2.19) in Rocky Valley trench, plant material was abundant and some of the radiocarbon ages were younger than expected. We use sampled RV09 which had the oldest radiocarbon age.

Table. 2.1 Big Creek and Rocky Valley radiocarbon ages from this study. Detailed reports are in Appendix 3

Trench Site	Sample #	Description	Unit	Collection date	Calibration curve	Max. Age (Cal.cal. yr BP)	Min. Age (Cal.cal. yr BP)	Max Age (AD)	Min Age (AD)	Conventional radiocarbon age (cal. yr BP)
Rocky Valley	RV01	Wood within organic silt.	3b	8-Mar-16	SHCaLI3	1170	977	973	776	1201 ± 21
Rocky Valley	RV02	Plant material within organic silt.	3b	8-Mar-16	SHCaLI3	924	801	1149	1026	1006 ± 21
Rocky Valley	RV06	Bulk peat sample.	3a	8-Mar-16	SHCaLI3	253	0	1697	1950	134 ± 21
Rocky Valley	RV08	Bulk peat sample.	3a	8-Mar-16	SHCaLI3	551	517	1399	1433	570 ± 18
Rocky Valley	RV09	Organic silt.	3a	8-Mar-16	SHCaLI3	721	652	1298	1229	776 ± 22
Big Creek	BC01	Bulk peat sample.	4	7-Mar-16	SHCAL13	1275	1121	829	675	1326 ± 22
Big Creek	BC02	Piece of wood in peat.	4	7-Mar-16	SHCAL13	1300	1184	766	650	1375 ± 22

Table. 2.2 Big Creek OSL ages from this study. Detailed report is in Appendix 3.

Trench Site	Sample #	Description	Unit	Collection date	Luminescence Age (cal. yr BP)
Big Creek	BCK01	Silt lens within gravel	5d ¹	9-Mar-16	1325 ± 1201
Big Creek	BCK02	Silt from BT horizon	5a ¹	9-Mar-16	9300 ± 900
Big Creek	BCK05	Mottled silt above gravel	5a ²	9-Mar-16	10400 ± 1700
Big Creek	BCK06	Silt grading to fine sand	3c	9-Mar-16	8900 ± 1600
Big Creek	BCK07	Silt from Colluvial wedge	3d	9-Mar-16	10000 ± 700

2.5.1 Comparing OSL and radiocarbon ages with previous work

Previously, Litchfield and Norris (2000) collected auger and percussion cores from Bull Creek, Nobles Stream, and Rocky Valley Creek. These cores were collected on the downthrown side of the Akatore Fault, in an attempt to capture samples from buried peat horizons which had resulted from damming during uplift events. These samples have been radiocarbon dated, and the results are shown in Table. 2.3. Most of the new radiocarbon ages, from this study, correlate well to those by Litchfield and Norris (2000), which gave us confidence in our results (Fig. 2.20). The exception is RV06, which has been contaminated with modern material and, most notably, B9(2) which was a single radiocarbon age from a buried wood horizon (Fig. 2.20).

OSL ages of original alluvium deposits were compared to McKellar's (unpublished) gravel radiocarbon age which was collected from a riverbank deposit at Nobles Stream (Table. 2.4). Our ages correlated well with McKellar's which gave us confidence in our OSL ages at Big Creek (Fig. 2.21).

These ages provide the critical information for understanding the event history of the Akatore Fault.

Table. 2.3 Litchfield and Norris (2000) radiocarbon ages along the Akatore Fault.

Location	Sample #	Description	Sampling method	Collection date	Calibration curve	Max. Age (Cal.cal. yr BP)	Min. Age (Cal.cal. yr BP)	Max Age (AD)	Min Age (AD)
Bull Creek	B9(1)	Peat layer at 1.1-1.3 m depth	Auger	2-Oct-97	SHCal	1287	1073	1073	1070
Bull Creek	B9(2)	Plant material in gravel at 3.6 m depth	Auger	2-Oct-97	SHCal	4080	3698	4080	3700
Nobles Stream	N1(4)	Wood in peat at 4.08-4.24 m	Auger?	12-Aug-98	SHCal	1519	1288	1520	1290
Nobles Stream	PN1	Wood in peat at 3.85 m depth	Percussion core	3-Sep-98	SHCal	1055	744	1060	740
Rocky Valley	R3	Wood and twigs at 0.7-0.8 m depth within brown clay	Auger	4-Sep-97	SHCal	1270	987	1270	990
Rocky Valley	R4(1)	Wood and peat at 1.4 m depth within grey silt	Auger	4-Sep-97	SHCal	1262	933	1260	930
Rocky Valley	R7(1)	Wood in peat at 1.75 m depth	Auger	2-Oct-97	SHCal	1177	936	1180	940



Fig. 2.20 Comparison between Litchfield and Norris (2000) (orange) and our study's radiocarbon ages (blue) from the Akatore Fault.

Table. 2.4 McKellar (unpublished) radiocarbon age along the Akatore Fault.

Location	Sample #	Description	Sampling method	Collection date	Calibration curve	Max. Age (Cal.cal. yr BP)	Min. Age (Cal.cal. yr BP)	Max Age (AD)	Min Age (AD)
Nobles Stream	H45/F9 532	Log not in growth position in clay lens in material of small flood plain	Riverbank exposure	12-Sep-63	SHCal	11164	10301	11160	10300

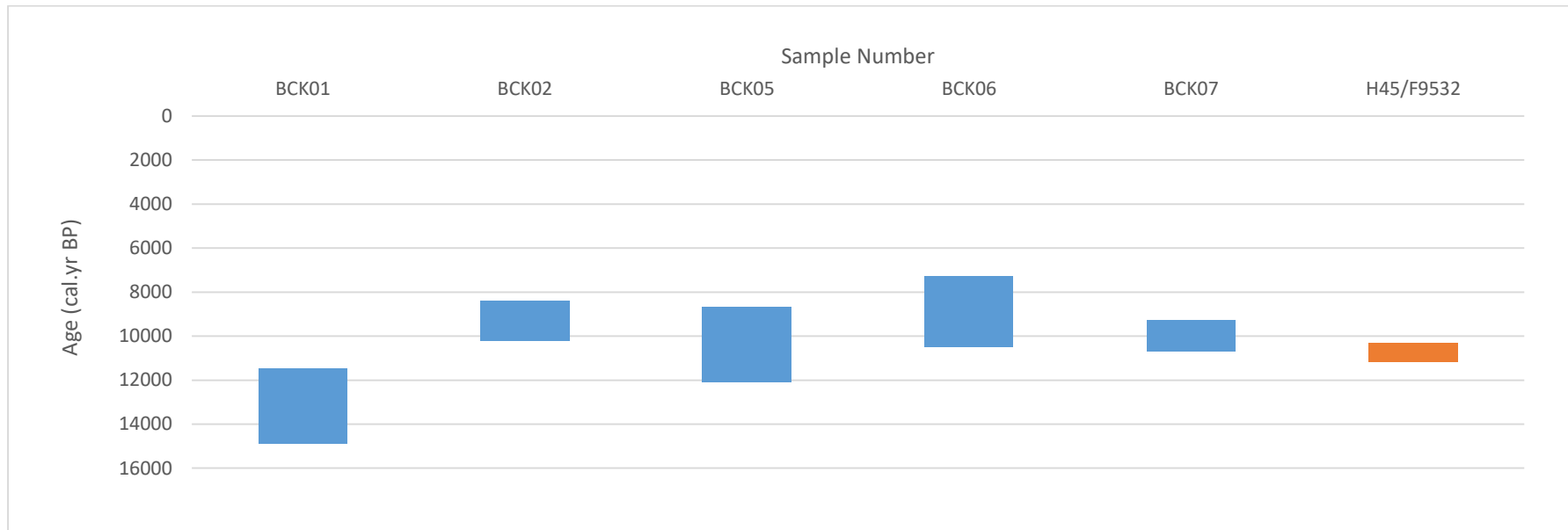


Fig. 2.21 Comparison between McKellar's gravel age (orange) and our study's OSL ages (blue) from the Akatore Fault.

2.6 BIG CREEK HOLOCENE EVENT HISTORY

2.6.1 Pre event stratigraphy and age

Bog cores by Mcglone and Wilmshurst (1999) suggested that the mid-late Holocene climate in East Otago was largely dry with periods of increased rainfall. Uplift would have resulted from the older Titri Fault, which was active from the middle – late Quaternary (Litchfield, 2001). The bottom of Big Creek is composed of schist basement. Gravel, sand and silt, overlies the schist, and have accumulated over time through fluvial processes. Sedimentary packages on the footwall and hanging wall of the fault indicated these fluvial deposits were present before the fault ruptured. The gravel (unit 5c in Fig. 2.16; 2.17) was the oldest sediment, deposited $13,200 \pm 1,700$ cal. yr BP. The gravel was varied in size, with clasts measured up to 20 cm in diameter. Interpretation of Hjulstrom's curve indicates that gravels of this size require high river velocities, ~ 2.5 m/ sec, to be transported (Hjulström, 1935). These velocities would have been acquired during flood / high discharge events, which were common during this time (Mcglone and Wilmshurst, 1999). The mottled silt on the footwall (unit 5a¹ with OSL age $10,400 \pm 1,700$ cal. yr BP) and the silt on the hanging wall (unit 5a² with OSL age $9,300 \pm 900$ cal. yr BP) have similar ages, therefore may have come from the same overall sedimentary package (Fig. 2.16: Fig. 2.17). Silts are indicative of a low energy environment (Hjulström, 1935), so the silts of unit 5a and 5b may have accumulated during periods of low discharge on Big Creek, under drier climatic conditions (Fig. 2.16; 2.17).

2.6.2 Antepenultimate event

The antepenultimate event was suggested by the formation of peat on the downthrown side of the fault. Peat is the accumulation of organic matter, which has only partially decayed as a result of water-saturated conditions (Keddy, 2010). Here, the peat (unit 4a in Fig. 2.16; 2.17) is aged $1,326 \pm 22$ cal. yr BP. The uplift of the hanging wall of the

fault could have led to damming of Big Creek. As a result, the footwall would have become waterlogged. Carbon material may have been trapped against the scarp as a result of the drainage path being blocked. The slow accumulation rate of peat, ~1 mm/yr, suggests Big Creek was blocked for some time before the scarp was eroded and the water found a path through the gorge (Martini et al., 2007). Reduced sedimentation, would have been conducive to the formation of peat. The silt, which lies below (unit 5a in Fig. 2.16; 2.17), pre-dates the uplift event which allows the first event to be constrained between $10,400 \pm 1,700$ and $1,326 \pm 22$ cal. yr BP. It is likely however, that the timing of this event is closer to the timing of peat deposition, so immediately prior to $1,326 \pm 22$ cal. yr BP.

2.6.3 Penultimate event

The penultimate event is suggested by the accumulation of silt above the peat, and the deposition of a colluvial wedge. The silt (unit 3c in Fig. 2.16; 2.17) is dated at $8,900 \pm 1,600$ cal. yr BP, which is significantly older than the peat (unit 4a in Fig. 2.16; 2.17, with radiocarbon age $1,326 \pm 22$ cal. yr BP), yet a similar age to the underlying mottled silt, (unit 5a with in Fig. 2.16; 2.17, radiocarbon age $10,400 \pm 1,700$ cal. yr BP). The silt has possibly been expelled syn-earthquake, and ‘squeezed out’ from the underlying mottled silt, resulting in the age inversion. The peat appears to thin out near the fault, and this may have been due to the underlying silt being ejected above the peat during the earthquake. The silt wedge on the footwall would have been expelled prior to development of a colluvial wedge over the silt. The peat provides an age for the second event of post $1,326 \pm 22$ cal. yr BP.

A colluvial wedge is formed at the base of an unstable scarp by an earthquake (McCalpin, 2009). Partial collapse of the Big Creek scarp would have produced a wedge shape on top of the silt and pre-faulted surface (Fig. 2.16; 2.17).

2.6.4 Most recent event

The colluvial wedge was distorted and it was in fault contact with the schist; this implies that there has been an additional event post the formation of the wedge. The third event would have thrust the hanging wall up over the footwall, resulting in the colluvium wedge on the downthrown side being in direct contact with the schist on the uplifted side. This event caused an unstable scarp and resulted in new colluvium being deposited on the pre-existing colluvial wedge.

The age of the colluvium (unit 3d in Fig. 2.16; 2.17, with OSL age $10,000 \pm 700$ cal. yr BP) is similar to the silt layer above the gravel (unit 5a in Fig. 2.16; 2.17, with OSL age $9,300 \pm 900$ cal. yr BP). This suggested the alluvium from the hanging wall has been reworked and re-deposited. The lack of sediment accumulation on the footwall during the most recent two events suggested that Big Creek was only dammed by the fault for a short amount of time before it was able to erode the scarp and re-establish a path out to sea.

Above the colluvium are unfaulted soil horizons (unit 1a, 2a and 2b in Fig. 2.16; 2.17; 2.19) which suggested the colluvium represents the last event on the Akatore Fault. This event can be correlated to ages from Rocky Valley trench, which also captured the most recent uplift event on the Akatore Fault. The soil horizon layers were planar, while the underlying silt and peat layers overturn towards the end of the trench, suggesting these have been faulted. By dating the peat (unit 4a in Fig. 2.16; 2.17), which has been deposited after the first event, and the base of the subsoil (unit 2a in Fig. 2.19), which is unfaulted, the most recent uplift event on the Akatore Fault can be constrained between $1,326 \pm 22$ and 776 ± 22 cal. yr BP. The second (penultimate) event also occurred within these dates.

2.6.5 Modern day

Over time, soil horizons have developed. Distinctive marks and fissures in the soil horizons suggested liquefaction has occurred at some time during activity on the fault. The time at which liquefaction has occurred cannot be constrained. The silts on either

side of the fault, which are part of the same sedimentary package (unit 5a and 5b in Fig. 2.16; 2.17), have different thicknesses. After the first earthquake, the thickness of the silt on the footwall was presumably buried and preserved, while the silt on the hanging wall was eroded during sequential earthquakes. Another differing characteristic, was the silt on the footwall was mottled (unit 5a² in Fig. 2.16; 2.17). This was related to the sediment drainage, and is often caused by water table fluctuations in the soil (Húska and Jurík). The grey colour of the silt implies soil saturation. Mottling of the silt may have been the result of continual damming of Big Creek.

After each of the Akatore Fault events Big Creek's flow has been briefly restricted prior to re-establishing a new, easier path through the scarp towards the coast. Past courses of Big Creek can be observed from paleochannels on the uplifted side of the paddock.

2.6.6 Comparison with Litchfield and Norris (2000)

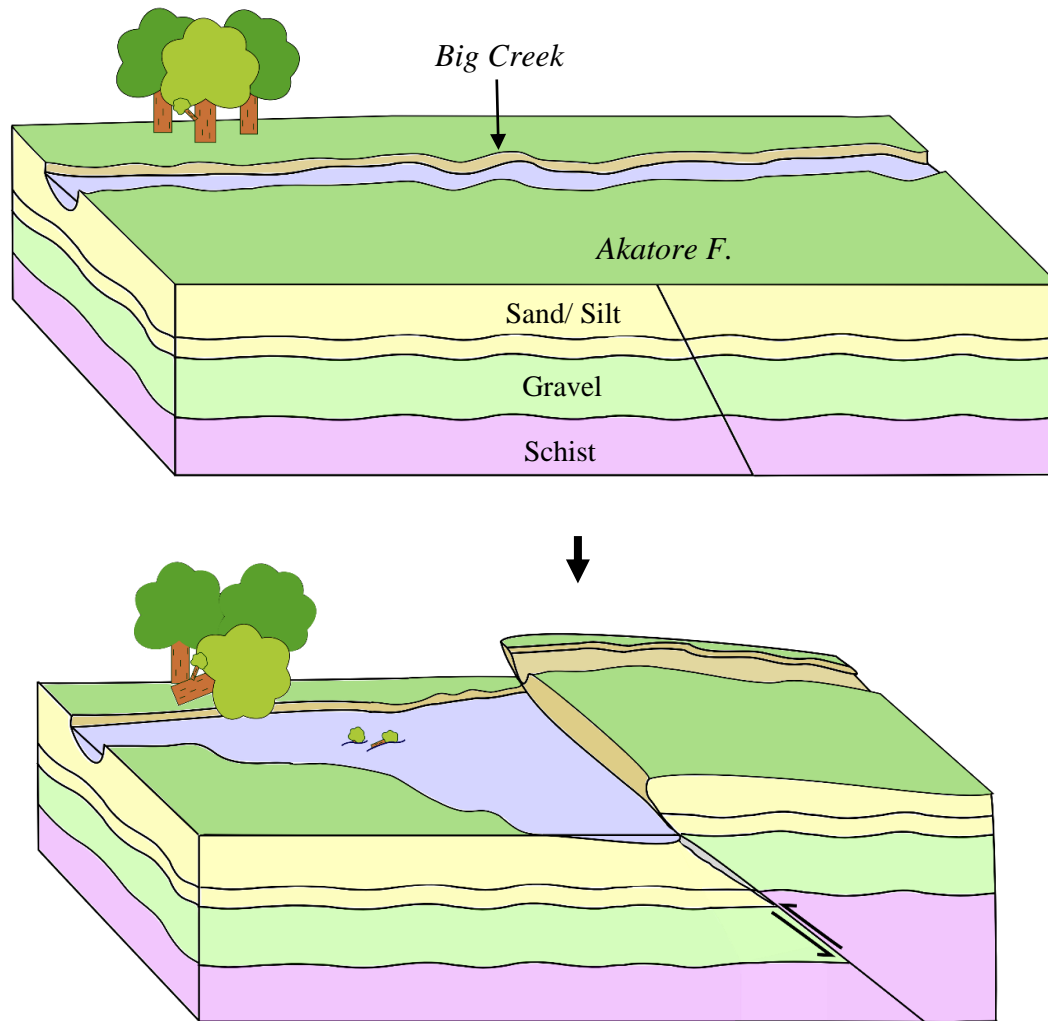
From this study we have determined that the oldest Holocene event occurred between $10,400 \pm 1,700$ and $1,326 \pm 22$ cal. yr BP, however this is likely to be closer to the later date.

The penultimate event determined from this study occurred between $1,326 \pm 22$ and 776 ± 22 cal. yr BP. Litchfield and Norris (2000) suggested an age post 3.8 ka. Our new results do not show a 3.8 ka event (Fig. 2.20).

The most recent event from, this study, also occurred between $1,326 \pm 22$ and 776 ± 22 cal. yr BP. Litchfield and Norris (2000) concluded an age of 1150 - 1000 yr BP which fits within our age range.

2.7 GRAPHICAL SUMMARY OF HOLOCENE EVENTS

During the late Holocene, three ground rupturing events have been interpreted from the trenches. Below is a sequence of schematic diagrams of Big Creek, demonstrating how the fault has behaved over time, resulting in its distinctive stratigraphy (Fig. 2.22). These have been constructed from trench observations and by dating key layers in the trench.



Pre event stratigraphy and age

Prior to the three Holocene earthquakes, sediments were transported through alluvium processes and deposited at the bottom of Big Creek.

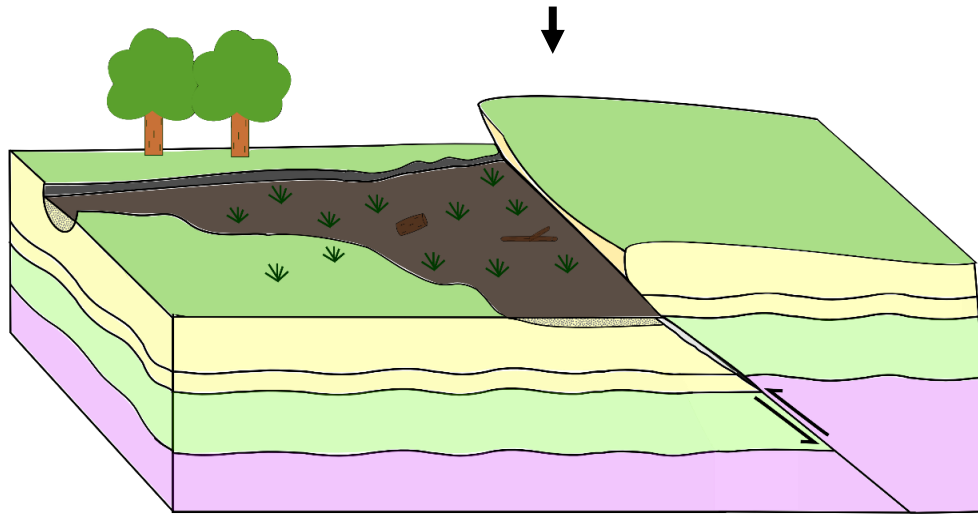
Age of alluvium deposition:

- Gravel: $13,200 \pm 1,700$ cal. yr BP.
- Silt: $9,850 \pm 1,300$ cal. yr BP

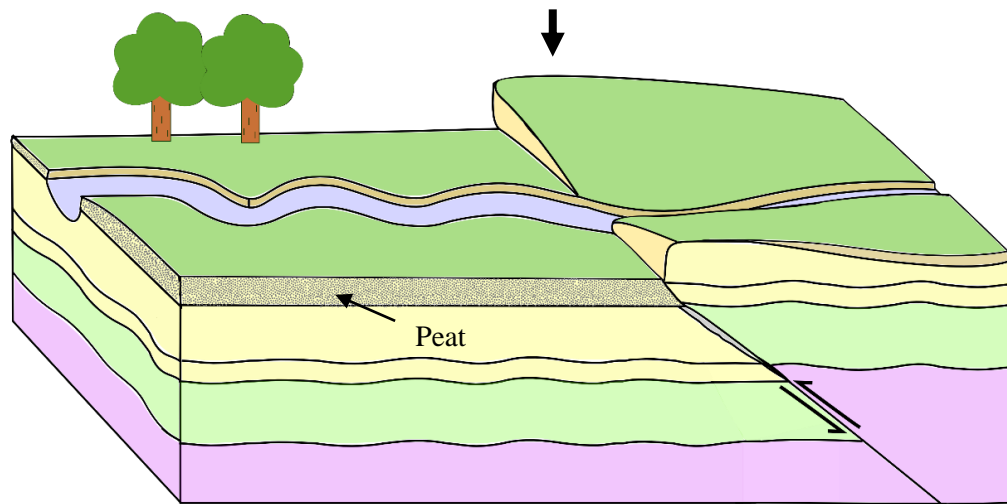
Antepenultimate event

Between $10,400 \pm 1,700$ and $1,326 \pm 22$ cal. yr BP the Akatore Fault ruptured, uplifting the hanging wall relative to the foot wall. This resulted in damming of Big Creek as its path was blocked by the fault scarp.

Fig. 2.22 Schematic diagrams illustrating the tectonic evolution of Big Creek.

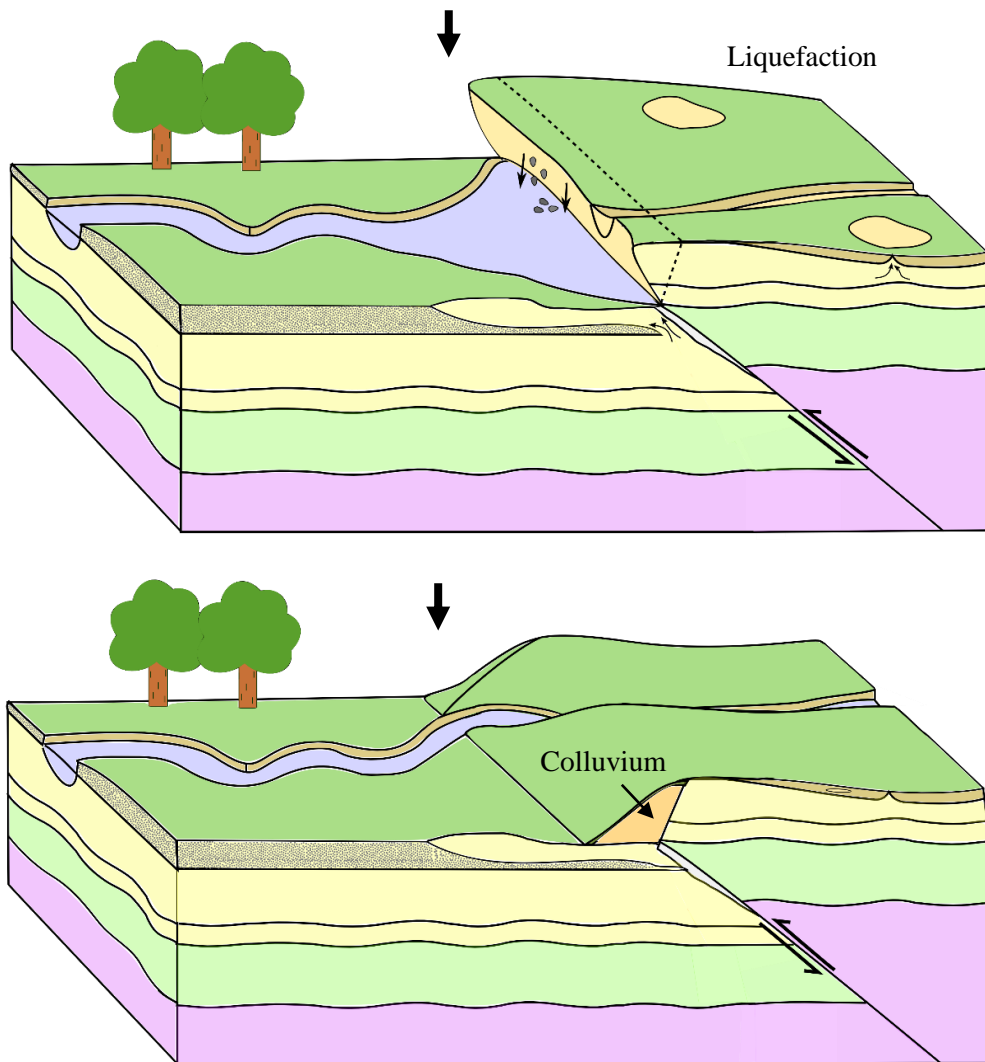


It took some time before the river eroded a channel through the scarp. During this time peat formed at the bottom of the scarp.



Eventually the river carved a new path through the fault scarp out towards the coast. The exposed scarp has led to thinning (weathering and erosion) of silt on the hanging wall.

Fig. 2.22. Continued.



Penultimate event

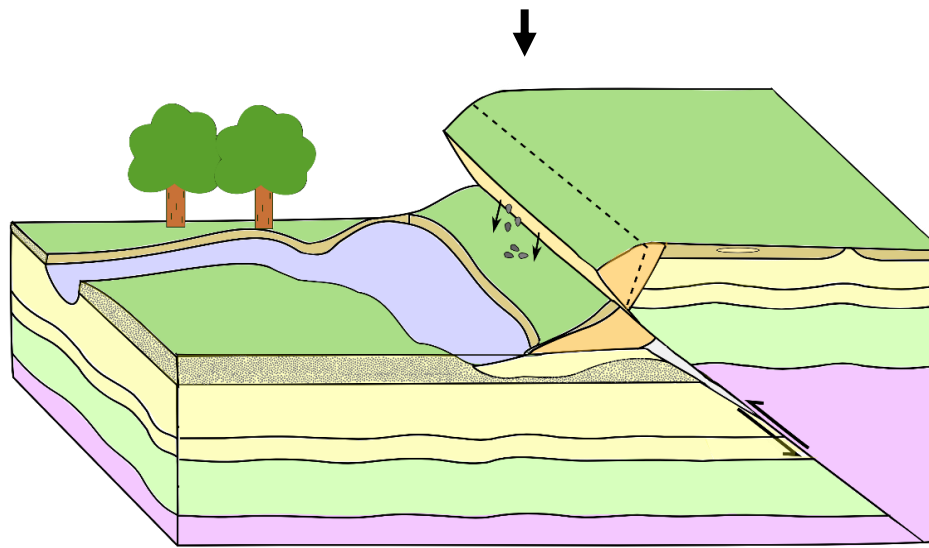
The penultimate event occurred between $1,326 \pm 22$ and 776 ± 22 cal. yr BP.

During this event the silt on the footwall has been ‘squeezed out’ and ejected on top of the peat syn-earthquake. The uplift caused an unstable scarp leading to a collapse of loose material onto the base of the scarp, forming a colluvial wedge.

Soil liquefaction appears to have occurred in the hanging wall, however the timing of its occurrence is unknown.

Over time the river was able to re-establish a path to the coast. Big Creek was dammed only for a short amount of time, relative to the first event, as peat formation did not occur.

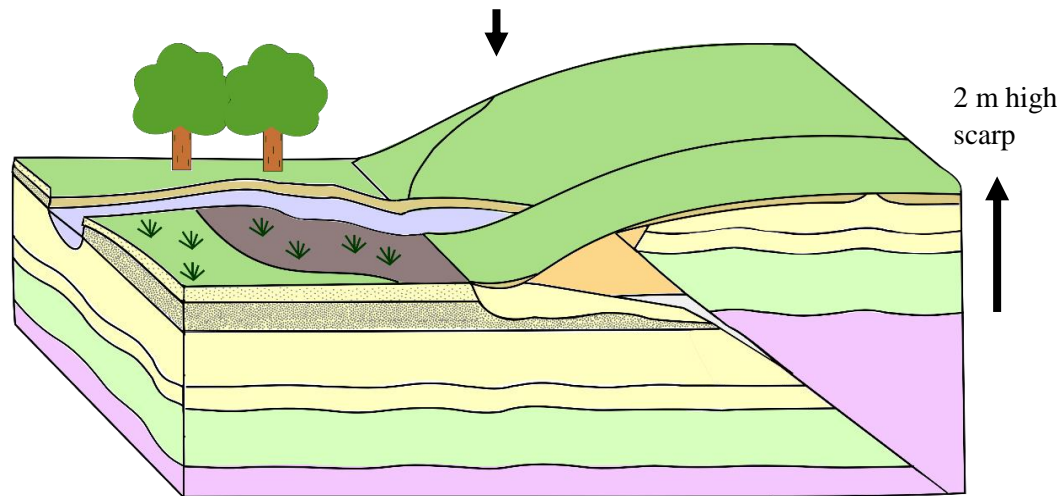
Fig 2.22. Continued.



Most recent event

The last event also occurred between $1,326 \pm 22$ and 776 ± 22 cal. yr BP.

During this event the colluvial wedge was faulted. The scarp was once again unstable leading to the re-deposition of the uplifted colluvium onto the base of the scarp.



A colluvial wedge has formed, and over time the river has carved its way back out to the coast. The continual damming of Big Creek has led to a depression on the footwall of the fault and mottling of the silt below. A depression in the land has resulted in a modern swamp setting around the base of the scarp.

Fig. 2.22 Continued.

Chapter 3

**FAULTED MARINE TERRACES AT
TAIERI MOUTH**



Aerial photograph of Taieri Mouth

(Source: Algie, 2016)

3.1 INTRODUCTORY REMARKS

At the north-eastern end, the Akatore Fault has a distinctive 2 m west facing scarp which can be observed in a paddock when looking east from Moturata Road (Fig. 3.1). This site is located 30 km south of Dunedin and it provides the last expression of the fault before it strikes offshore. It is of significance as here the Akatore Fault displaces the 125 ka marine terrace, therefore provides constraints on the longer term behaviour of the fault. In this chapter, I have reviewed previous paleoseismic studies of the marine terraces at Taieri Mouth. Then I have described field work we have undertaken, which includes geological observations, magnetic intensity and ground penetrating radar investigations, before discussing the results.

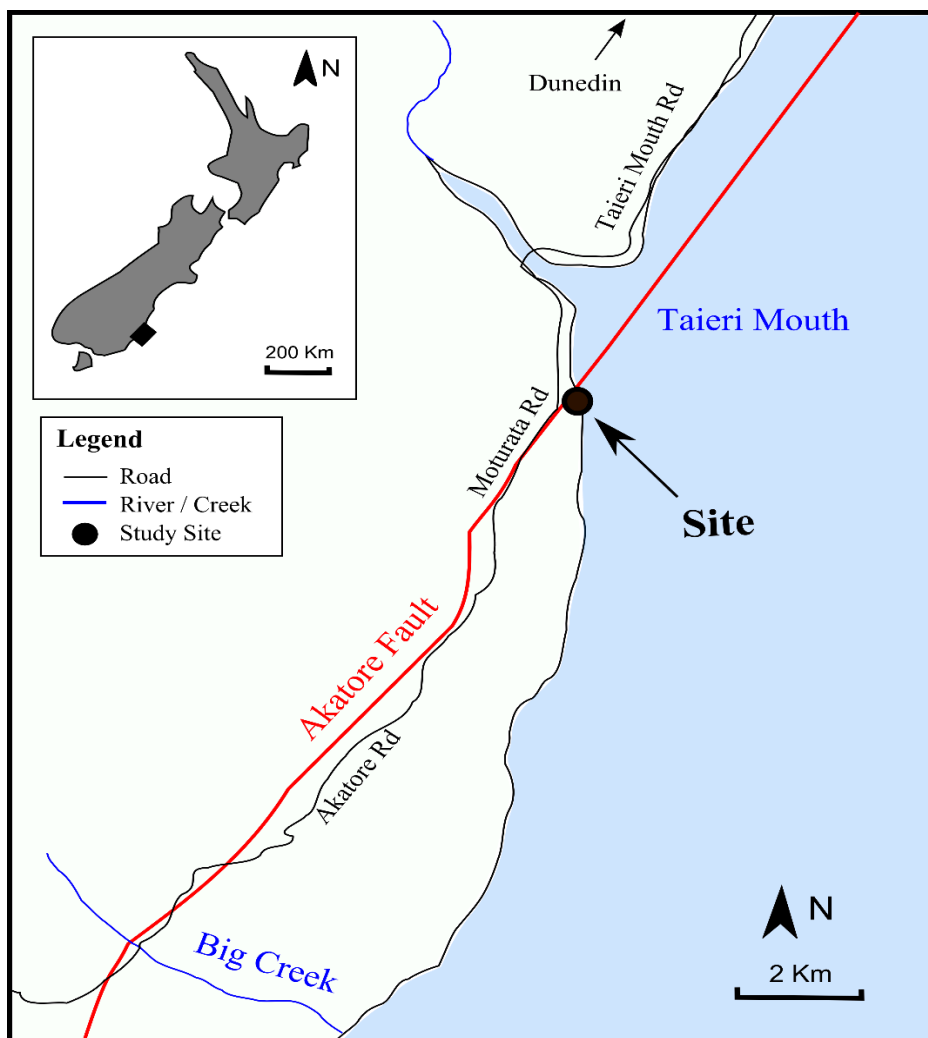


Fig. 3.1 Location of the Taieri Mouth site along the Akatore Fault (red).

3.2 MARINE TERRACES

Multiple marine terraces are observed along the coast in the Akatore Fault area. The series of marine terraces are well preserved around Taieri Mouth (Bishop and Turnbull, 1996; Barrell et al., 1998).

3.2.1 Previous work

Few geological studies were conducted at Taieri Mouth before the 1990's (Gage, 1953; Pillans, 1990). Those that have been undertaken have focused on the marine terraces, which are extensive in the area. The marine terraces have been investigated to gather information on past sea level stands (Gage, 1953). Early studies by Cotton (1957), acknowledged the relationship between tectonics and the marine terraces along the coast. Since terraces reached heights of over 50 - 60 m above the maximum sea level, tectonic activity must have played a role in their formation. At Taieri Mouth these terraces range from 2 – 120 m above average sea level (Barrell et al., 1998). East of the Akatore Fault, the youngest marine erosional surface is at ~ 5 m above sea level, at least 2 m higher than elsewhere along the coast (Bishop, 1994).

The marine terraces were dated at Taieri Mouth to gain information on past movement along the Akatore Fault (Litchfield and Lian, 2004; Rees-Jones et al., 2000). Motion on the fault has uplifted the marine terraces on the hanging wall (east). This was evident as the marine terraces do not appear to be well aligned across the fault (Barrell et al., 1998).

Luminescence dating of the marine terraces provided an age for the burial of the sediments. Samples were dated using Optical Luminescence, with one sample dated using Thermoluminescence (TL); TL is a luminescence dating technique where the minerals are heated during the measurement (Rhodes, 2011). Results are shown in Table. 3.1.

These samples were collected along the east (uplifted) side of the Akatore Fault, south of Taieri Mouth (Fig. 3.2). Here Otago Schist basement, which has been eroded into a wave cut platform, was observed. Overlying this was red / orange coarse grained sands, ~1 m thick and then fine yellow sands, ~1.5 m thick covered with loess (~1 m).

Loess is extensive throughout eastern South Island, on late Pleistocene and older terraces, it has been transported and deposited by wind during glaciations (Fig. 3.2; Eden and Hammond, 2003). The loess has been deposited at ~ 20 ka, during the Last Glacial Maximum; this is a similar age to that recorded elsewhere in New Zealand (Berryman, 1993; Eden and Hammond, 2003).

The red / orange coarse sands have been interpreted as beach sands as they are deposited on top of a shore platform, and have similar characteristics to modern day sands. The beach sands are interpreted to have been deposited during a high-stand of the last interglacial (~80 ka), when sea level was 4 - 6 m higher than present day (Harmon et al., 1983; Rees-Jones et al., 2000). After the sea retreated the younger fine sand was deposited. Since these sediments are currently at higher elevation than present day sand levels, significant uplift of the marine terraces must have occurred within this area. The youthful appearance of the scarp suggests recent movement along the Akatore Fault (Rees-Jones et al., 2000).

The beach sands were re-dated by Litchfield and Lian (2004; Fig. 3.2). These ages suggest the beach sands correspond to the 125 ka last interglacial peak high stand, rather than the previously interpreted 80 ka. These beach sands are ~ 3 m thick, overlying ~ 4 m (above high sea level) of basement and capped with loess 1 m thick. These sands were sampled 1 m up from the basement where their ages most likely correspond to the terrace formation (Fig 3.2).

The uplifted block of the 125 ka terrace has a relatively low elevation of 5 - 20 m above high sea level, furthermore, this terrace is offset by 2 - 4 m across the fault. These findings suggest all of the uplift on the Akatore Fault has been wholly accounted for during the Holocene events (Litchfield and Norris, 2000; Litchfield and Lian, 2004). Litchfield and Lian (2004) suggested the last Holocene event (the penultimate event) occurred post 3.8 ka, their findings imply that there has been little or no uplift on the Akatore Fault 125 – 3.8 ka.

Table 3.1 Luminescence ages of sands and loess south of Taieri Mouth, East Otago. Samples are in stratigraphic order.

Sample Number	Unit Description	Method	Age (ka)	Reference
NZ8	Loess	OSL	19 ± 7 22 ± 7	Rees-Jones et al. (2000)
B1*	Loess	OSL	28 ± 7	Barrell et al. (1998)
NZ9	Yellow fine sand	OSL	47 ± 15	Rees-Jones et al. (2000)
B2*	Yellow fine sand	OSL	57 ± 18	Barrell et al. (1998)
NZ10	Red/orange coarse sand	OSL	71 ± 14	Rees-Jones et al. (2000)
B2*	Red/orange coarse sand	OSL	87 ± 19	Barrell et al. (1998)
TBE1	Red/orange coarse sand	OSL	117 ± 12	Litchfield and Lian (2004)
W2857	Red/orange coarse sand	TL	117 ± 13	Litchfield and Norris (2000)

* Not original sample codes.

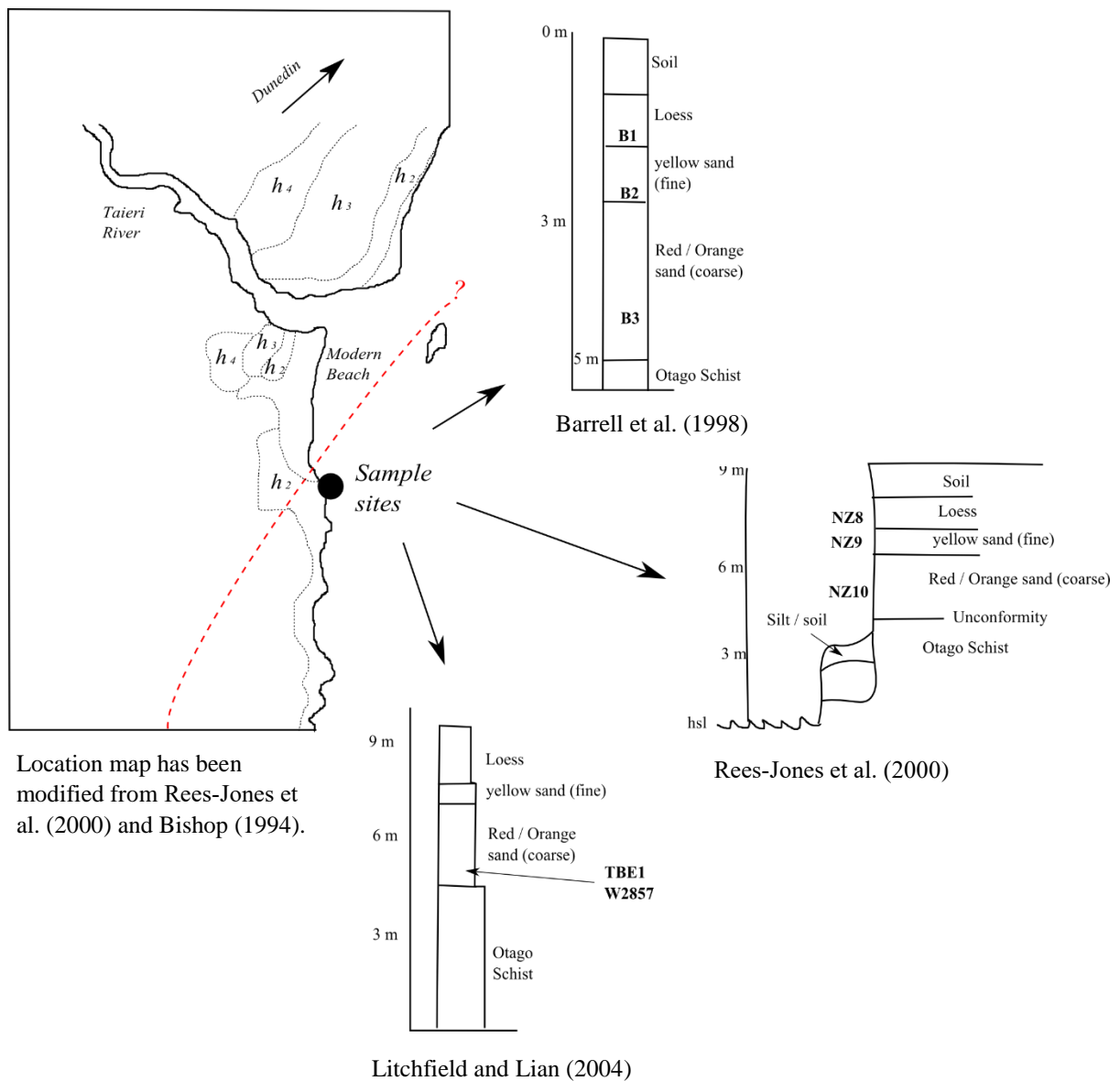


Fig. 3.2 Sample locations and corresponding logs of Pleistocene terraces, h (larger numbers are associated with older terraces). Text in bold indicates the sample number. The red dashed line is the Akatore Fault.

3.3 FIELD WORK

Geophysical data (magnetic intensity and ground penetrating radar data) were collected, with the help from the undergraduate “Geophysics of the Earth” students (GEOL 251/361), throughout the paddock, south of Taieri Mouth, as an attempt to image the subsurface expression of the Akatore Fault. Assessing the characteristics of the fault before it strikes offshore has provided information on the activity of the fault in the north-eastern areas, and therefore, the hazard it poses to Dunedin and elsewhere.

3.3.1 Site geomorphology

The Akatore Fault is evident from the ~ 2 m scarp which crosses the large paddock (Fig. 3.3; 3.4.). Towards the south the fault strikes ~ 60°, it then slightly alters its orientation and strikes ~40° at the northern end. Towards the north of the paddock the fault moves offshore 150 m NE of the large tree in the paddock (Fig. 3.3). The fault is expressed in the near-shore areas of Taieri Mouth by a north-east alignment of schist reefs and an island (Fig. 3.3). To the south-west the fault scarp is present and the peneplain uplift on the hanging wall of the fault progressively increases in height.



Fig. 3.3 Bird's eye view of the Taieri mouth site (original image sourced from Google Maps). **A.** The Taieri Mouth site with the Akatore Fault scarp annotated in red. **B.** The black box marks where the fieldwork was conducted. The fault can be projected offshore (arrow) by the exposed schist outcrops. The schist outcrops and Taieri Island are on the hanging wall of the fault.



Fig. 3.4 Close up of the distinctive ~ 2 m Akatore Fault scarp at the Taieri mouth site. **A.** View is to the south. **B.** View is to the north.

3.3.2 Geological observations

On the 12th of August we investigated the Taieri Mouth site to see if we could measure the offset of units across the fault. On the coast (GR: -46.07, 170.12) a marine cliff exposes friable and weathered Otago Schist bedrock. The Otago Schist forms part of the Chrystal Beach Complex (Nelson, 1982) which is an accretionary melange in south-east Otago, composed of bedrock with sandstone-shale and volcanogenic affinity (Fagereng and Cooper, 2010; Nelson, 1982). Within the Otago Schist at Taieri Mouth are altered metabasalts containing microcrystalline pillow structures. The mineral assemblage is largely epidote, actinolite, pumpellyite, albite and chlorite, providing the Otago Schist outcrop with its green colour (Pitcairn et al., 2015). The Otago Schist is ~ 6 m below the top of the cliff and is concealed by modern and paleo-beach sands elsewhere. Above the Otago Schist are schist-derived gravels that are overlain by a thick layer of sand, and capped by loess (Fig. 3.6). The Otago Schist was not exposed on the footwall, therefore we looked for correlatable horizons in the tertiary sands to constrain the long-term behaviour of the fault.

A riser truncates the marine terrace and fault scarp to the north at GR: -46.07, 170.12. Here, we observed an outcrop of sands and loess within the road cuttings (Fig. 3.7a). We excavated the exposed sediments by shovel. Within the road cuttings and immediately below the faulted marine terrace surface was a thick bed of well consolidated whitish loess. The loess had vertical joints, which were cracks caused by faulting. The loess is ~ 20 ka in age (Table. 3.1.), and is associated with the low stand of the last glaciation (Berryman, 1993). The fault was evident by the change in height at the top of the loess (Fig. 3.7a). The loess was overlying well sorted, loose – poorly consolidated mottled sands below, which were orange to red in colour. These sands vary in age and are associated with the last interglacial high stands, 80 – 125 ka (Table. 3.1; Berryman, 1993). There was a gradual transition between the sands and loess, which were separated by a layer of gritty iron cement (Fig. 3.5.). North-west of the fault scarp, similar sediments were observed on the footwall of the fault which correlate with the hanging wall (Fig. 3.7b). The cementation caused part of the sediments to be well-expressed in the footwall exposure (Fig. 3.7b). These sediments had an equivalent gritty cemented layer to that of the hanging wall. By correlating the sedimentary relations across the fault

(the cemented gritty iron stained layers and underlying sandy sediments) it was estimated that there has been approximately 1 – 2 m of throw across the fault. The loess on the hanging wall was ~ 1.7 m thick, while the loess on the footwall was ~ 1.1 m thick, suggesting there has been some erosion of the loess on the footwall. It was estimated that there was a minimum of 1 m throw across the fault, taking into account the potential erosion prior to the deposition of the loess.

The height of this offset (1 – 2 m) was similar to that of the fault scarp in the paddock, suggesting a minimum of 1 – 2 m of scarp development since the formation of the marine terrace (~125 ka). Furthermore the youngest Holocene marine terrace is 1 - 3 m above sea level along most of the coast (Litchfield and Norris, 2000), however, east of the Akatore Fault the surface is 5 m above sea level suggesting 2 - 4 m of uplift along the fault (Bishop, 1994, Bishop and Turnbull, 1996). Weathering and erosion may have played a part in reducing the faulted topography but, if not, our observation was simply that there may have only been the 2 - 4 m of scarp development since the marine terrace was formed. Since the Big Creek trench results indicated similar displacements achieved over three Holocene earthquakes, it was plausible that the scarp development has happened by way of these same three Holocene events, with nothing occurring for a long period prior. Specifically, three ground rupturing events in the recent Holocene, and none since the formation of the marine terrace at ~125 ka.

Our findings support those from Litchfield and Lian (2000) who suggested little to no uplift between 125 – 3.8 ka; however we have determined, from our paleoseismic data at Big Creek, that the oldest Holocene uplift event occurred $10,400 \pm 1,700$ cal. yr BP, therefore suggesting the Akatore Fault was in a period of quiescence between 125 – 10 ka.



Fig. 3.5 A close up of the gritty, iron cement separating the loess (above) from the underlying (presumably Tertiary) sands.

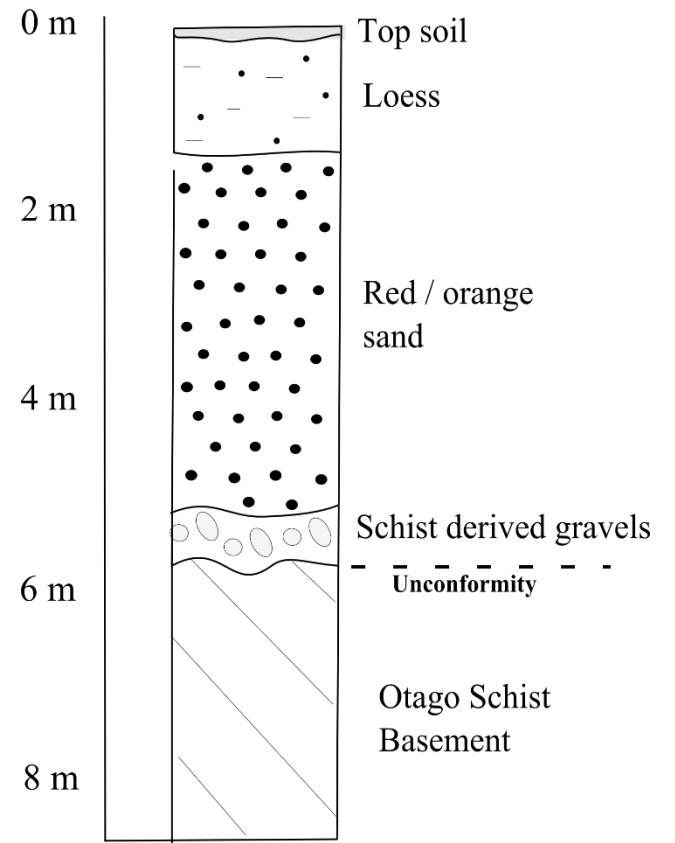


Fig. 3.6 Beach outcrop south of Taieri Mouth; GR: -46.07, 170.20, facing south-west. Key features are annotated on the log. “Fat Lamb” for scale.

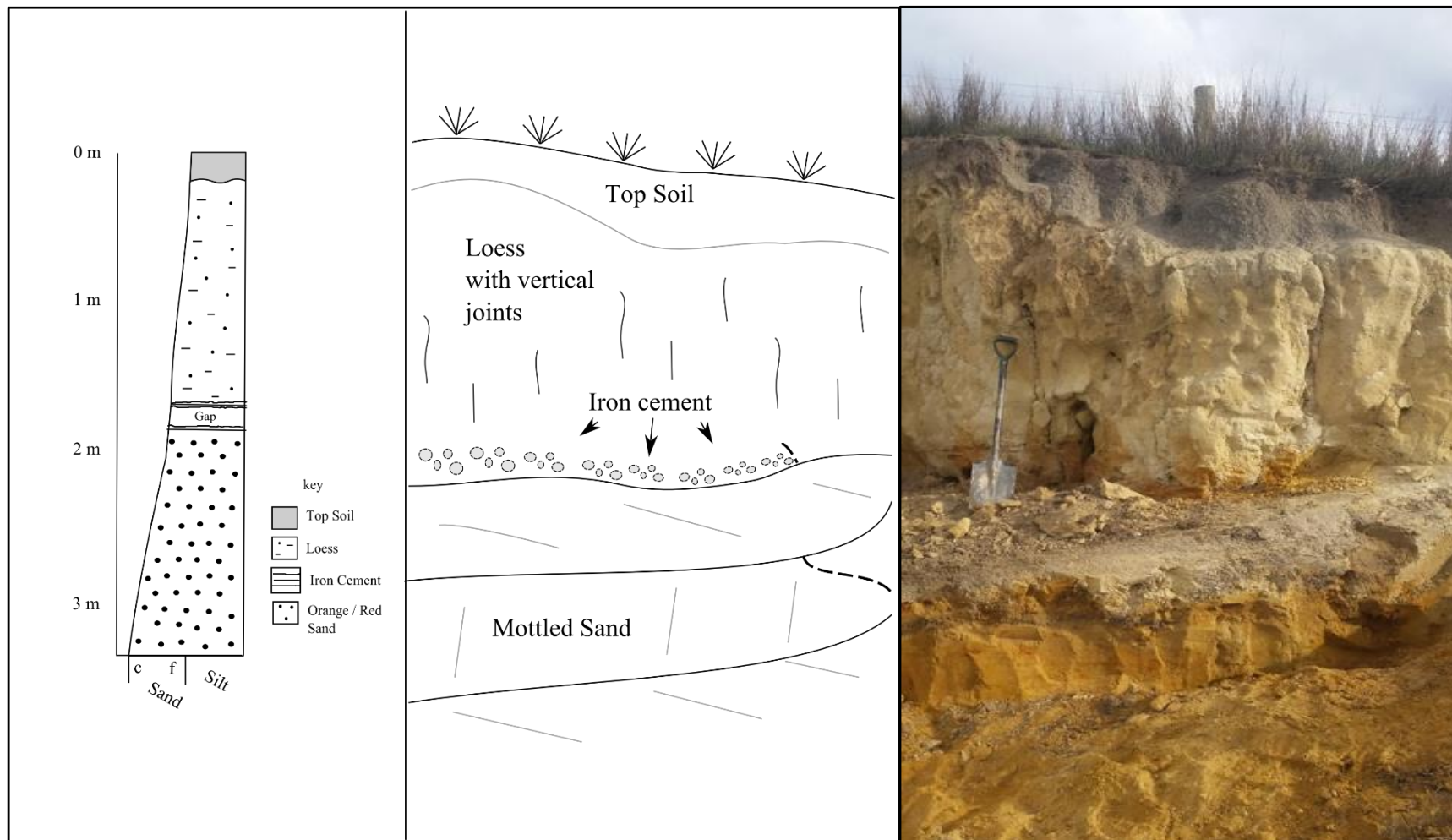


Fig. 3.71a Loess and sands within road cuttings primarily on the east side of the fault (hanging wall), south of Taieri Mouth. The slope of the scarp can be observed in the skyline and the fault is annotated by black dashed lines.

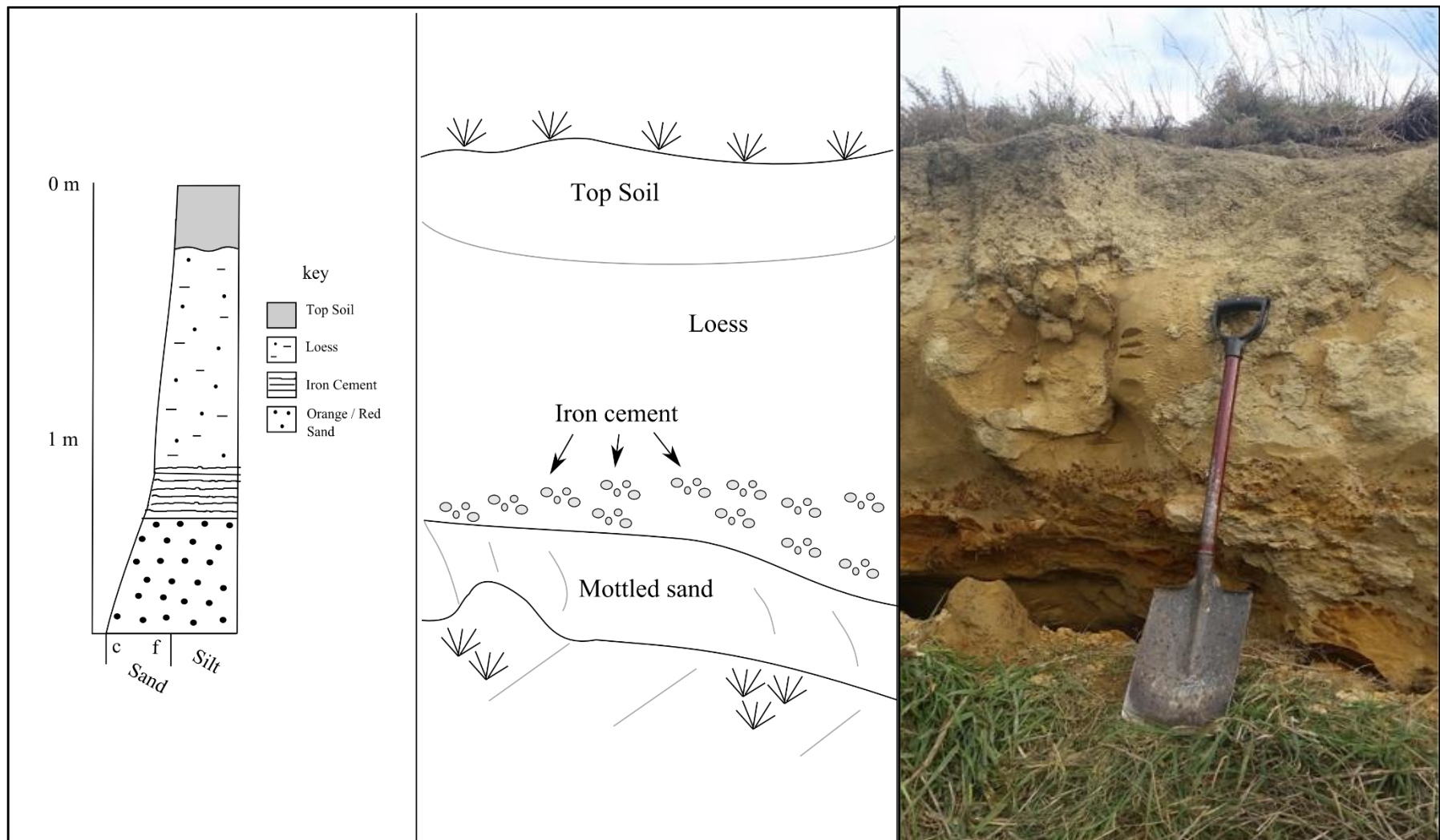


Fig. 3.7b Loess and sands within road cuttings on the west side of the fault (footwall), south of Taieri Mouth.

3.3.3 Magnetic intensity

Two weekends in September were spent at Taieri Mouth collecting field data as part of the GEOL 261/361 field school in which the author was a teaching assistant. The students ran a geophysical survey across the Akatore Fault scarp and collected magnetic intensity data.

Magnetic surveys can be used to investigate the magnetic properties of the underlying rocks. A magnetometer was used to measure the strength of the magnetic field in a transect across the scarp (Mariita, 2007; Likkason, 2014). Variations, referred to as magnetic anomalies, are related to the underlying rock's magnetic susceptibility. A high anomaly is where the magnetic field is higher than expected and a low anomaly is where the magnetic field is lower than expected. The students collected multiple lines over the two weekends (Fig. 3.8.).

Results and interpretation. The results from the survey showed areas of magnetic anomalies. The net variance in the magnetic field strength was 72 nT (Fig. 3.9.). By comparing the results from the four days, we found that there were high magnetic anomalies that do not appear on sequential days. These outliers are most likely picking up metal objects (belts, shoes, keys etc.) which may have been in the vicinity of the survey at the time (Mariita, 2007). The small red anomalies which appear on the centre of the maps were associated with the electric fence which was located in the middle of the paddock (Fig. 3.9).

Ignoring these outliers, we can see that majority of the highly magnetic anomalies were located to the east of the paddock, whereas the lower magnetic anomalies were located to the west. The fairly abrupt change in magnetic intensity suggested that the fault had been crossed. On the hanging wall we expected to see the schist basement uplifted relative to the footwall. Metamorphic rocks tend to have greater magnetic susceptibilities than sediments, so the magnetic intensity would be expected to be significantly different on either side of the fault. The minerals which make up most sediments (e.g. quartz and calcite) have very weak, negative magnetic susceptibilities (Clark, 1997). The magnetic survey, hence provides a clear image of this geological boundary (Fig. 3.9). Furthermore, there was a second high magnetic intensity area to the east, separated by a small area of lower magnetic intensity. This was roughly parallel to the main fault scarp, suggesting it

was a subsidiary scarp that has accommodated some of the displacement (Fig. 3.9). This secondary scarp can also be detected by an increase in the elevation (see Lidar Image in Fig. 3.11).

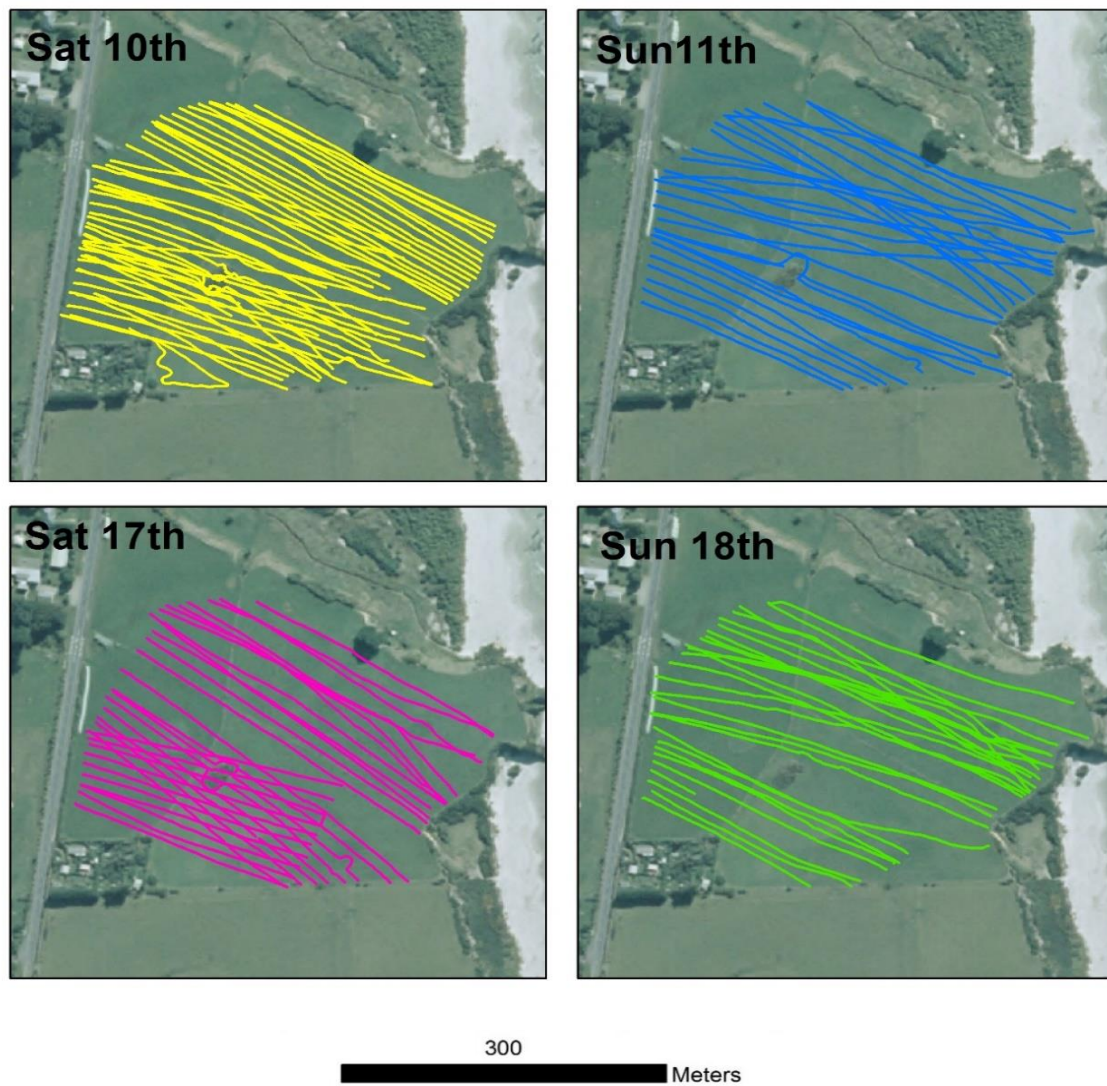


Fig. 3.8 Magnetic survey lines which collected magnetic intensity data over four days at the Taieri Mouth site. Data collected by students on the GEOL 261/361 field school and compiled by Hamish Bowman.

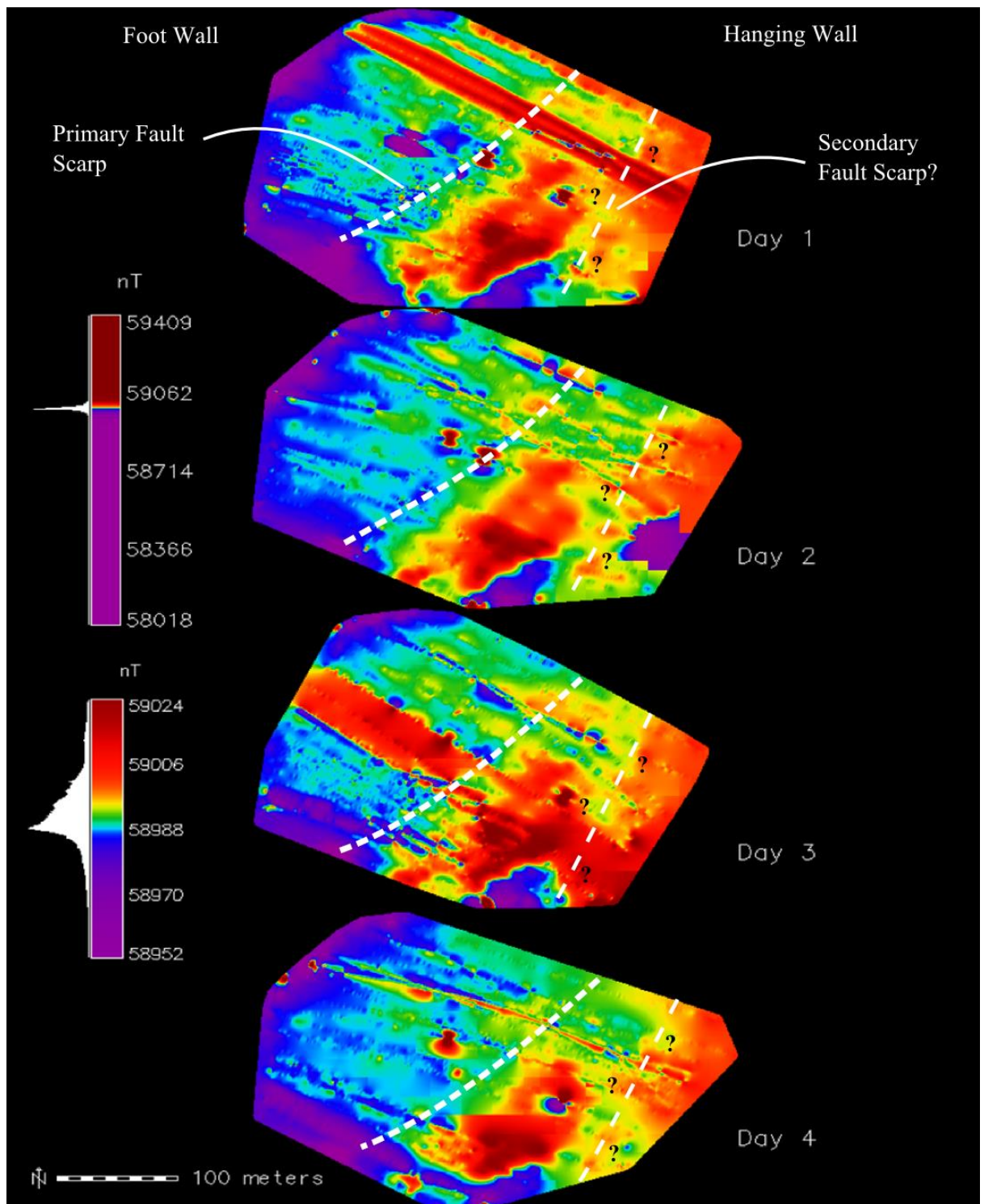


Fig. 3.9 Annotated magnetic intensity results from the lines collected in Fig. 3.8 (above). The dark red and dark purple areas are associated with high and low magnetic anomalies, respectively.

3.3.4 Ground penetrating radar (GPR)

GPR has been utilised as an attempt to image the subsurface geology across the scarp. GPR equipment images the subsurface by sending out electromagnetic pulses into the ground from a transmitter at the surface. The electromagnetic pulses are reflected back towards the surface and recorded by a receiver. The reflection happens when the pulses come into contact with the boundary between two materials with different dielectric properties. These differences depend on the water content, rock type, porosity, compaction etc. (Jol and Bristow, 2003). GPR has become a popular method in subsurface geology studies, as it is portable, light weight, and digital; the GPR data can be collected continuously and can be viewed in real time in the field (Jol and Bristow, 2003).

On the 11th of October 2016, two GPR lines were collected at the Taieri Mouth site in order. We collected two lines rather than just one to enable more accurate interpretations. The GPR equipment was supplied from the Geography Department of Otago University. We used 100 MHz paddles (recorders), and our hopes were that we would be able to image down to the schist bedrock. The lower the frequency of the transmitter the greater the depth of penetration, but also the reduction in quality (Jol and Bristow, 2003). We collected our data after a week of damp weather which may have enhanced the radar signal (Jol and Bristow, 2003). Our previous observations along the cliff face, showed that the bedrock is at ~6 m in depth on the hanging wall of the fault. The two lines were collected across the fault scarp at right angles to the scarp (Fig. 3.10; 3.11). The lines were both 139 m long. Starting on the hanging wall, each measurement was collected at 0.5 m intervals, holding the transmitter and receiver 1 m apart. The first line (line01) was collected parallel to second line (line02), at ~ 50 m apart. The fault was clearly shown in the raw GPR data.

Once the fieldwork was completed, the data was imported into Ekko View to produce an image of the subsurface. To produce an image a velocity had to be selected. The velocity value was derived from diffractions at the lower band of reflectivity in the data, which was hoped to provide a good average of the section. The velocity was set to 0.068 m/ns. From field observations we expected the subsurface to consist primarily of loess, sands and schist. In the literature a velocity of 0.06 m/ns was seen to be associated with moist

loamy soils. This average velocity is commonly used in sedimentological studies (Jol and Bristow, 2003).

This average velocity was used to convert TWT to an approximate depth. The GPR equipment has collected data up to ~6 m in depth. The topography was added to all profiles by overlying elevation values from the Lidar images onto the top of the GPR data. The topography was added in Ekko View and smoothed, which produced the final picture. Processing was kept to a minimum to keep the integrity of the data.



Fig. 3.10 The setup of our GPR survey. A 140 m long tape is laid out across the fault scarp and the paddles are placed 1 m apart.

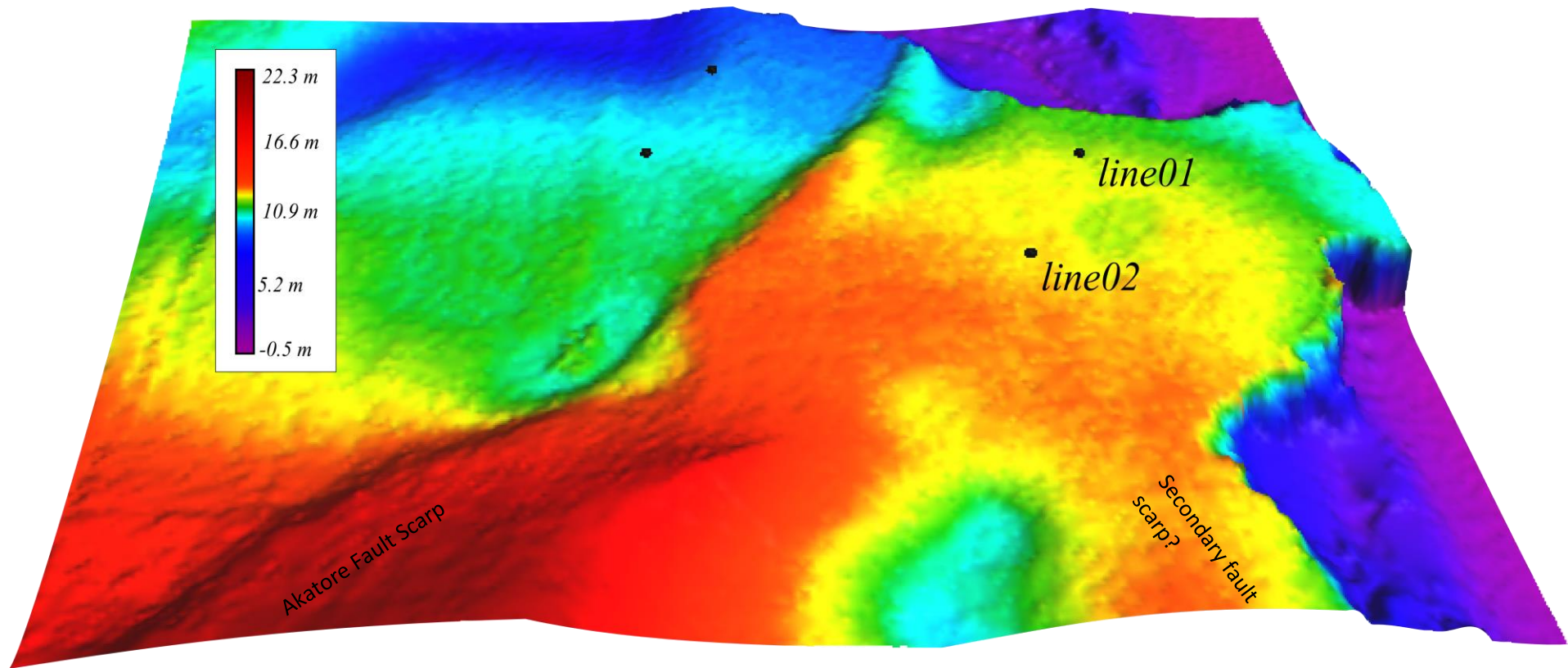


Fig. 3.11 Lidar image of Taieri Mouth paddock. The fault scarp is well defined from the sudden change in elevation. The two GPR lines are annotated with black dots highlighting their extent. The lines were collected right (east) to left (west). The Lidar image is sourced from the Otago Regional Council.

Results and interpretation. In general, the interpretations of the layers within the GPR profile correlate well with what was observed and what has been documented previously (e.g. Rees-Jones et al., 2000; Barrell et al., 1998; Litchfield and Lian, 2004).

The data shows that there is a ~ 2 m drop in elevation across the scarp (Fig. 3.13; 3.14). Line02, which was collected to the south of line01, shows that the scarp is increasing in height towards this direction. Apart from the elevation variation, the two profiles have very similar characteristics within the subsurface hence the two profiles have been interpreted together (Fig. 3.13; 3.14).

The first strong reflection in the data correlated to the boundary between the air and the ground, 0 – 55 ns (Fig. 3.13; 3.14). This was a distinct first reflection as energy has low attenuation and travels at high velocity within the air (Jol and Bristow, 2003). Below the surface was a unit of loess. This unit was massive and homogenous therefore reflections were sparse (Fig. 3.13; 3.14; Ékes and Friele, 2003). The loess unit was thicker on the hanging wall than the footwall most likely a consequence of erosion on the footwall. On the profile the loess on the hanging wall is ~ 2 m in thickness. The loess is ≤ 1 m in thickness on the footwall, however it is difficult to distinguish in this resolution of the GPR data. The 1 - 2 m thickness of the loess agrees with previous field observations. Below the loess was the next strong reflection between 50 – 100 ns (Fig. 3.13; 3.14). From our observations we have interpreted this interference pattern as the boundary between the loess and the mottled sand below. At the boundary between these two layers we observed layers and clasts of iron cement. The iron cement was considered to be responsible for the strong reflection. Within the mottled sand unit were multiple small wave diffractions, some were continuous and some were intermittent. These were most evident on the footwall. These may be bedding plains within the sand. This unit was 2 – 4 m thick which is similar to that observed on the beach cliff (Fig. 3.6).

The last strong reflection was only observed on the footwall at ~ 150 ns (Fig. 3.13; 3.14). This reflection was difficult to interpret. It may have correlated to the schist bedrock, as this was a similar depth to where we observed the bed rock on the coastal cliff and similar to what was recorded in the literature (Fig. 3.6; e.g. Barrell et al., 1998; Litchfield and Lian, 2004; Rees-Jones et al., 2000). It was speculated that this unit may correspond to a faint reflection on the hanging wall which has similar characteristics at ~ 100 ns (Fig. 3.13; 3.14). Below this unit was a weak hyperbolic reflection at 200 ns, between 60 and

70 m along the profile. This is best observed in line01 (Fig. 3.13). This hyperbolic feature is a common characteristic associated with a localised feature, in this case the GPR equipment has reflected off the vehicle that we drove to the site. There was no continuous sub horizontal strong reflection throughout the profile, this indicates that we have not crossed the water table.

In these profiles the Akatore Fault was clearly depicted by the interruption of reflectors and the tilting of the units near the fault. This occurs 70 – 90 m along the profile (Fig. 3.13; 3.14). Near the fault the reflectors were faint, suggesting that the faulting has disturbed the surrounding sediments. Assuming the faint reflection at ~ 100 ns corresponds to the strong reflection at ~ 150 ns, and that the fault is dipping at a 41° (dip is from the penultimate event at Big Creek) this would suggest ~ 4 m of total displacement from the offset of the bedrock (Fig. 3.12). This total displacement is similar to that measured from the Big Creek trench (~5 m). These results support our findings that all of the displacement which has occurred since the formation of the 125 ka marine terrace can wholly be accounted for by the three Holocene earthquakes we measured at Big Creek.

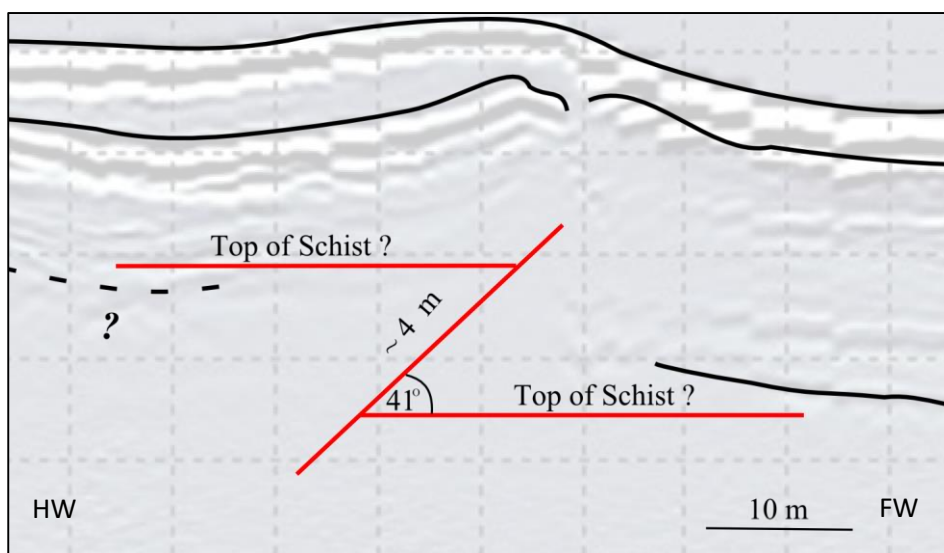


Fig. 3.12 GPR profile of the fault zone suggesting ~ 4 m of offset of the bedrock across the fault (assuming the deepest reflection on the hanging wall and footwall are from the top of the schist).

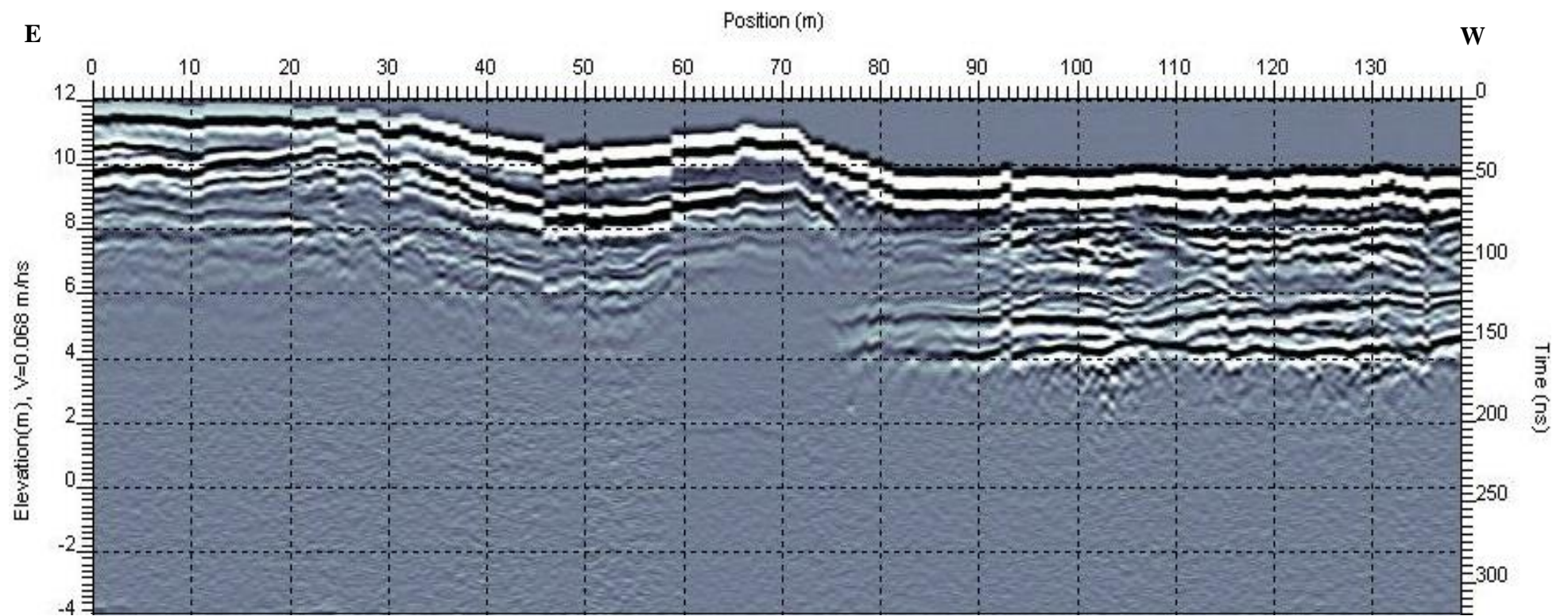


Fig. 3.13a GPR Line 01 Profile with topography corrected. Exported from EkkoView.

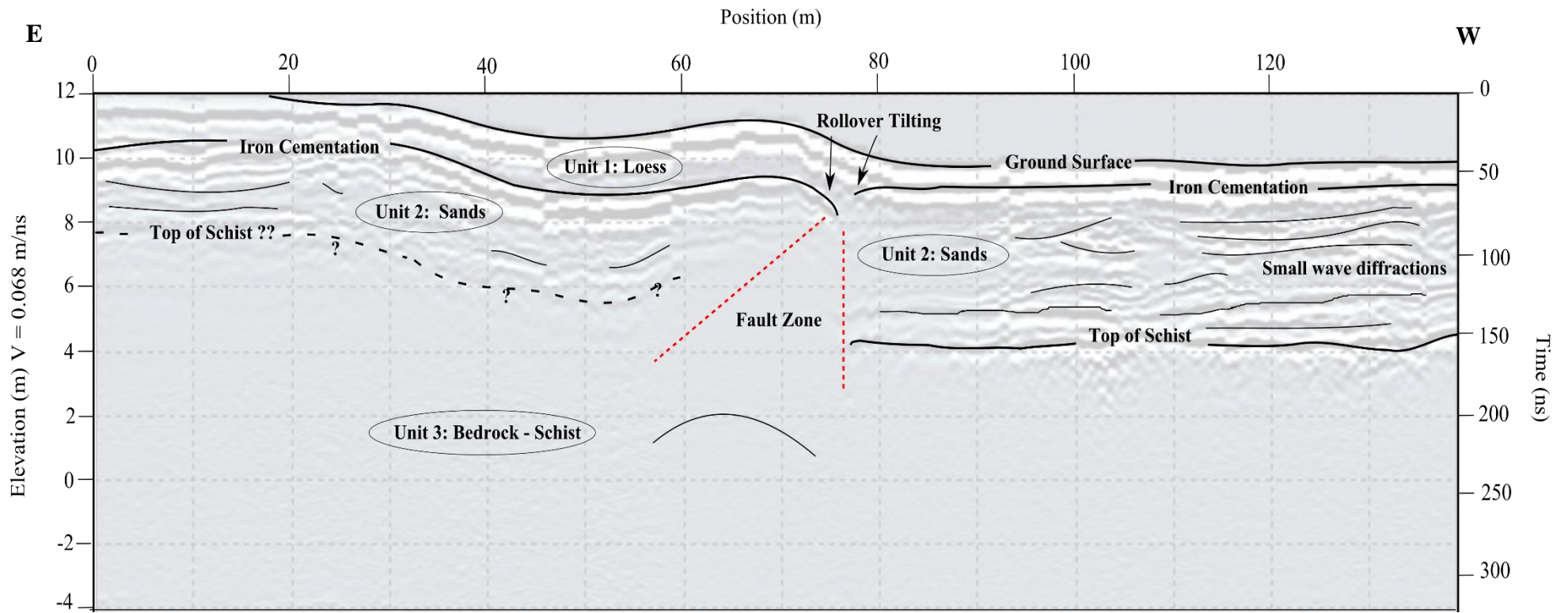


Fig. 3.13b Annotated diagram of GPR Line 01 profile (Fig.3.13a), showing key features.

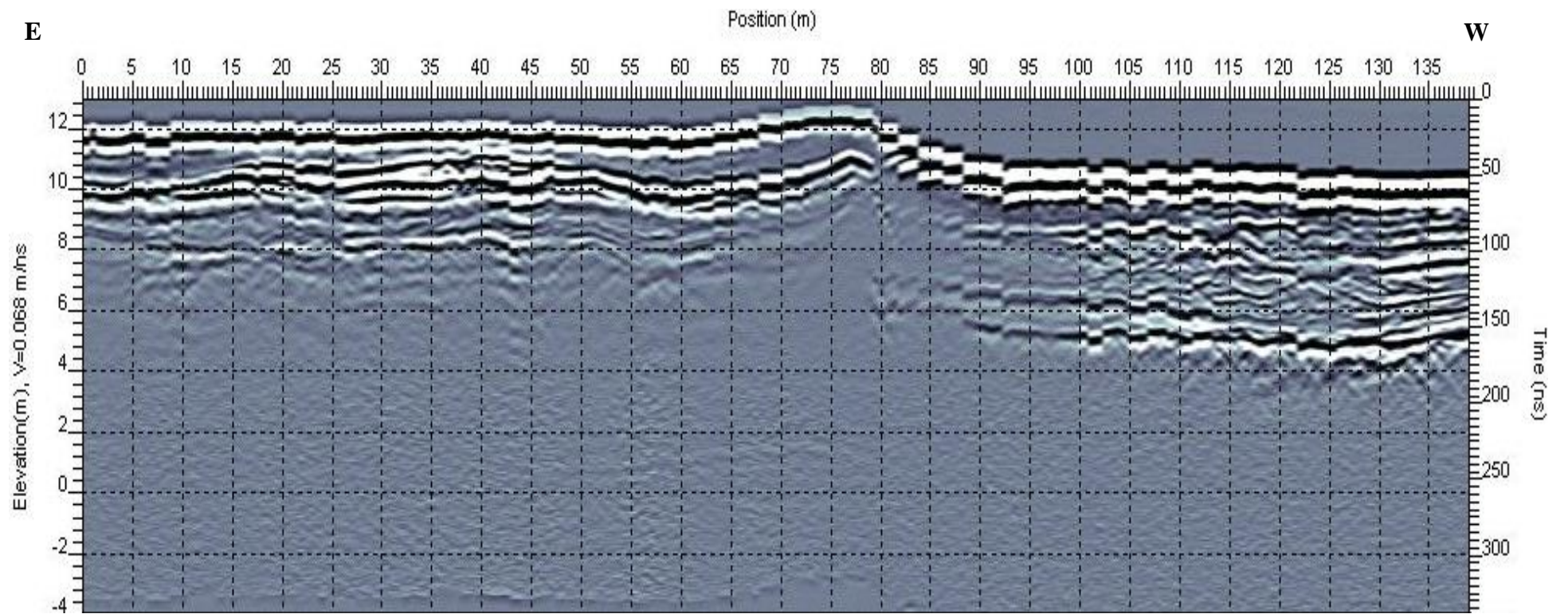


Fig. 3.14a GPR Line 02 Profile with topography corrected. Exported from EkkoView

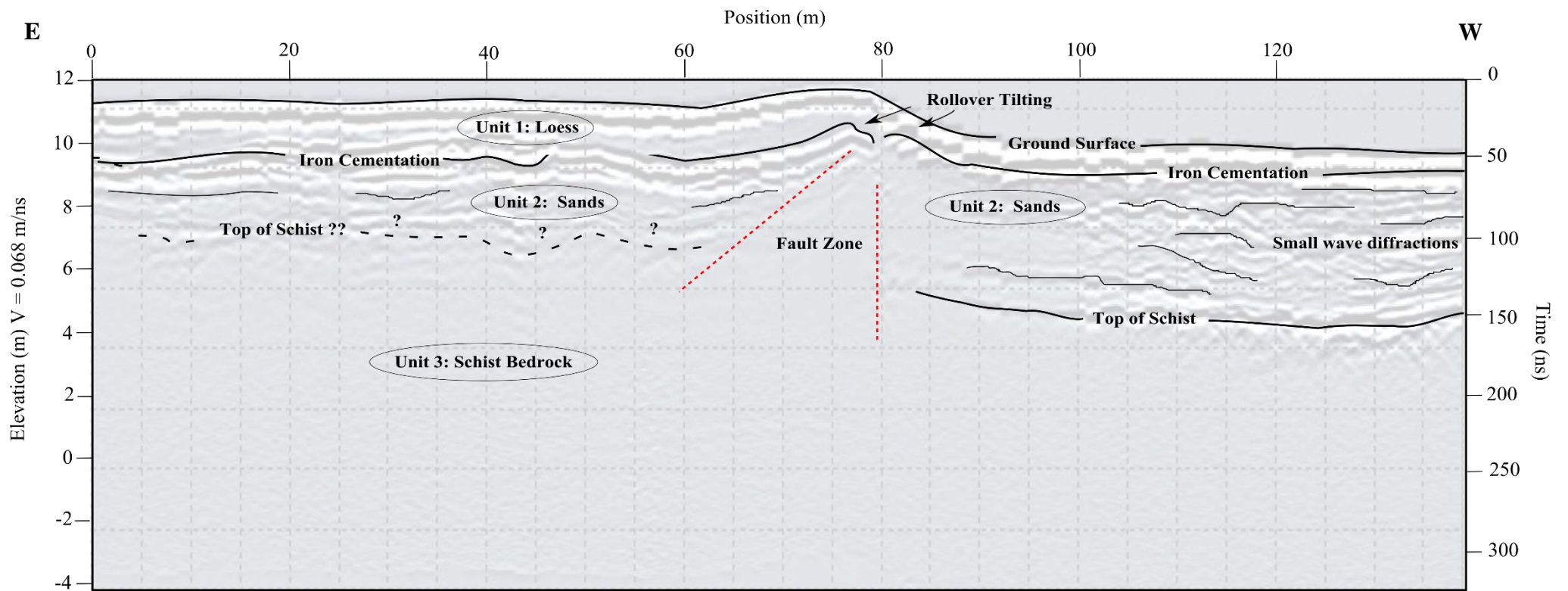


Fig. 3.14b Annotated diagram of GPR line 02 profile (Fig. 3.14a), showing key features.

3.4 SUMMARY

- The site south of Taieri Mouth is of significance as here the Akatore Fault has displaced the 125 ka marine terrace, and this is the last expression of the fault before it heads offshore.
- Observations of historic beach sands show 1 - 2 m of throw across the fault. This is similar to the height of the Akatore Fault scarp. This is a minimum, as erosion and weathering may have played a part in reducing the displacement recorded by the hanging wall.
- The magnetic intensity data clearly show some expression of the fault, and suggest a secondary fault scarp.
- It can be speculated from the GPR results, that there may have been ~4 m of dip slip on the fault since ~125 ka.
- Our observations, combined with findings from previous work, suggests there may have only been the 3 Holocene earthquakes since ~125 ka, and there has been very little activity along the Akatore Fault between ~125 and 10 ka.

Chapter 4

SEISMIC HAZARD IMPLICATIONS



Damaged chimney on house in Bayview Road, Saint Kilda, caused from the 1974 Dunedin Earthquake. Source: Bishop (1974a)

4.1 INTRODUCTORY REMARKS

Recent moderate - large earthquakes in the South Island of New Zealand include the 2010 Darfield Earthquake (M_w 7.1) and the 2016 Kaikoura Earthquake (M_w 7.8; Hamling et al., 2017; Xuhua et al., 2017). These events have highlighted the importance of investigating the locations and characteristics of active faults and their obvious seismic hazard, especially when they are in close proximity to cities. The 2011, Christchurch Earthquake resulted in 183 fatalities over 7,000 injuries, caused \$40 billion of damage and left tens of thousands of people without homes (Orchiston et al., 2016).

The Akatore Fault is in close vicinity to Dunedin City. To the north it is last observed onshore at Taieri Mouth, ~30 km from Dunedin, but its offshore northern continuation may extend close to Kaikorai Valley, only ~ 10 km from the city centre. It is potentially the single greatest source of seismic hazard for Dunedin (Glasse et al., 2003).

In April 1974 an earthquake struck Dunedin with the magnitude (M) 5 and a felt intensity of MM VII. It was located only 10 km south of Dunedin City and caused ~ \$250,000 worth of damage. This earthquake is thought to have been the result of movement on the Akatore Fault or one of related parallel offshore faults (Adams and Kean, 1974; Bishop, 1974a). The worst damage occurred in South Dunedin where the unconsolidated ground amplified the effects (Adams and Kean, 1974; Bishop, 1974a). Since this event smaller earthquakes have been recorded by a seismograph located at the University of Otago. An M 4 earthquake occurred offshore near Taieri Mouth in 1989 (Norris et al., 1994).

In this chapter I have used the data we have collected at Big Creek, Rocky Valley and Taieri Mouth along with earthquake scaling relationships to gain estimates of single event displacement, slip rates, recurrence intervals and magnitude of an event along the Akatore Fault. I then compare our results to those of other faults in the Otago region.

4.2 SUMMARY OF HOLOCENE EVENTS

Trenching of the Akatore Fault at Big Creek and Rocky Valley, has allowed me to conclude that there were three fault rupture events in the Holocene. Evidence of the antepenultimate event comes from the displacement of the schist basement and the damming of sediments, resulting in peat deposition. This event is constrained between $10,400 \pm 1,700$ and $1,326 \pm 22$ cal. yr BP. The evidence for the penultimate event is from the formation of a colluvial wedge. This wedge is in fault contact with the schist suggesting a third (most recent) event. These two events have been constrained between $1,326 \pm 22$ and 776 ± 22 cal. yr BP.

Observations at Taieri Mouth, and previous dating of the marine terraces (Litchfield and Lian, 2004), suggests that there has been no, or very little activity along the Akatore Fault between ~ 125 and 10 ka). These results indicate there may have been only three Holocene events since the formation of the ~ 125 ka marine terrace.

4.3 RUPTURE CHARACTERISTICS

The single event displacement (mm), slip rate (mm/yr) and dimensions (W/D) of the fault are crucial in determining the rupture characteristics (recurrence interval and magnitude). These parameters can be determined from paleoseismic studies, and where no data is present, can be inferred from the fault expression. Equations come from Stirling et al. (2012).

4.3.1 Single event displacement

The single event displacement is the amount of dip slip displacement per rupture event. At Big Creek ~5 m of total displacement has been determined from offset of the strath on the schist on the hanging wall and footwall, along the fault plane (41° dip angle). This is slightly greater than the total offset we estimated from the GPR at Taieri Mouth of ~4 m (assuming the deepest reflections correspond to the schist bedrock). Taieri Mouth is the northern most onshore portion of the Akatore Fault, whereas Big Creek is located in the centre of the onshore portion, commonly the dip-slip of a fault tapers towards the end (Scholz, 2002). From trench data at Big Creek and Rocky Valley three rupture events have been determined; giving a single event displacement of 1 – 2 m.

4.3.2 Slip rate

The slip rate defines the long-term average movement along the fault each year, averaged over multiple earthquake cycles. The recent slip rate of the Akatore Fault can be determined from the paleoseismic data collected from the Big Creek and Rocky Valley trenches. The three Holocene events all occurred post 10,400 ± 1,700 cal. yr BP, after the deposition of the silt (unit 5a; Fig. 2.16; 2.17). If the total Holocene displacement is 5 m and the dip slip has a 41° dip angle, we calculate a slip rate of 0.5 mm / yr (Eq. 4.1).

$$\frac{5,000}{10,400} = 0.48 = 0.5 \text{ mm/yr} \quad (4.1)$$

The silt (unit 5a; Fig. 2.16; 2.17) has been interpreted as deposited before the first Holocene event, therefore this value is a minimum. The first Holocene event was interpreted from the presence of peat (unit 4a; Fig. 2.16; 2.17.) in the footwall. Using the age of the peat, 1,326 ± 22 cal. yr BP we determine a maximum slip rate of 3.9 mm / yr (Eq. 4.2).

$$\frac{5,000}{1,326} = 3.877 = 3.9 \text{ mm/yr} \quad (4.2)$$

Hence, the Holocene slip rate is between 3.9 and 0.5 mm / yr.

In the absence of paleoseismic data, the long-term slip rate can be inferred from the geomorphic expression of the fault (Stirling et al., 2012). Here, we have determined the long-term slip rate by measuring the offset of the Otago peneplain near the Akatore Fault. The Otago peneplain is a low relief surface which is well preserved on schist terrain. It is of low topography and is often buried beneath Tertiary sediments (Stirling, 1991). The peneplain is thought to be the result of two erosional periods, one in the late Cretaceous, and the other in the early Cenozoic. In East Otago the Titri and Akatore Faults have displaced the peneplain surface (Bishop and Turnbull, 1996). By measuring the offset of the Otago peneplain near the Akatore Fault we have determined the long term slip rate. The largest offset of the peneplain is near Big Creek. The hill to the immediate south of the Big Creek trench site is ~ 122 m above the valley floor.

Assuming a fault dip of 41°, there has been 186 m of uplift across the fault plane (Eq. 4.3).

$$\frac{122 \text{ m}}{\sin(41)} = 186 \text{ m} \quad (4.3)$$

To calculate the long-term slip rate, the age of initiation of reverse motion on the Akatore Fault must be determined, which requires an understanding of when the ~120 m of peneplain uplift began on the hanging wall of the Akatore Fault

Landis et al. (2008) suggested East Otago was completely inundated in the Oligocene. In East Otago ocean marine regression began ~21 Ma, which has been linked to the beginning of uplift in the area. Oblique convergence and incipient uplift occurred in New Zealand in the early Miocene, 22 – 5 Ma, as a result of the collision of the Pacific and Australian plates. Thickening crust resulted in the formation of mountains (Landis et al., 2008). The Otago Schist has developed strong planar schistosity associated with regional metamorphism. In the Taieri River catchment, incipient uplift of the surrounding schist

ridges have been aged at middle Quaternary, ~ 1 Ma, from cosmogenic dating of sedimentary quartzites (Bennett et al., 2006; Bennett et al., 2005; Waters et al., 2015).

The Titri Fault is a Mesozoic fault which was reactivated in the late Miocene (Mutch and Wilson, 1952; Bishop and Turnbull, 1996; Litchfield, 2001). Stream catchments have developed on the Titri Fault block and flow south-east down the dip slope. These include streams such as Akatore Creek, Big Creek, Bull Creek and Nobles Stream, which have cut through the Akatore Fault block, forming antecedent gorges. Evidence comes from remnants of the late Cretaceous sedimentary cover on the footwall of the Akatore Fault (Fig. 4.1). Drainage patterns indicate that the initiation of reverse motion on the Akatore Fault is much younger than the parallel Titri Fault (Norris et al., 1994).

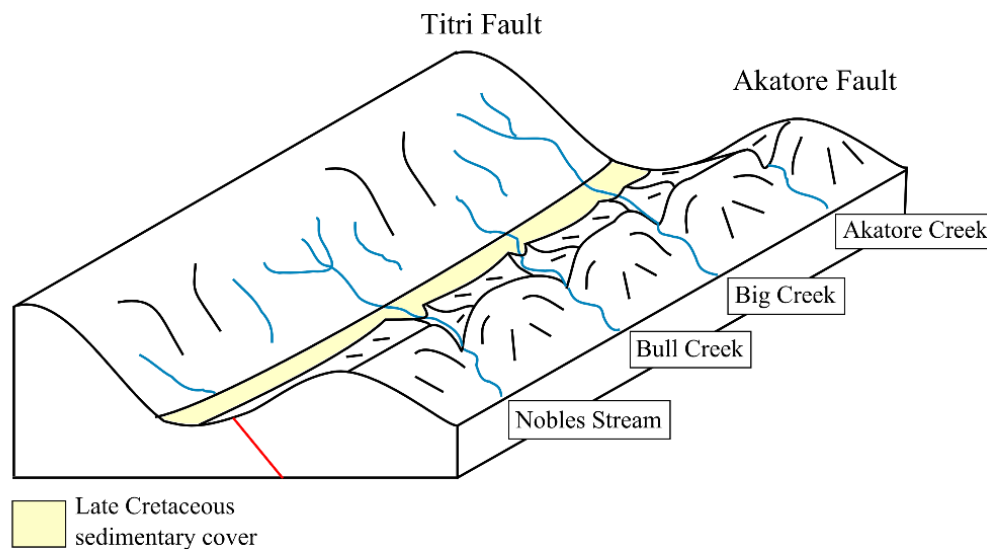


Fig. 4.1 Schematic diagram of the drainage patterns along the Akatore Fault (fault plane illustrated in red).

The reverse displacement on the Akatore Fault postdates the eruption of the Dunedin Volcanic Group which indicates motion along the fault occurred post 5 Ma (Bishop and Turnbull, 1996; Litchfield and Norris, 2000; Norris et al., 1994). Furthermore, the Akatore Fault scarp is well preserved with a youthful appearance (apparent from limited river incision and drainage development) suggesting it is Quaternary in age (Litchfield, 2001; Litchfield and Norris, 2000; Norris et al., 1994).

In consideration of all the above, we have used 1 Ma as the initiation of uplift on the hanging wall block of the Akatore Fault. If the uplift began 1 Ma this would result in a slip rate of 0.2 mm / yr (Eq. 4.4).

$$\frac{186,000}{1,000,000} = 0.186 = 0.2 \text{ mm/yr} \quad (4.4)$$

For comparison, I have also calculated the slip rate for a 5 Ma inception age of uplift on the peneplain. This is a maximum age for the peneplain uplift. If the uplift began at 5 Ma this would result in a slip rate of 0.04 mm per year (Eq. 4.5).

$$\frac{186,000}{5,000,000} = 0.0372 = 0.04 \text{ mm/yr} \quad (4.5)$$

Comparing the short-term and long-term slip rates (Equations 4.1 - 4.5) can provide information on the behaviour of the fault through time. The short term (Holocene) slip rate, 3.9 – 0.5 mm / yr, is significantly higher than the long-term slip rate of 0.04 – 0.2 mm/yr. This suggests that motion along the fault is not periodic and that the Akatore Fault has been experiencing a period of ‘higher than expected’ activity in geologically recent time. This line of reasoning, of course, is dependent on our assumed age estimates for the initiation of peneplain uplift at the Akatore Fault.

Our results suggest there have only been three Holocene events in the last ~125 ka. This indicates that the Akatore Fault has gone through a period of activity post 10,400 yr ± 1,700 cal. yr BP; prior to this the Akatore Fault was in a period of quiescence. If there have only been the three Holocene earthquakes since ~125 ka, we can use this age along with the long-term slip rate, 0.2 and 0.04 mm/year, to gain an expected total displacement over that 125 ka time period. This is highly speculative, as we remain unsure as to whether evidence of pre-Holocene earthquakes is missing at Taieri Mouth due to modification of the 125 ka marine terrace.

Using the 1 Ma slip rate gives us an expected total post-125 ka displacement of 24 m which is significantly greater than the 5 m of total displacement measured in the trenches

(Eq. 4.6). This provides a slip deficit of 19 m; in this scenario, where all of the uplift occurred in the last 1 Ma, the Akatore Fault has not presently slipped enough to accommodate the longer-term strain accumulation.

$$0.19 \times 125,000 = 23,750 \text{ mm} = 24 \text{ m} \quad (4.6)$$

However, if we use the 5 Ma slip rate we gain an expected total post 125 ka displacement of 4.6 m (Eq. 4.7). This is similar / slightly less than the total displacement measured in the trenches, so would suggest that the Holocene slip has been enough to accommodate the long term strain accumulation; there is no post 125 ka slip deficit in this scenario.

$$0.037 \times 125,000 = 4,625 \text{ mm} = 4.6 \text{ m} \quad (4.7)$$

As discussed previously, relevant literature suggests it is more probable that the inception of peneplain uplift occurred in the Quaternary, therefore the 0.2 mm/yr slip rate is more likely. This would imply that the Akatore Fault may not have accommodated the total strain accumulated at that rate, and therefore possibly still be in a state of ‘activity’. Even if the peneplain inception began at 4 Ma this may result in some slip deficit on the fault. Overall the fault may pose a higher seismic hazard for Dunedin and the surrounding areas if a younger age of peneplain uplift is considered and if there has only been three Holocene events since ~125 ka.

4.3.3 Recurrence interval

The recurrence interval is the average recurrence, in years, of ground motion along a fault assuming the fault behaves in a periodic fashion. The recurrence interval (T) can be calculated from the single event displacement (D) and the slip rate (SR ; Eq. 4.8).

$$\frac{D}{SR} = T \quad (4.8)$$

From our paleoseismic data, we obtained a single event displacement of 1 - 2 m. Here we have used a single event displacement of 1.5 m and the previously calculated slip rates to obtain a recurrence interval.

To calculate the short term (Holocene) recurrence interval we use the minimum slip rate of 0.48 mm/yr and the maximum slip rate of 3.8 mm/yr. Hence, our Holocene recurrence interval is 395 – 3,125 years (Eq. 4.9).

$$\frac{1,500}{0.48} = 3,125 \text{ yrs (min)}, \quad \frac{1,500}{3.8} = 395 \text{ yrs (max)} \quad (4.9)$$

Our short term recurrence interval is similar to that of the National Seismic Hazard Model for New Zealand; the Akatore Fault has been modelled to have a recurrence interval of 3,480 years (Stirling et al., 2012).

The long-term recurrence interval can be calculated from the slip rate 0.2 mm/yr, assuming peneplain uplift began around 1 Ma. This provides us with a long term recurrence interval of 7,900 years (Eq. 10).

$$\frac{1,500}{0.19} = 7,900 \text{ yrs} \quad (4.10)$$

This is similar to the 6,000 – 12,000 year recurrence interval calculated by Norris et al. (1994). The long-term recurrence interval provides an average recurrence of a ground rupture since the initiation of reverse motion along the Akatore Fault. Since movements on the Akatore Fault are irregular and episodic, with short periods of activity followed by long periods of quiescence, the recurrence interval does not provide useful information in predicting future events. Given the considerable aperiodicity in the Akatore paleoseismic data, and resulting calculations (above), the fault should be modelled by way of time-dependent methods.

4.3.4 Magnitude

Moment magnitude (M_w) is a measure of energy released and correlates approximately to fault's length or area. The moment magnitude for New Zealand faults is calculated using the following regression in equation (4.11), where W , is the fault width and L , is the fault length (Stirling et al., 2012).

$$4.18 + \frac{2}{3} \log W + \frac{4}{3} \log L = M_w \quad (4.11)$$

For the Akatore Fault we use a width of 18.3 km which has been calculated using 12 km as the base depth of the seismogenic zone and dip of 41° (dip is from the penultimate event at Big Creek; Eq. 4.12). In most of the central South Island the depth of the seismogenic base is 12 ± 2 km (Leitner et al., 2001).

$$\frac{12 \text{ km}}{\sin(41)} = 18.3 \text{ km} \quad (4.12)$$

The onshore extent of the Akatore Fault is well constrained at ~ 22 km in length, however the extent of the offshore portion is still in debate. If the fault extends from off the coast of Kaitangata, to the south and to Kaikorai Estuary in the north, the total will be a maximum rupture length of ~ 62 km (Bishop and Turnbull, 1996); we will calculate two magnitudes based on the maximum and minimum fault lengths.

Using a fault length of 22 km results in an earthquake with a moment magnitude of 6.8 (Eq. 4.13). This is the minimum M_w expected along the Akatore Fault. The relevant calculation is as follows:

$$4.18 + \frac{2}{3} \log (18.3) + \frac{4}{3} \log (22) = 6.81 \quad (4.13)$$

Assuming the fault extends to a total length of 62 km, results in an earthquake with a moment magnitude of 7.4 (Eq. 4.14). This is the maximum M_w expected along the Akatore Fault.

$$4.18 + \frac{2}{3} \log (18.3) + \frac{4}{3} \log (62) = 7.41 \quad (14) \quad (4.14)$$

Utilising the New Zealand regression equation, an earthquake on the Akatore Fault is likely to result in an M_w of 6.8 – 7.4. This gives us an average earthquake M_w of 7.1.

4.3.5 Modified Mercalli Intensity (MMI)

From these moment magnitudes, the intensity of an earthquake near Dunedin can be estimated. Intensity is a measurement of damage to manmade structures, humans and nature caused by strong motion from an earthquake (Alvarez et al., 2012). The Modified Mercalli Intensity (MMI) in Dunedin can be estimated from Equation (4.15), which is has been modelled from felt earthquake reports in California. In this equation, Δ is the distance between the site and the epicentre (Bakun and Wentworth, 1997).

$$1.68 M_w - 3.29 - 0.0206 \Delta = MMI \quad (4.15)$$

Here we have calculated a range of MMI values for Dunedin CBD, based on different epicentral locations along the fault, Kaikorai Valley (Eq. 4.16), Taieri Mouth (Eq. 4.17), Big Creek (Eq. 4.18) and Tokomairiro Mouth (Eq. 4.19). We will assume the earthquake has average M_w of 7.1.

$$1.68 (7.1) - 3.29 - 0.0206 (10) = 8.4 \quad (4.16)$$

$$1.68 (7.1) - 3.29 - 0.0206 (30) = 8.0 \quad (4.17)$$

$$1.68 (7.1) - 3.29 - 0.0206 (40) = 7.8 \quad (4.18)$$

$$1.68 (7.1) - 3.29 - 0.0206 (50) = 7.6 \quad (4.19)$$

These provide us with MMI values between 7.6 and 8.4, which relate to considerable damage of infrastructure (Table. 4.1).

These are average intensities that are typically experienced, however the intensities may vary depending on earthquake parameters and the underlying geology. Sites which are underlain by hard rock typically experience lower intensities than sites underlain by soft, unconsolidated sediments (Bakun and Wentworth, 1997). Dunedin has many high risk areas, such as those underlain by poorly consolidated, fine grained sediments and water saturated areas (e.g. Taieri Plains and coastal areas) which are prone to greater shaking and liquefaction than sites with firmer geology. Also, landslides would be likely to occur on moderate to steep slopes, notably where Tertiary marine sediments overlie bedrock (e.g. Green Island and Saddle Hill; Bakun and Wentworth, 1997; Barrell et al., 2014; Glassey et al., 2003).

Table. 4.1 Modified Mercalli Intensity Scale, VII - IX, for Dunedin (Murashev et al., 2006; Wood and Neumann, 1931). The complete MMI scale can be found in Appendix 4.

VII	Moderate shaking, damage considerable in poorly built houses e.g. fallen chimneys, wall damage, broken windows, and furniture. Damage negligible in well-designed buildings. Small landslides and rock fall in susceptible areas.
VIII	Trees shaken, liquefaction in susceptible areas, considerable damage in most houses. Partial collapse in some cases. Fallen walls, chimneys, columns and monuments. Overturned heavy furniture. Small landslides and rock fall in all areas.
IX	Considerable damage. Liquefaction in susceptible areas. Obvious cracked ground. Great damage in all buildings. Large collapse. Buildings shifted off foundations, underground pipes. Small to moderate landslides and rock fall.

4.4 COMPARISON WITH OTHER OTAGO FAULTS

For the Otago faults Norris et al., (2004) have compiled data on the average fault rupture parameters. The average fault length is 24 km and the single event displacement is 1 -2 m. The average slip rate is 0.2 mm/yr, with a range of 0.1-1 mm /yr, which suggest a recurrence interval of 5,000 – 15,000 years (Berryman and Beanland, 1991; Norris, 2004; Stirling et al., 2002). Our Akatore results fit within these averages for Otago faults. We calculated a recurrence rate of 7,900 years, 1-2 m of single event displacement and a long-term slip rate of 0.2 mm/years, assuming that uplift began 1 Ma. Total vertical displacements of the Otago faults range from 120 to 2,000 m (Youngson et al., 1998). The Akatore Fault is on the lower end of this range, perhaps signifying it is a relatively young fault.

The Akatore Fault may behave episodically, with short periods of activity followed by long periods of quiescence. There may have been no movement between ~125 and 10 ka, which means that the fault may have been in a period of quiescence for at least 100 ka. In Otago, other faults have been suggested as possibly exhibiting similar behaviours, such as Pisa, Dunstan and Titri Faults. These faults may have periods of quiescence similar to the Akatore Fault (Beanland and Berryman, 1989; Norris, 2004).

More information is required to establish if this episodic behaviour is wide-spread in Otago. This behaviour of long periods of quiescence may explain the low rates of historic seismicity. This provides issues for earthquake hazard assessment in Otago.

4.5 SUMMARY

- Three Holocene events have been determined from the trench data. The antepenultimate event occurred between $10,400 \pm 1,700$ and $1,326 \pm 22$ cal. yr BP. The penultimate event and most recent event occurred between $1,326 \pm 22$ and 776 ± 22 cal. yr BP
- There is ~ 5 m of total dip-slip displacement on the fault plane at Big Creek trench, indicating single event displacement of 1 - 2 m per Holocene event.
- We have calculated a Holocene slip rate of 3.8 - 0.5 mm/yr and a long-term slip rate of 0.2 and 0.04 mm/yr assuming the inception of peneplain uplift is 1 and 5 Ma, respectively.
- If the Akatore Fault uplift commenced ~ 1 Ma then there may not have been enough Holocene slip to have accommodated 125 ka of accumulated strain.
- The Akatore Fault has a wide range of recurrence intervals (Holocene: 395 – 3,125 years; long term: 395 - 7,900 years), in addition to the possible longer-term aperiodicity.
- Depending on the total fault length, earthquakes between M_w 6.8 and 7.4 are expected along the Akatore Fault.
- These moment magnitudes would result in estimated MMIs between 7.6 and 8.4 for Dunedin. Depending on the rupture length of the fault, these intensities would cause considerable damage to the city.
- The Akatore Fault has similar parameters to other Otago faults. Episodic fault behaviour may be characteristic of other faults in Otago.

Chapter 5

CONCLUSIONS AND FUTURE WORK



Akatore Fault in the distance, evident from the offset of peneplain surface (the notch in the distant hillslopes).

Photo taken from Flagstaff Hill, Dunedin.

5.1 PALEOSEISMOLOGY

In order to investigate the rupture history of the Akatore Fault in the Holocene we successfully trenched the fault, and radiocarbon and OSL dated unfaulted and faulted sediments. We have determined that there have been three ground rupturing events along the Akatore Fault in the Holocene. The antepenultimate event has been constrained between $10,400 \pm 1,700$ and $1,326 \pm 22$ cal. yr BP, however this is likely to be closer to the later data, while, the second and third (most recent) events have been constrained between $1,326 \pm 22$ and 776 ± 22 cal. yr BP. The offset of gravels within Big Creek trench produced a total displacement of ~ 5 m along the fault plane, therefore, 1-2 m of slip per event.

Observations along exposures of beach sands at Taieri Mouth suggest there has been 1-2 m of throw since the deposition of loess (~ 20 ka). Furthermore I speculate, on the basis of the Taieri Mouth GPR results, that there may have been only 4 m of dip slip on the fault since 125 ka. These results are similar to those of previous work (e.g. Litchfield and Lian, 2004; Litchfield and Norris, 2000; Bishop and Turnbull, 1996; Bishop, 1994), and suggest there have only been three Holocene events since the formation of the marine terrace, and therefore no movement between ~ 10 and 125 Ka.

5.2 SEISMIC HAZARD

My findings suggest that the Akatore Fault has the potential to produce earthquakes of $6.8 - 7.4 M_w$. Assuming uplift of the hanging wall of the Akatore Fault began at 1 Ma, the fault has an estimated long term recurrence interval of 7,900 years. However, the Akatore Fault may have episodic behaviour, which makes it difficult to estimate the

overall recurrence parameters and future hazard implications; other Otago faults may have similar behaviours. The Akatore Fault may not have slipped as much as expected based on the long-term slip rate, which means that further fault ruptures could occur in the near future, geologically-speaking. A large earthquake on the Akatore Fault could cause considerable damage to Dunedin, and in neighbouring areas underlain by soft sediments. The Akatore Fault needs to become the focus of a time-dependent seismic hazard calculation for Dunedin.

5.3 FUTURE WORK

To provide more concise information on the hazard Akatore Fault poses, it is crucial that future work is aimed at better constraining the age of inception of Akatore Fault uplift. This age is vital to determining whether the three Holocene events have accommodated enough long term strain accumulation, or whether there is currently slip deficit across the Akatore Fault. Also, it is important that we determine the total length of the fault to produce improved moment magnitude estimates. Depth data of the seismogenic base near the Akatore Fault, will be updated in the following year (M. Reyners pers.comm.), which will allow for more accurate estimates of magnitude.

Future work could also include coring and/or trenching the Akatore Fault at the site south of Taieri Mouth, in order to verify the GPR profile interpretations of minimal post 125 ka displacement across the fault. Finally, it is essential that further paleoseismic studies are undertaken in Otago to better understand the behaviour of these faults, particularly whether they are episodic like the Akatore Fault.

REFERENCES

- Adams, R. & Kean, R. 1974. The Dunedin Earthquake, 9 April 1974: Part I: Seismological Studies. *Bulletin of the New Zealand National Society for Earthquake Engineering*, 7, 115-122.
- Akinci, A. & Antonioli, A. 2012. Observations and stochastic modelling of strong ground motions for the 2011 October 23 Mw 7.1 Van, Turkey, earthquake. *Geophysical Journal International*, 192, 1217-1239.
- Alvarez, D. A., Hurtado, J. E. & Bedoya-ruíz, D. A. 2012. Prediction of modified Mercalli intensity from PGA, PGV, moment magnitude, and epicentral distance using several nonlinear statistical algorithms. *Journal of Seismology*, 16, 489-511.
- Anderson, E. 1951. The dynamics of faulting *Edinburgh Geological Society*, 8, 387-402
- Anderson, H. & Webb, T. 1994. New Zealand seismicity: patterns revealed by the upgraded National Seismograph Network. *New Zealand Journal of Geology and Geophysics*, 37, 477-493.
- Antolik, M. & Dreger, D. S. 2003. Rupture process of the 26 January 2001 Mw 7.6 Bhuj, India, earthquake from teleseismic broadband data. *Bulletin of the Seismological Society of America*, 93, 1235-1248.
- Aoudia, A., Saraò, A., Bukchin, B. & Suhadolc, P. 2000. The 1976 Friuli (NE Italy) thrust faulting earthquake: a reappraisal 23 years later. *Geophysical Research Letters*, 27, 573-576.
- Arnold, J & Libby, W. F. 1949. Age determinations by radiocarbon content: checks with samples of known age. *Science*, 110, 678-680.
- Bailey, A. 1974. Near surface fault detection by magnetometer. *California Geology*, 38, 274-277.
- Bakun, W. U. & Wentworth, C. 1997. Estimating earthquake location and magnitude from seismic intensity data. *Bulletin of the Seismological Society of America*, 87, 1502-1521.

- Barker, S. L. L. 2005. Pseudotachylyte-generating faults in Central Otago, New Zealand. *Tectonophysics*, 397, 211-223.
- Barrell, D. J. A., Mcintosh, P., Forsyth, P. D., Litchfield, N. J., Eden, D. N., Glassey, P. J., Brown, L. J., Froggatt, P. C., Morrison, B., Smith-Lytle, B., Turnbull, I. M. 1998: Quaternary fans and terraces of coastal Otago, New Zealand. *Institute of Geological & Nuclear Sciences Report*, 98/11.
- Barrell, D. J. A., Glassey, P., Cox, S. & Lytle, B. S. 2014. Assessment of liquefaction hazards in the Dunedin City district.
- Bartsch-Winkler, S. & Schmoll, H. R. 1992. Utility of radiocarbon-dated stratigraphy in determining late Holocene earthquake recurrence intervals, upper Cook Inlet region, Alaska. *Geological Society of America Bulletin*, 104, 684-694.
- Beanland, S. & Barrow-Hurlbert, S. A. 1988. The Nevis-Cardrona fault system, central Otago, New Zealand: late Quaternary tectonics and structural development. *New Zealand journal of geology and geophysics*, 31, 337-352.
- Beanland, S., Berryman, K. R. & Blick, G. H. 1989. Geological investigations of the 1987 Edgecumbe earthquake, New Zealand. *New Zealand journal of geology and geophysics*, 32, 73-91.
- Beanland, S. & Berryman, K. R. 1989. Style and episodicity of late Quaternary activity on the Pisa-Grandview Fault Zone, Central Otago, New Zealand. *New Zealand Journal of Geology and Geophysics*, 32, 451-461.
- Beavan, J. & Haines, J. 2001. Contemporary horizontal velocity and strain rate fields of the Pacific-Australian plate boundary zone through New Zealand. *Journal of Geophysical Research: Solid Earth*, 106, 741-770.
- Ben-Zion, Y. 2008. Collective behavior of earthquakes and faults: Continuum-discrete transitions, progressive evolutionary changes, and different dynamic regimes. *Reviews of Geophysics*, 46.
- Bennett, E., Youngson, J., Jackson, J., Norris, R., Raisbeck, G. & Yiou, F. 2006. Combining geomorphic observations with in situ cosmogenic isotope measurements to study anticline growth and fault propagation in Central Otago, New Zealand. *New Zealand Journal of Geology and Geophysics*, 49, 217-231.
- Bennett, E. R., Youngson, J. H., Jackson, J. A., Norris, R. J., Raisbeck, G. M., Yiou, F. & Fielding, E. 2005. Growth of South Rough Ridge, Central Otago, New Zealand: Using in situ cosmogenic isotopes and geomorphology to study an active, blind reverse fault. *Journal of Geophysical Research: Solid Earth*, 110.
- Benson, W. N. 1935. Some land forms in southern New Zealand. *The Australian Geographer*, 2, 3-22.

- Berberian, M. 1979. Earthquake faulting and bedding thrust associated with the Tabas-e-Golshan (Iran) earthquake of September 16, 1978. *Bulletin of the Seismological Society of America*, 69, 1861-1887.
- Berberian, M., Asudeh, I., Bilham, R., Scholz, C. & Soufleris, C. 1979. Mechanism of the main shock and the aftershock study of the Tabas-e-Golshan (Iran) earthquake of September 16, 1978: A preliminary report. *Bulletin of the Seismological Society of America*, 69, 1851-1859.
- Berryman, K. 1980. Late Quaternary movement on White Creek Fault, South Island, New Zealand. *New Zealand journal of geology and geophysics*, 23, 93-101.
- Berryman, K. & Beanland, S. 1991. Variation in fault behaviour in different tectonic provinces of New Zealand. *Journal of Structural Geology*, 13, 177-189.
- Berryman, K., Cooper, A., Norris, R., Villamor, P., Sutherland, R., Wright, T., Schermer, E., Langridge, R. & Biasi, G. 2012. Late Holocene rupture history of the Alpine fault in south Westland, New Zealand. *Bulletin of the Seismological Society of America*, 102, 620-638.
- Berryman, K. R. 1993. Distribution, age, and deformation of Late Pleistocene marine terraces at Mahia Peninsula, Hikurangi Subduction Margin, New Zealand. *Tectonics*, 12, 1365-1379.
- Bishop, D. 1974a. The Dunedin earthquake, 9 April 1974. Part 2: Local effects. *Bulletin of the New Zealand National Society for Earthquake Engineering*, 7, 123-129.
- Bishop, D. 1974b. Stratigraphic, structural, and metamorphic relationships in the Dansey Pass area, Otago, New Zealand. *New Zealand Journal of Geology and Geophysics*, 17, 301-335.
- Bishop, D. 1994. Geology of the Milton area. *Institute of Geological and Nuclear Sciences Map 9*. Scale 1:500 000. 1 sheet + 32 p. Lower Hutt, New Zealand.
- Bishop, D. & Turnbull, I. 1996. Geology of the Dunedin area. *Institute of Geological & Nuclear Sciences Map 21*. Scale 1: 250 000. Lower Hutt, New Zealand.
- Blick, G. H. 1981. Akatore Fault Survey Report 1979-1980. *New Zealand Geological Survey Earth Deformation Studies Report*.
- Boore, D. M. 1989. The Richter scale: its development and use for determining earthquake source parameters. *Tectonophysics*, 166, 1-14.
- Brill, R. P. 1981. Akatore Site Report. *New Zealand Geological Survey Earth Deformation Studies Report 64*.

- Broecker, W. S. 2014. 5.9 - Radiocarbon A2 - Holland, Heinrich D. *In: TUREKIAN, K. K. (ed.) Treatise on Geochemistry (Second Edition)*. Oxford: Elsevier, 257-271
- Bruce, C. 2010. Near - surface expression of active deformation on the Shallow Otago continental shelf. Unpublished B.Sc (Hons) dissertation, University of Otago.
- Bull, W. B. 2009. *Tectonically Active Landscapes*. West Sussex, UK: Wiley-Blackwell, John Wiley & Sons Ltd.
- Cassidy, J. F., Rogers, G. C. & Hyndman, R. D. 2014. An overview of the 28 October 2012 Mw 7.7 earthquake in Haida Gwaii, Canada: A tsunamigenic thrust event along a predominantly strike-slip margin. *Pure and Applied Geophysics*, 171, 3457-3465.
- Chen, Y. G., Chen, Y. W., Chen, W. S., Zhang, J. F., Zhao, H., Zhou, L. P. & Li, S.H. 2003. Preliminary results of long-term slip rates of 1999 earthquake fault by luminescence and radiocarbon dating. *Quaternary Science Reviews*, 22, 1213-1221.
- Chung, W. Y. & Gao, H. 1995. Source parameters of the Anjar earthquake of July 21, 1956, India, and its seismotectonic implications for the Kutch rift basin. *Tectonophysics*, 242, 281-292.
- Cipar, J. 1980. Teleseismic observations of the 1976 Friuli, Italy earthquake sequence. *Bulletin of the Seismological Society of America*, 70, 963-983.
- Clark, D. 1997. Magnetic petrophysics and magnetic petrology: aids to geological interpretation of magnetic surveys. *AGSO Journal of Australian Geology and Geophysics*, 17, 83-104.
- Copley, A., Karasozen, E., Oveisi, B., Elliott, J. R., Samsonov, S. & Nissen, E. 2015. Seismogenic faulting of the sedimentary sequence and laterally variable material properties in the Zagros Mountains (Iran) revealed by the August 2014 Murmuri (E. Dehloran) earthquake sequence. *Geophysical Journal International*, 203, 1436-1459.
- Cotton, C. A. 1957. Pleistocene shorelines on the compound coast of Otago. *New Zealand Journal of Science and Technology* B38: 750-762.
- Crone, A. J., Machette, M. N. & Bowman, J. R. 1992. Geologic investigations of the 1988 Tennant Creek, Australia, earthquakes; implications for paleoseismicity in stable continental regions. *US Geological Survey Bulletin*. 123A
- Davey, F. J., Henyey, T., Holbrook, W. S., Okaya, D., Stern, T. A., Melhuish, A., Henrys, S., Anderson, H., Eberhart-Phillips, D., Mcevilly, T., Uhrhammer, R., Wu, F., Jiracek, G. R., Wannamaker, P. E., Caldwell, G. & Christensen, N. 1998. Preliminary results from a geophysical study across a modern, continent-

- continent collisional plate boundary — the Southern Alps, New Zealand. *Tectonophysics*, 288, 221-235.
- Demets, C., Gordon, R. G., Argus, D. F. & Stein, S. 1994. Effect of recent revisions to the geomagnetic reversal time scale on estimates of current plate motions. *Geophysical Research Letters*, 21, 2191-2194.
- Denham, D., Alexander, L., Everingham, I., Gregson, P., Mccaffrey, R. & Enever, J. 1987. The 1979 Cadoux earthquake and intraplate stress in Western Australia. *Australian Journal of Earth Sciences*, 34, 507-521.
- Denys, P., Pearson, C., Norris, R. & Denham, M. 2016. A geodetic study of Otago: results of the central Otago deformation network 2004–2014. *New Zealand Journal of Geology and Geophysics*, 59, 147-156.
- Dolan, J. F., Sieh, K., Rockwell, T. K., Guphill, P. & Miller, G. 1997. Active tectonics, paleoseismology, and seismic hazards of the Hollywood fault, northern Los Angeles basin, California. *Geological Society of America Bulletin*, 109, 1595-1616.
- Eden, D. N. & Hammond, A. P. 2003. Dust accumulation in the New Zealand region since the last glacial maximum. *Quaternary Science Reviews*, 22, 2037-2052.
- Ékes, C. & Friele, P. 2003. Sedimentary architecture and post-glacial evolution of Cheekye fan, southwestern British Columbia, Canada. *Geological Society, London, Special Publications*, 211, 87-98.
- Everett, M. E. 2013. *Near-surface applied geophysics*, Cambridge University Press.
- Fagereng, Å. & Cooper, A. F. 2010. Petrology of metabasalts from the Chrystalls Beach accretionary melange-implications for tectonic setting and terrane origin. *New Zealand Journal of Geology and Geophysics*, 53, 57-70.
- Fang, L., Wu, J., Wang, W., Lü, Z., Wang, C., Yang, T. & Cai, Y. 2013. Relocation of the mainshock and aftershock sequences of M 7.0 Sichuan Lushan earthquake. *Chinese Science Bulletin*, 58, 3451-3459.
- Farrier, T. P. 1990. *Akatore Fault Monitoring Pattern*. Unpublished B.Surv dissertation, University of Otago.
- Feng, R. & Mcevilly, T. 1983. Interpretation of seismic reflection profiling data for the structure of the San Andreas fault zone. *Bulletin of the Seismological Society of America*, 73, 1701-1720.
- Fielding, E. J., Lundgren, P. R., Taymaz, T., Yolsal-Çevikbilen, S. & Owen, S. E. 2013. Fault-Slip Source Models for the 2011 M 7.1 Van Earthquake in Turkey from

SAR Interferometry, Pixel Offset Tracking, GPS, and Seismic Waveform Analysis. *Seismological Research Letters*, 84, 579-593.

- Fukuyama, E. 2009. *Fault-zone properties and earthquake rupture dynamics*, Academic Press.
- Gage, M. 1953. The study of Quaternary strand-lines in New Zealand. *Transactions of the Royal Society of New Zealand*, 81, 27-34.
- Glassey, P., Barrell, D., Forsyth, J. & Macleod, R. 2003. The geology of Dunedin, New Zealand, and the management of geological hazards. *Quaternary International*, 103, 23-40.
- Gledhill, K., Ristau, J., Reyners, M., Fry, B. & Holden, C. 2011. The Darfield (Canterbury, New Zealand) Mw 7.1 earthquake of September 2010: A preliminary seismological report. *Seismological Research Letters*, 82, 378-386.
- Glennie, C. L., Carter, W. E., Shrestha, R. L. & Dietrich, W. E. 2013. Geodetic imaging with airborne LiDAR: the Earth's surface revealed. *Reports on Progress in Physics*, 76.
- Gorman, A., Bruce, C., Reid-Lindroos, Z. & Preskett, S. Characterization of an active offshore coast-parallel fault system on the shallow SE continental shelf of New Zealand's South Island. AGU Fall Meeting Abstracts, 2009. 1057.
- Gorman, A., Hill, M., Orpin, A., Koons, P., Norris, R., Landis, C., Allan, T., Johnstone, T., Gray, F. & Wilson, D. 2013. Quaternary shelf structures SE of the South Island, imaged by high-resolution seismic profiling. *New Zealand Journal of Geology and Geophysics*, 56, 68-82.
- Grauch, V., Hudson, M. R. & Minor, S. A. 2001. Aeromagnetic expression of faults that offset basin fill, Albuquerque basin, New Mexico. *Geophysics*, 66, 707-720.
- Griffiths, G. A. & Mcsaveney, M. 1983. Distribution of mean annual precipitation across some steepland regions of New Zealand. *New Zealand journal of science*, 26, 197-209.
- Guéguen, Y. & Palciauskas, V. 1994. *Introduction to the Physics of Rocks*, Princeton University Press.
- Hamling, I. J., Hreinsdóttir, S., Clark, K., Elliott, J., Liang, C., Fielding, E., Litchfield, N., Villamor, P., Wallace, L. & Wright, T. J. 2017. Complex multifault rupture during the 2016 Mw 7.8 Kaikōura earthquake, New Zealand. *Science*, eaam7194.
- Hancox, G. T. 2008. The 1979 Abbotsford Landslide, Dunedin, New Zealand: a retrospective look at its nature and causes. *Landslides*, 5, 177-188.

- Hanks, T. C. 1979. b values and ω - γ seismic source models: Implications for tectonic stress variations along active crustal fault zones and the estimation of high-frequency strong ground motion. *Journal of Geophysical Research: Solid Earth*, 84, 2235-2242.
- Harmon, R. S., Mitterer, R. M., Kriausakul, N., Land, L. S., Schwarcz, H. P., Garrett, P., Larson, G. J., Vacher, H. L. & Rowe, M. 1983. U-series and amino-acid racemization geochronology of Bermuda: implications for eustatic sea-level fluctuation over the past 250,000 years. *Palaeogeography, Palaeoclimatology, Palaeoecology*, 44, 41-70.
- Hartzell, S. & Mendoza, C. 1991. Application of an iterative least-squares waveform inversion of strong-motion and teleseismic records to the 1978 Tabas, Iran, earthquake. *Bulletin of the Seismological Society of America*, 81, 305-331.
- Hatheway, A. W. & Leighton, F. B. 1979. Trenching as an exploratory method. *Reviews in Engineering Geology*, 4, 169-196.
- Hildebrand, J., Wiggins, S., Henkart, P. & Conyers, L. 2002. Comparison of seismic reflection and ground-penetrating radar imaging at the controlled archaeological test site, Champaign, Illinois. *Archaeological Prospection*, 9, 9-21.
- Hjulström, F. 1935. *Studies of the morphological activity of rivers as illustrated by the River Fyrís: Inaugural Dissertation*, Almqvist & Wiksells.
- Hough, S. E., Martin, S., Bilham, R. & Atkinson, G. M. 2002. The 26 January 2001 M 7.6 Bhuj, India, earthquake: Observed and predicted ground motions. *Bulletin of the Seismological Society of America*, 92, 2061-2079.
- Hubert-Ferrari, A., Avşar, U., El Ouahabi, M., Lepoint, G., Martinez, P. & Fagel, N. 2012. Paleoseismic record obtained by coring a sag-pond along the North Anatolian Fault (Turkey). *Annals of Geophysics*, 55, 929-953.
- Húska, D. & Jurík, L. 2008. Country as a space to transport water, chemical substances and energy in the system soil - plant - atmosphere. In: Pollution and water resources. *Columbia university seminar proceedings : scientific and social-institutional aspects of Central Europe and USA areas*. Hungarian Academy of Science, 207-224.
- Jackson, J., Norris, R. & Youngson, J. 1996. The structural evolution of active fault and fold systems in central Otago, New Zealand: evidence revealed by drainage patterns. *Journal of Structural Geology*, 18, 217-234.
- Jackson, J., Ritz, J. F., Siame, L., Raisbeck, G., Yiou, F., Norris, R., Youngson, J. & Bennett, E. 2002. Fault growth and landscape development rates in Otago, New Zealand, using in situ cosmogenic ^{10}Be . *Earth and Planetary Science Letters*, 195, 185-193.

- Johnstone, T. 1990. A seismic reflection investigation of the extent and geometry of recent northeast- trending faults on the Otago shelf. Unpublished M.Sc thesis, University of Otago
- Jol, H. M. & Bristow, C. S. 2003. GPR in sediments: advice on data collection, basic processing and interpretation, a good practice guide. *Geological Society, London, Special Publications*, 211, 9-27.
- Jull, A. J. T. & Burr, G. S. 2015. Radiocarbon Dating. *In: Jack Rink, W. & Thompson, J. W. (eds.) Encyclopedia of Scientific Dating Methods*. Dordrecht: Springer Netherlands.
- Kanamori, H. & Anderson, D. L. 1975. Theoretical basis of some empirical relations in seismology. *Bulletin of the Seismological Society of America*, 65, 1073-1095.
- Keddy, P. A. 2010. *Wetland ecology: principles and conservation*, Cambridge University Press.
- Kikuchi, M., Nakamura, M. & Yoshikawa, K. 2003. Source rupture processes of the 1944 Tonankai earthquake and the 1945 Mikawa earthquake derived from low-gain seismograms. *Earth, Planets and Space*, 55, 159-172.
- Kondo, H. & Owen, L. A. 2013. 5.12 Paleoseismology A2 - Shroder, John F. *Treatise on Geomorphology*. San Diego: Academic Press.
- Koons, P. 1990. Two-sided orogen: Collision and erosion from the sandbox to the Southern Alps, New Zealand. *Geology*, 18, 679-682.
- Landis, C., Campbell, H., Begg, J., Mildenhall, D., Paterson, A. M. & Trewick, S. 2008. The Waipounamu Erosion Surface: questioning the antiquity of the New Zealand land surface and terrestrial fauna and flora. *Geological Magazine*, 145, 173-197.
- Langridge, R., Ries, W., Litchfield, N., Villamor, P., Van Dissen, R., Barrell, D., Rattenbury, M., Heron, D., Haubrock, S. & Townsend, D. 2016. The New Zealand active faults database. *New Zealand Journal of Geology and Geophysics*, 59, 86-96.
- Lay, T., Ye, L., Kanamori, H., Yamazaki, Y., Cheung, K. F., Kwong, K. & Koper, K. D. 2013. The October 28, 2012 Mw 7.8 Haida Gwaii underthrusting earthquake and tsunami: Slip partitioning along the Queen Charlotte Fault transpressional plate boundary. *Earth and Planetary Science Letters*, 375, 57-70.
- Lay, T., Ye, L., Koper, K. D. & Kanamori, H. 2016. Assessment of teleseismically-determined source parameters for the April 25, 2015 MW 7.9 Gorkha, Nepal earthquake and the May 12, 2015 MW 7.2 aftershock. *Tectonophysics*, <http://dx.doi.org/10.1016/j.tecto.2016.05.023>

- Le Dortz, K., Meyer, B., Sébrier, M., Braucher, R., Nazari, H., Benedetti, L., Fattahi, M., Bourlès, D., Foroutan, M. & Siame, L. 2011. Dating inset terraces and offset fans along the Dehshir Fault (Iran) combining cosmogenic and OSL methods. *Geophysical Journal International*, 185, 1147-1174.
- Lee, S. J., Huang, H. H., Shyu, J. B. H., Yeh, T. Y. & Lin, T. C. 2014. Numerical earthquake model of the 31 October 2013 Ruisui, Taiwan, earthquake: Source rupture process and seismic wave propagation. *Journal of Asian Earth Sciences*, 96, 374-385.
- Leitner, B., Eberhart-Phillips, D., Anderson, H. & Nabelek, J. L. 2001. A focused look at the Alpine fault, New Zealand: Seismicity, focal mechanisms, and stress observations. *Journal of Geophysical Research: Solid Earth*, 106, 2193-2220.
- Leon, L. A., Dolan, J. F., Shaw, J. H. & Pratt, T. L. 2009. Evidence for large Holocene earthquakes on the Compton thrust fault, Los Angeles, California. *Journal of Geophysical Research: Solid Earth*, 114.
- Lewis, J. D. 1981. *The Cadoux earthquake, 2 June 1979*, Geological Survey of Western Australia.
- Likkason, O. K. 2014. Exploring and Using the Magnetic Methods. In: Marghany, M. *Advanced Geoscience Remote Sensing*. Rijeka: InTech, 141-174
- Lin, A., Ouchi, T., Chen, A. & Maruyama, T. 2001. Co-seismic displacements, folding and shortening structures along the Chelungpu surface rupture zone occurred during the 1999 Chi-Chi (Taiwan) earthquake. *Tectonophysics*, 330, 225-244.
- Lisle, R. J., Orife, T. O., Arlegui, L., Liesa, C. & Srivastava, D. C. 2006. Favoured states of palaeostress in the Earth's crust: evidence from fault-slip data. *Journal of Structural Geology*, 28, 1051-1066.
- Litchfield, N., Craw, D., Koons, P. O., Edge, B., Perraudin, E. & Peake, B. 2002. Geology and geochemistry of groundwater within the Taieri Basin, east Otago, New Zealand. *New Zealand Journal of Geology and Geophysics*, 45, 481-497.
- Litchfield, N. J. 2001. The Titri Fault System: Quaternary-active faults near the leading edge of the Otago reverse fault province. *New Zealand Journal of Geology and Geophysics*, 44, 517-534.
- Litchfield, N. J. & Lian, O. B. 2004. Luminescence age estimates of Pleistocene marine terrace and alluvial fan sediments associated with tectonic activity along coastal Otago, New Zealand. *New Zealand Journal of Geology and Geophysics*, 47, 29-37.

- Litchfield, N. J. & Norris, R. J. 2000. Holocene motion on the Akatore Fault, south Otago coast, New Zealand. *New Zealand Journal of Geology and Geophysics*, 43, 405-418.
- Liu, C., Zheng, Y., Ge, C., Xiong, X. & Hsu, H. 2013. Rupture process of the M 7.0 Lushan earthquake, 2013. *Science China Earth Sciences*, 56, 1187-1192.
- Lohman, R. & Barnhart, W. 2010. Evaluation of earthquake triggering during the 2005–2008 earthquake sequence on Qeshm Island, Iran. *Journal of Geophysical Research: Solid Earth*, 115.
- M.Ongley 1939. The Geology of the Kaitangata-Green Island Subdivision, Eastern and Central Otago Divisions. *New Zealand Geological Survey Branch Bulletin*, 38, 499-511.
- Ma, K. F., Mori, J., Lee, S. J. & Yu, S. 2001. Spatial and temporal distribution of slip for the 1999 Chi-Chi, Taiwan, earthquake. *Bulletin of the Seismological Society of America*, 91, 1069-1087.
- Mackenzie, D. & Craw, D. 2005. Structural and lithological continuity and discontinuity in the Otago Schist, Central Otago, New Zealand. *New Zealand Journal of Geology and Geophysics*, 48, 279-293.
- Mandal, P., Rastogi, B. K., Satyanaraya, H. V. S., Kousalya, M., Vijayraghavan, R., Satyamurty, C., Raju, I. P., Sarma, A. N. S. & Kumar, N. 2004. Characterization of the causative fault system for the 2001 Bhuj earthquake of Mw 7.7. *Tectonophysics*, 378, 105-121.
- Mariita, N. O. 2007. The Magnetic Method. *Short Course II on Surface Exploration for Geothermal Resources*.
- Markley, M. & Norris, R. J. 1999. Structure and neotectonics of the Blackstone Hill Antiform, Central Otago, New Zealand. *New Zealand Journal of Geology and Geophysics*, 42, 205-218.
- Martini, I. P., Cortizas, A. M. & Chesworth, W. 2007. *Peatlands: evolution and records of environmental and climate changes*, Elsevier.
- Matsuda, T., Yamazaki, H., Nakata, T. & Imaizumi, T. 1980. The surface faults associated with the Rikuu earthquake of 1896. *Buletin of Earthquake Research Institute., University of Tokyo*, 55, 795-855.
- Mccalpin, J. P. 2009. *Paleoseismology*, Academic press.
- Mccalpin, J. P. 2013. 14.12 Trenching and Exposed Faces A2 - Shroder, John F. *Treatise on Geomorphology*. San Diego: Academic Press, 138-149.

- Mcfadgen, B. 2008. *Hostile shores: catastrophic events in prehistoric New Zealand and their impact on Maori coastal communities*, Auckland University Press.
- Mcglone, M. S. & Wilmshurst, J. M. 1999. A Holocene record of climate, vegetation change and peat bog development, east Otago, South Island, New Zealand. *Journal of Quaternary science*, 14, 239-254.
- Mckellar, I. 1966. Sheet 25 Dunedin Geological map of New Zealand 1: 250000. Department of Scientific and Industrial Research, Wellington.
- Meghraoui, M., Maouche, S., Chemaa, B., Cakir, Z., Aoudia, A., Harbi, A., Alasset, P. J., Ayadi, A., Bouhadad, Y. & Benhamouda, F. 2004. Coastal uplift and thrust faulting associated with the Mw= 6.8 Zemmouri (Algeria) earthquake of 21 May, 2003. *Geophysical Research Letters*, 31.
- Mitchell, W. A. 1977. Partial recovery and reconstruction after disaster: the Lice case. *Mass Emergencies*, 2, 233-247.
- Moazami-Goudarzi, K. & Akasheh, B. 1977. The earthquake of September 6, 1975 in Lice (eastern Turkey). *Tectonophysics*, 40, 361-368.
- Molnar, P., Anderson, R. S. & Anderson, S. P. 2007. Tectonics, fracturing of rock, and erosion. *Journal of Geophysical Research: Earth Surface*, 112, F03014.
- Motagh, M., Bahroudi, A., Haghghi, M. H., Samsonov, S., Fielding, E. & Wetzell, H. U. 2015. The 18 August 2014 Mw 6.2 Mormori, Iran, Earthquake: A Thin-Skinned Faulting in the Zagros Mountain Inferred from InSAR Measurements. *Seismological Research Letters*, 86, 775-782.
- Murashev, A., Stewart, D. & Lynch, R. 2006. Seismic Risk in the Otago Region. Earthquakes and Urban Development: New Zealand Geotechnical Society 2006 Symposium, Nelson, February 2006. Institution of Professional Engineers New Zealand.
- Murray, A. S. & Olley, J. M. 2002. Precision and accuracy in the optically stimulated luminescence dating of sedimentary quartz: a status review. *Geochronometria*, 21, 1-16.
- Murray, C. J., Last, G. V. & Truex, M. J. 2005. Review of Geophysical Techniques to Define the Spatial Distribution of Subsurface Properties or Contaminants. Pacific Northwest National Laboratory (PNNL), Richland, WA (US).
- Mutch, A. & Wilson, D. 1952. Reversal of movement on the Titri Fault. *New Zealand Journal of Science and Technology*, 33, 398-403.

- Nakamura, T., Tsuboi, S., Kaneda, Y. & Yamanaka, Y. 2010. Rupture process of the 2008 Wenchuan, China earthquake inferred from teleseismic waveform inversion and forward modeling of broadband seismic waves. *Tectonophysics*, 491, 72-84.
- Nelson, K. D. 1982. A suggestion for the origin of mesoscopic fabric in accretionary melange, based on features observed in the Chrystalls Beach Complex, South Island, New Zealand. *Geological Society of America Bulletin*, 93, 625-634.
- Nissen, E., Ghorashi, M., Jackson, J., Parsons, B. & Talebian, M. 2007. The 2005 Qeshm Island earthquake (Iran)—a link between buried reverse faulting and surface folding in the Zagros Simply Folded Belt? *Geophysical Journal International*, 171, 326-338.
- Nissen, E., Yamini-Fard, F., Tatar, M., Gholamzadeh, A., Bergman, E., Elliott, J. R., Jackson, J. A. & Parsons, B. 2010. The vertical separation of mainshock rupture and microseismicity at Qeshm island in the Zagros fold-and-thrust belt, Iran. *Earth and Planetary Science Letters*, 296, 181-194.
- Norris, R. J. 2004. Strain localisation within ductile shear zones beneath active faults: The Alpine Fault contrasted with the adjacent Otago fault system, New Zealand. *Earth, planets and space*, 56, 1095-1101.
- Norris, R. J. & Cooper, A. F. 2001. Late Quaternary slip rates and slip partitioning on the Alpine Fault, New Zealand. *Journal of Structural Geology*, 23, 507-520.
- Norris, R. J., Koons, P. O. & Cooper, A. F. 1990. Australasian tectonics The obliquely-convergent plate boundary in the South Island of New Zealand: implications for ancient collision zones. *Journal of Structural Geology*, 12, 715-725.
- Norris, R. J., Koons, P. O. & Landis, C. A. 1994. *Seismotectonic evaluation of fault structures in east Otago*, Department of Geology, University of Otago.
- Oglesby, D. D., Archuleta, R. J. & Nielsen, S. B. 1998. Earthquakes on dipping faults: the effects of broken symmetry. *Science*, 280, 1055-1059.
- Oglesby, D. D., Archuleta, R. J. & Nielsen, S. B. 2000. The three-dimensional dynamics of dipping faults. *Bulletin of the Seismological Society of America*, 90, 616-628.
- Orchiston, C., Davies, T., Langridge, R., Wilson, T., Mitchell, J. & Hughes, M. 2016. Alpine Fault Magnitude 8 Hazard Scenario.
- Parsons, T., Yeats, R. S., Yagi, Y. & Hussain, A. 2006. Static stress change from the 8 October, 2005 M= 7.6 Kashmir earthquake. *Geophysical Research Letters*, 33.

- Pathier, E., Fielding, E., Wright, T., Walker, R., Parsons, B. & Hensley, S. 2006. Displacement field and slip distribution of the 2005 Kashmir earthquake from SAR imagery. *Geophysical Research Letters*, 33.
- Pillans, B. 1990. Pleistocene marine terraces in New Zealand: a review. *New Zealand journal of geology and geophysics*, 33, 219-231.
- Pitcairn, I. K., Craw, D. & Teagle, D. A. 2015. Metabasalts as sources of metals in orogenic gold deposits. *Mineralium Deposita*, 50, 373-390.
- Quigley, M., Van Dissen, R., Litchfield, N., Villamor, P., Duffy, B., Barrell, D., Furlong, K., Stahl, T., Bilderback, E. & Noble, D. 2012. Surface rupture during the 2010 Mw 7.1 Darfield (Canterbury) earthquake: Implications for fault rupture dynamics and seismic-hazard analysis. *Geology*, 40, 55-58.
- Rashed, M., Kawamura, D., Nemoto, H., Miyata, T. & Nakagawa, K. 2003. Ground penetrating radar investigations across the Uemachi fault, Osaka, Japan. *Journal of Applied Geophysics*, 53, 63-75.
- Rees-Jones, J., Rink, W. J., Norris, R. J. & Litchfield, N. J. 2000. Optical luminescence dating of uplifted marine terraces along the Akatore Fault near Dunedin, South Island, New Zealand. *New Zealand Journal of Geology and Geophysics*, 43, 419-424.
- Rhodes, E. J. 2011. Optically stimulated luminescence dating of sediments over the past 200,000 years. *Annual Review of Earth and Planetary Sciences*, 39, 461-488.
- Richter, C. F. 1935. An instrumental earthquake magnitude scale. *Bulletin of the Seismological Society of America*, 25, 1-32.
- Robertson, P. 1958. Structural and metamorphic geology of the Brighton- Taieri Mouth area East Otago, New Zealand. Unpublished M.Sc thesis, University of Otago.
- Scholz, C. 1988. The brittle-plastic transition and the depth of seismic faulting. *Geologische Rundschau*, 77, 319-328.
- Scholz, C. H. 2002. *The mechanics of earthquakes and faulting*, Cambridge University Press.
- Sibson, R. H. & Xie, G. 1998. Dip range for intracontinental reverse fault ruptures: Truth not stranger than friction? *Bulletin of the Seismological Society of America*, 88, 1014-1022.
- Štěpančíková, P., Hók, J., Nývlt, D., Dohnal, J., Sýkorová, I. & Stemberk, J. 2010. Active tectonics research using trenching technique on the south-eastern section of the

- Sudetic Marginal Fault (NE Bohemian Massif, central Europe). *Tectonophysics*, 485, 269-282.
- Stern, T. A. & McBride, J. H. 1998. Deep Seismic Profiling of the Continents, I: General Results and New Methods. Seismic exploration of continental strike-slip zones. *Tectonophysics*, 286, 63-78.
- Stirling, M. 1991. Peneplain modification in an alpine environment of Central Otago, New Zealand. *New Zealand journal of geology and geophysics*, 34, 195-201.
- Stirling, M., Mcverry, G., Gerstenberger, M., Litchfield, N., Van Dissen, R., Berryman, K., Barnes, P., Wallace, L., Villamor, P., Langridge, R., Lamarche, G., Nodder, S., Reyners, M., Bradley, B., Rhoades, D., Smith, W., Nicol, A., Pettinga, J., Clark, K. & Jacobs, K. 2012. National Seismic Hazard Model for New Zealand: 2010 Update. *Bulletin of the Seismological Society of America*, 102, 1514-1542.
- Stirling, M. W., Verry, G. H. M. & Berryman, K. R. 2002. A New Seismic Hazard Model for New Zealand. *Bulletin of the Seismological Society of America*, 92, 1878-1903.
- Trifunac, M. D. & Hudson, D. E. 1971. Analysis of the Pacoima dam accelerogram—San Fernando, California, earthquake of 1971. *Bulletin of the seismological Society of America*, 61, 1393-1411.
- Van Arsdale, R. 2000. Displacement history and slip rate on the Reelfoot fault of the New Madrid seismic zone. *Engineering Geology*, 55, 219-226.
- Vittori, E., Sylos Labini, S. & SERVA, L. 1991. Palaeoseismology: review of the state-of-the-art. *Tectonophysics*, 193, 9-32.
- Walcott, R. 1998. Modes of oblique compression: Late Cenozoic tectonics of the South Island of New Zealand. *Reviews of geophysics*, 36, 1-26.
- Wald, D. J., Heaton, T. H. & Hudnut, K. W. 1996. The slip history of the 1994 Northridge, California, earthquake determined from strong-motion, teleseismic, GPS, and leveling data. *Bulletin of the Seismological Society of America*, 86, S49-S70.
- Wallace, L. M., Beavan, J., Mccaffrey, R., Berryman, K. & Denys, P. 2007. Balancing the plate motion budget in the South Island, New Zealand using GPS, geological and seismological data. *Geophysical Journal International*, 168, 332-352.
- Wang, C., Ding, X., Li, Q., Shan, X., Zhu, W., Guo, B. & liu, P. 2015. Coseismic and postseismic slip models of the 2011 Van earthquake, Turkey, from InSAR, offset-tracking, MAI, and GPS observations. *Journal of Geodynamics*, 91, 39-50.

- Waters, J. M., Wallis, G. P., Burridge, C. P. & Craw, D. 2015. Geology shapes biogeography: Quaternary river-capture explains New Zealand's biologically 'composite' Taieri River. *Quaternary Science Reviews*, 120, 47-56.
- Wells, D. L. & Coppersmith, K. J. 1994. New empirical relationships among magnitude, rupture length, rupture width, rupture area, and surface displacement. *Bulletin of the seismological Society of America*, 84, 974-1002.
- Wen, Y., Xu, C., Liu, Y. & Jiang, G. 2016. Deformation and source parameters of the 2015 Mw 6.5 earthquake in pishan, western China, from Sentinel-1a and ALOS-2 data. *Remote Sensing*, 8, 134.
- Wesnousky, S. G. 2008. Displacement and geometrical characteristics of earthquake surface ruptures: Issues and implications for seismic-hazard analysis and the process of earthquake rupture. *Bulletin of the Seismological Society of America*, 98, 1609-1632.
- Whitcomb, J. H., Allen, C. R., Garmany, J. D. & Hileman, J. A. 1973. San Fernando earthquake series, 1971: focal mechanisms and tectonics. *Reviews of Geophysics*, 11, 693-730.
- Wood, H. O. & Neumann, F. 1931. Modified Mercalli intensity scale of 1931. *Bulletin of Seismological Society of America*, 21, 277-283.
- WOODWARD, C. A. & SLOSS, C. R. 2013. 14.11 Coring and Augering A2 - Shroder, John F. *Treatise on Geomorphology*. San Diego: Academic Press.
- Xie, Z., Jin, B., Zheng, Y., Ge, C., Xiong, X., Xiong, C. & Hsu, H. 2013. Source parameters inversion of the 2013 Lushan earthquake by combining teleseismic waveforms and local seismograms. *Science China Earth Sciences*, 56, 1177-1186.
- Xu, X., Wen, X., Han, Z., Chen, G., LI, C., Zheng, W., Zhnag, S., Ren, Z., Xu, C. & Tan, X. 2013. Lushan M 7.0 earthquake: a blind reserve-fault event. *Chinese Science Bulletin*, 58, 3437-3443.
- Xu, X., Wen, X., Yu, G., Chen, G., Klinger, Y., Hubbard, J. & Shaw, J. 2009. Coseismic reverse-and oblique-slip surface faulting generated by the 2008 Mw 7.9 Wenchuan earthquake, China. *Geology*, 37, 515-518.
- Yeats, R. S., Sieh, K. E., Allen, C. R. & Geist, E. 1997. *The geology of earthquakes*, New York: Oxford university press.
- Yielding, G., Jackson, J., King, G., Sinvhal, H., Vita-Finzi, C. & Wood, R. M. 1981. Relations between surface deformation, fault geometry, seismicity, and rupture characteristics during the El Asnam (Algeria) earthquake of 10 October 1980. *Earth and Planetary Science Letters*, 56, 287-304.

- Youngson, J. 2005. Diagenetic silcrete and formation of silcrete ventifacts and aeolian gold placers in Central Otago, New Zealand. *New Zealand Journal of Geology and Geophysics*, 48, 247-263.
- Youngson, J., Craw, D., Landis, C. & Schmitt, K. 1998. Redefinition and interpretation of late Miocene-Pleistocene terrestrial stratigraphy, central Otago, New Zealand. *New Zealand Journal of Geology and Geophysics*, 41, 51-68.
- Yukihara, E. G. & Mckeever, S. W. 2011. *Optically stimulated luminescence: fundamentals and applications*, John Wiley & Sons.
- Zoback, M., Hickman, S. & Ellsworth, W. 2010. Scientific drilling into the San Andreas fault zone. *Eos*, 91, 197-204.
- Xuhua, S., Yu, W., Jing, L. Z., Ray, W., Shengji, W., Teng, W. & Kerry, S. 2017. How complex is the 2016M w 7.8 Kaikoura earthquake, South Island, New Zealand? *Science Bulletin*, 62, 309-311.

APPENDICES

APPENDIX 1: REFERENCE LIST FOR TABLE. 1.1

The following table contains the reference list for Table. 1.1

1	Wen et al. (2016)
2	Lay et al. (2016)
3	Chung and Gao (1995) & Lee et al. (2014)
4	Copley et al. (2015) & Motagh et al. (2015)
5	Fang et al. (2013), Liu et al. (2013), Xie et al. (2013) & Xu et al. (2013)
6	Cassidy et al. (2014) & Lay et al. (2013)
7	Akinci and Antonioli (2012), Fielding et al. (2013) & Wang et al. (2015)
8	Lohman and Barnhart (2010) & Nissen et al. (2010)
9	Nakamura et al. (2010) & Xu et al. (2009)
10	Lohman and Barnhart (2010), Nissen et al. (2007) & Nissen et al. (2010)
11	Parsons et al. (2006) & Pathier et al. (2006)
12	Meghraoui et al. (2004)
13	Antolik and Dreger (2003)
14	Antolik and Dreger (2003), Hough et al. (2002) & Mandal et al. (2004)
15	Lin et al. (2001) & Ma et al. (2001)
16	Wald et al. (1996)
17	Crone et al. (1992)
18	Yielding et al. (1981)
19	Denham et al. (1987) & Lewis (1981)
20	Berberian (1979), Berberian et al. (1979) & Hartzell and Mendoza (1991)
21	Aoudia et al. (2000) & Cipar (1980)
22	Mitchell (1977), Moazami-Goudarzi and Akasheh (1977) & Wells and Coppersmith, (1994)
23	Trifunac and Hudson (1971), Wesnousky (2008) & Whitcomb et al. (1973)
24	Kikuchi et al. (2003)
25	Kikuchi et al. (2003)
26	Matsuda et al. (1980)

APPENDIX 2: COMPILED TRENCH PHOTOS

Contained here are compiled photos of Big Creek and Rocky Valley trench; pictures were generated in Agisoft Photoscan.

Big Creek Trench



North Wall



South Wall

1 m

Rocky Valley Stream trench



South Wall

1 m

APPENDIX 3: OSL AND RADIOCARBON REPORTS

Optically Stimulated Luminescence and Radiocarbon Reports from which Table 2.1 and 2.2 were compiled.



Rafter Radiocarbon Calibration Report

NZA 61174

R 40891/4

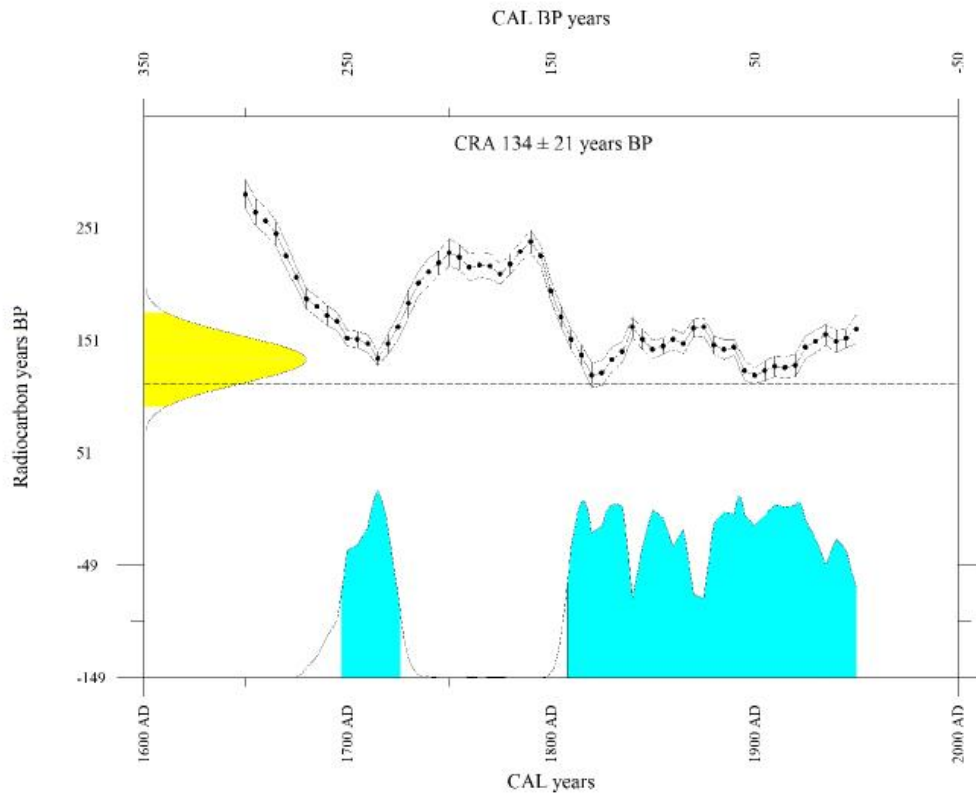
Report issued: 30 May 2016

CONVENTIONAL RADIOCARBON AGE 134 ± 21 years BP

Calibrated with SHCal13 (Hogg et al., Radiocarbon 55(4):1889-1902, 2013).

CALIBRATED AGE in terms of confidence intervals

1 sigma interval is 1707 AD to 1721 AD	243 BP to 229 BP (8.8% of area)
1811 AD to 1838 AD	139 BP to 112 BP (16.8% of area)
1846 AD to 1859 AD	104 BP to 91 BP (7.8% of area)
1863 AD to 1866 AD	87 BP to 84 BP (1.7% of area)
1879 AD to 1931 AD	71 BP to 19 BP (32.7% of area)
1940 AD to 1941 AD	10 BP to 9 BP (0.5% of area)
2 sigma interval is 1697 AD to 1726 AD	253 BP to 224 BP (15.6% of area)
1808 AD to 1950 AD	142 BP to 0 BP (79.2% of area)



Calibration performed using Winstcal v. 6.0 adapted from: Stuiver and Reimer (*Radiocarbon* 35(1): 215-230, 1993).

National Isotope Centre, GNS Science
 PO Box 31-312 Lower Hutt, New Zealand Phone +64 4 570 4644
 Email radiocarbon@gns.cri.nz Website www.RafterRadiocarbon.co.nz



Rafter Radiocarbon

Accelerator Mass Spectrometry Result

This result for the sample submitted is for the exclusive use of the submitter. All liability whatsoever to any third party is excluded.

NZA 61174

R 40891/4

Job No: 204433

Report issued: 30 May 2016

Sample ID RV06
Description Bulk peat sample. Same unit as RV08.
Fraction dated Peat
Submitter Nicola Litchfield
GNS Science

Conventional Radiocarbon Age (years BP)	134	±	39	
$\delta^{13}\text{C}$ (‰) and type of measurement	-26.3	±	0.2	IRMS
Fraction modern	0.9835	±	0.0047	
$\Delta^{14}\text{C}$ (‰) and collection date	-24.4	±	4.7	8 Mar 2016

Measurement Comment: Uncertainty on this result is larger than normally reported. The primary standards used to normalise this result exhibited a larger scatter than normal, due to a component failure during analysis. Secondary standards - known age materials treated as unknowns - measured in the same wheel did not exhibit this larger scatter and are consistent with their consensus values. We chose to be conservative and apply the larger uncertainty implied by the primary standards.

Sample Treatment Details

13727.7mg of raw sample was received. Description of sample when received: Sample was submitted in a clear zip lock bag consisting of a single large piece of damp black peat with roots. Several reed casings were removed from the bulk of the sample. 31.0mg was subsampled and prepared by: Wet Sieve/Picking. Pretreatment description: Sample was sonicated then wet sieved to try free up the root ball. A few segments of reedy material were removed and sonicated again to remove any extra sediment. Dried the rest of the material and stored. The reeds were cleaned using tweezers and a scalpel to remove any root hairs or sediment. Chemical pretreatment was by acid, alkali, acid. Weight obtained after chemical pretreatment was 2.6mg. Carbon dioxide was generated by sealed tube combustion and 1.1mgC was obtained. Carbon dioxide was generated by sealed tube combustion and 1.1mgC was obtained. Sample carbon dioxide was converted to graphite by reduction with hydrogen over iron catalyst.

Conventional Radiocarbon Age and $\Delta^{14}\text{C}$ are reported as defined by Stuiver and Polach (*Radiocarbon* 19:355-363, 1977). $\Delta^{14}\text{C}$ is reported only if collection date was supplied and is decay corrected to that date. Fraction modern (F) is the blank corrected fraction modern normalized to $\delta^{13}\text{C}$ of -25‰, defined by Donahue et al. (*Radiocarbon*, 32(2):135-142, 1990). $\delta^{13}\text{C}$ normalization is always performed using $\delta^{13}\text{C}$ measured by AMS, thus accounting for AMS fractionation. Although not used in the ^{14}C calculations, the environmental $\delta^{13}\text{C}$ measured offline by IRMS is reported if sufficient sample material was available. The reported errors comprise statistical errors in sample and standard determinations, combined in quadrature with a system error based on the analysis of an ongoing series of measurements of standard materials. Further details of pretreatment and analysis are available on request.

National Isotope Centre, GNS Science
PO Box 31-312 Lower Hutt, New Zealand Phone +64 4 570 4644
Email radiocarbon@gns.cri.nz Website www.RafterRadiocarbon.co.nz



Rafter Radiocarbon Calibration Report

NZA 61407

R 40891/5

Report issued: 13 Jul 2016

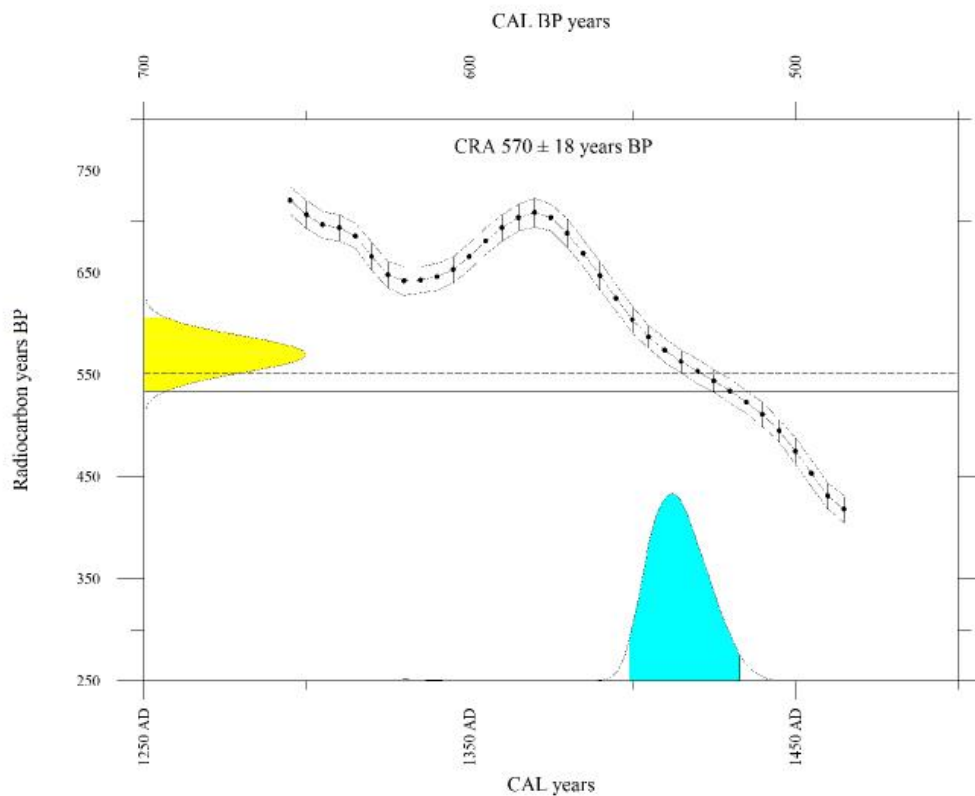
CONVENTIONAL RADIOCARBON AGE 570 ± 18 years BP

Calibrated with SHCal13 (Hogg et al., Radiocarbon 55(4):1889-1902, 2013).

CALIBRATED AGE in terms of confidence intervals

1 sigma interval is 1405 AD to 1422 AD 545 BP to 528 BP (65.6% of area)

2 sigma interval is 1399 AD to 1433 AD 551 BP to 517 BP (95.2% of area)



Calibration performed using Winstcal v. 6.0 adapted from: Stuiver and Reimer (*Radiocarbon* 35(1): 215-230, 1993).

National Isotope Centre, GNS Science
PO Box 31-312 Lower Hutt, New Zealand Phone +64 4 570 4644
Email radiocarbon@gns.cri.nz Website www.RafterRadiocarbon.co.nz



Rafter Radiocarbon

Accelerator Mass Spectrometry Result

This result for the sample submitted is for the exclusive use of the submitter. All liability whatsoever to any third party is excluded.

NZA 61407

R 40891/5

Job No: 204646

Report issued: 13 Jul 2016

Sample ID RV08
Description Bulk peat sample. Same unit as RV06.
Fraction dated Sediment
Submitter Nicola Litchfield
GNS Science

Conventional Radiocarbon Age (years BP)	570	±	18	
$\delta^{13}\text{C}$ (‰) and type of measurement	-27.6	±	0.2	IRMS
Fraction modern	0.9315	±	0.0021	
$\Delta^{14}\text{C}$ (‰) and collection date	-75.9	±	2.1	8 Mar 2016

Measurement
Comment:

Sample Treatment Details

755.5mg of raw sample was received. Description of sample when received: The sample was previously pre-treated to isolate plant fragments which were not found. Retreated for bulk sediment. <212 um was wet sieved out of the original sample. The sediment was greyish brown coloured (2.5Y 5/2 on Munsell chart). Under the microscope the sediment was predominantly grey grains with a lot of orange grains and some black grains. Some root hairs and fibres were visible. Pretreatment description: Picked out the root hairs and fibres. No other contamination was visible. Chemical pretreatment was by acid, alkali, (which was repeated), acid. Weight obtained after chemical pretreatment was 512.2mg. Carbon dioxide was generated by sealed tube combustion and 4.3mgC was obtained. Sample carbon dioxide was converted to graphite by reduction with hydrogen over iron catalyst.

Conventional Radiocarbon Age and $\Delta^{14}\text{C}$ are reported as defined by Stuiver and Polach (*Radiocarbon* 19:355-363, 1977). $\Delta^{14}\text{C}$ is reported only if collection date was supplied and is decay corrected to that date. Fraction modern (F) is the blank corrected fraction modern normalized to $\delta^{13}\text{C}$ of -25‰, defined by Donahue et al. (*Radiocarbon*, 32(2):135-142, 1990). $\delta^{13}\text{C}$ normalization is always performed using $\delta^{13}\text{C}$ measured by AMS, thus accounting for AMS fractionation. Although not used in the ^{14}C calculations, the environmental $\delta^{13}\text{C}$ measured offline by IRMS is reported if sufficient sample material was available. The reported errors comprise statistical errors in sample and standard determinations, combined in quadrature with a system error based on the analysis of an ongoing series of measurements of standard materials. Further details of pretreatment and analysis are available on request.

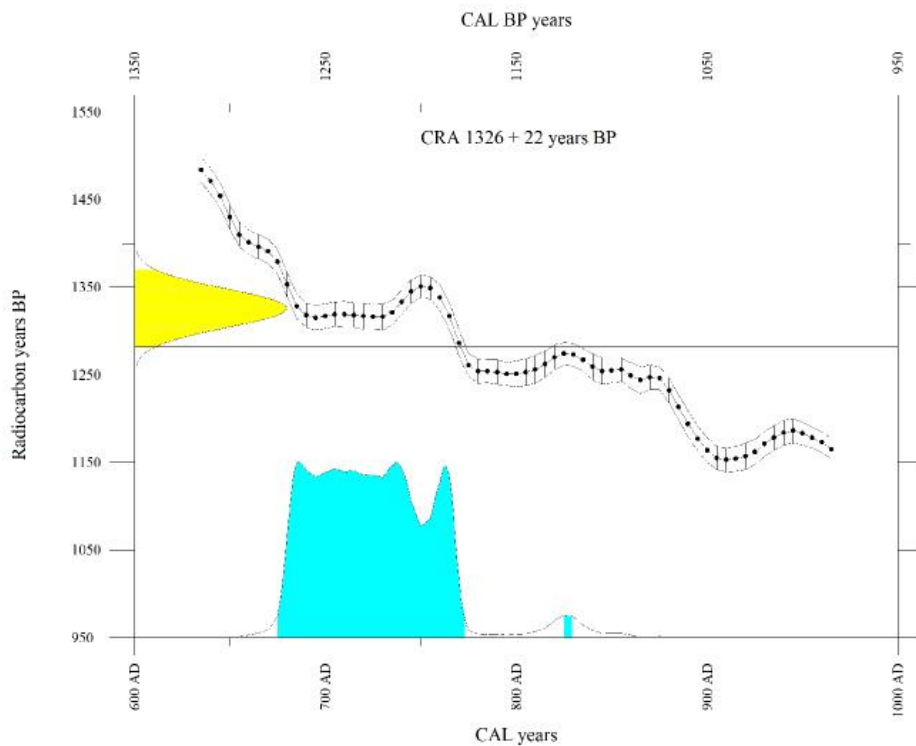
National Isotope Centre, GNS Science
PO Box 31-312 Lower Hutt, New Zealand Phone +64 4 570 4644
Email radiocarbon@gns.cri.nz Website www.RafterRadiocarbon.co.nz

CONVENTIONAL RADIOCARBON AGE 1326 ± 22 years BP

Calibrated with SHCal13 (Hogg et al., Radiocarbon 55(4):1889-1902, 2013).

CALIBRATED AGE in terms of confidence intervals

1 sigma interval is 684 AD to 742 AD	1266 BP to 1208 BP (62.6% of area)
761 AD to 766 AD	1189 BP to 1184 BP (5.5% of area)
2 sigma interval is 675 AD to 773 AD	1275 BP to 1177 BP (94.4% of area)
825 AD to 829 AD	1125 BP to 1121 BP (0.6% of area)



Calibration performed using Winscal v. 6.0 adapted from: Stuiver and Reimer (*Radiocarbon* 35(1): 215-230, 1993).

National Isotope Centre, GNS Science
 PO Box 31-312 Lower Hutt, New Zealand Phone +64 4 570 4644
 Email radiocarbon@gns.cri.nz Website www.RafterRadiocarbon.co.nz



Rafter Radiocarbon

Accelerator Mass Spectrometry Result

This result for the sample submitted is for the exclusive use of the submitter. All liability whatsoever to any third party is excluded.

NZA 61200

R 40891/2

Job No: 204431

Report issued: 13 Jun 2016

Sample ID BC01
Description Bulk peat sample. Same unit as BC02.
Fraction dated Peat
Submitter Nicola Litchfield
GNS Science

Conventional Radiocarbon Age (years BP)	1326	±	22	
$\delta^{13}\text{C}$ (‰) and type of measurement	-28.5	±	0.2	IRMS
Fraction modern	0.8479	±	0.0023	
$\Delta^{14}\text{C}$ (‰) and collection date	-158.9	±	2.3	7 Mar 2016

Measurement AMS measurement of this sample was performed at the Australian National University AMS facility. All preparation (pretreatment, combustion, graphitisation, target packing) and data reduction was performed at the Rafter facility in our usual way. The data quality meets our usual high standard, indicated by standard materials that agree with previous measurements of the same material made in our lab within one standard deviation.

Sample Treatment Details

3647.2mg of raw sample was received. The sample was submitted in a clear zip lock bag and consisted of 2 clumps of peat which was full of small pieces of organic matter; a mixture of small wood pieces, seeds, and blackened wood. There was also a lot of sediment and roots in the sample. Sample prepared by: Picking, Cut/Scrape. Pretreatment description: The clumps were broken up with a spatula and pieces of interest were removed and placed into a separate dish to be cleaned. Cleaning was done with a scalpel and tweezers to remove the sediment as best as possible which was limited by the size and fragility of the pieces. Chemical pretreatment was by acid, alkali, acid. Weight obtained after chemical pretreatment was 6.1 mg. Carbon dioxide was generated by elemental analyser combustion and 1.1 mgC was obtained. Sample carbon dioxide was converted to graphite by reduction with hydrogen over iron catalyst.

Conventional Radiocarbon Age and $\Delta^{14}\text{C}$ are reported as defined by Stuiver and Polach (*Radiocarbon* 19:355-363, 1977). $\Delta^{14}\text{C}$ is reported only if collection date was supplied and is decay corrected to that date. Fraction modern (F) is the blank corrected fraction modern normalized to $\delta^{13}\text{C}$ of -25‰, defined by Donahue et al. (*Radiocarbon*, 32(2):135-142, 1990). $\delta^{13}\text{C}$ normalization is always performed using $\delta^{13}\text{C}$ measured by AMS, thus accounting for AMS fractionation. Although not used in the ^{14}C calculations, the environmental $\delta^{13}\text{C}$ measured offline by IRMS is reported if sufficient sample material was available. The reported errors comprise statistical errors in sample and standard determinations, combined in quadrature with a system error based on the analysis of an ongoing series of measurements of standard materials. Further details of pretreatment and analysis are available on request.

National Isotope Centre, GNS Science
PO Box 31-312 Lower Hutt, New Zealand Phone +64 4 570 4644
Email radiocarbon@gns.cri.nz Website www.RafterRadiocarbon.co.nz



Rafter Radiocarbon Calibration Report

NZA 61201

R 40891/3

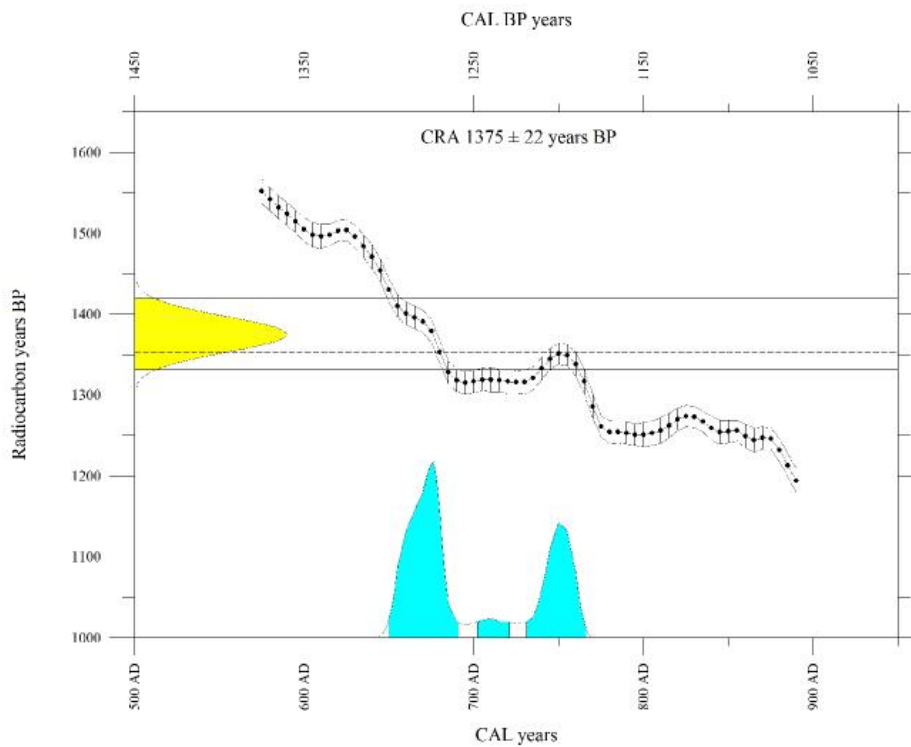
Report issued: 13 Jun 2016

CONVENTIONAL RADIOCARBON AGE 1375 ± 22 years BP

Calibrated with SHCal13 (Hogg et al., Radiocarbon 55(4):1889-1902, 2013).

CALIBRATED AGE in terms of confidence intervals

1 sigma interval is 657 AD to 683 AD	1293 BP to 1267 BP (49.3% of area)
745 AD to 758 AD	1205 BP to 1192 BP (19.4% of area)
2 sigma interval is 650 AD to 691 AD	1300 BP to 1259 BP (57.8% of area)
702 AD to 721 AD	1248 BP to 1229 BP (4.6% of area)
731 AD to 766 AD	1219 BP to 1184 BP (32.5% of area)



Calibration performed using Winscal v. 6.0 adapted from: Stuiver and Reimer (*Radiocarbon* 35(1): 215-230, 1993).

National Isotope Centre, GNS Science
 PO Box 31-312 Lower Hutt, New Zealand Phone +64 4 570 4644
 Email radiocarbon@gns.cri.nz Website www.RafterRadiocarbon.co.nz



Rafter Radiocarbon

Accelerator Mass Spectrometry Result

This result for the sample submitted is for the exclusive use of the submitter. All liability whatsoever to any third party is excluded.

NZA 61201

R 40891/3

Job No: 204432

Report issued: 13 Jun 2016

Sample ID	BC02
Description	A piece of wood in peat. Same unit as BC01.
Fraction dated	Wood
Submitter	Nicola Litchfield GNS Science

Conventional Radiocarbon Age (years BP)	1375	±	22	
$\delta^{13}\text{C}$ (‰) and type of measurement	-22.1	±	0.2	IRMS
Fraction modern	0.8427	±	0.0023	
$\Delta^{14}\text{C}$ (‰) and collection date	-164.1	±	2.3	7 Mar 2016

Measurement Comment: AMS measurement of this sample was performed at the Australian National University AMS facility. All preparation (pretreatment, combustion, graphitisation, target packing) and data reduction was performed at the Rafter facility in our usual way. The data quality meets our usual high standard, indicated by standard materials that agree with previous measurements of the same material made in our lab within one standard deviation.

Sample Treatment Details

9191.2mg of raw sample was received. Description of sample when received: sample was submitted in a clear zip lock bag. The sample consists of a single large piece of grey wood. A piece was subsampled from the outer part of the wood. 52.9mg was subsampled. Pretreatment description: a small piece was sub-sampled from the bulk of the sample using a scalpel and dried in the oven. Microscopic examination of the sample very clean wood observed sliced up into small pieces for cellulose extraction. Chemical pretreatment was by cellulose extraction. Weight obtained after chemical pretreatment was 24.4mg. Carbon dioxide was generated by elemental analyser combustion and 1mgC was obtained. Carbon dioxide was generated by elemental analyser combustion and 1mgC was obtained. Sample carbon dioxide was converted to graphite by reduction with hydrogen over iron catalyst.

Conventional Radiocarbon Age and $\Delta^{14}\text{C}$ are reported as defined by Stuiver and Polach (*Radiocarbon* 19:355-363, 1977). $\Delta^{14}\text{C}$ is reported only if collection date was supplied and is decay corrected to that date. Fraction modern (F) is the blank corrected fraction modern normalized to $\delta^{13}\text{C}$ of -25‰, defined by Donahue et al. (*Radiocarbon*, 32(2):135-142, 1990). $\delta^{13}\text{C}$ normalization is always performed using $\delta^{13}\text{C}$ measured by AMS, thus accounting for AMS fractionation. Although not used in the ^{14}C calculations, the environmental $\delta^{13}\text{C}$ measured offline by IRMS is reported if sufficient sample material was available. The reported errors comprise statistical errors in sample and standard determinations, combined in quadrature with a system error based on the analysis of an ongoing series of measurements of standard materials. Further details of pretreatment and analysis are available on request.

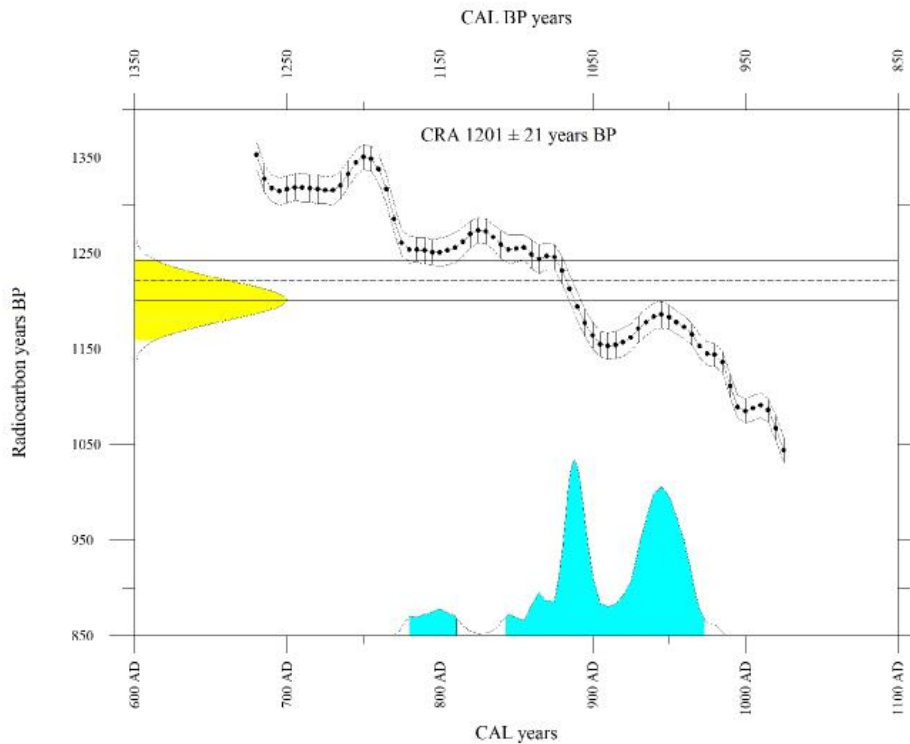
National Isotope Centre, GNS Science
PO Box 31-312 Lower Hutt, New Zealand Phone +64 4 570 4644
Email radiocarbon@gns.cri.nz Website www.RafterRadiocarbon.co.nz

CONVENTIONAL RADIOCARBON AGE 1201 ± 21 years BP

Calibrated with SHCal13 (Hogg et al., Radiocarbon 55(4):1889-1902, 2013).

CALIBRATED AGE in terms of confidence intervals

1 sigma interval is 878 AD to 901 AD	1072 BP to 1049 BP (26.5% of area)
927 AD to 965 AD	1023 BP to 985 BP (41.3% of area)
2 sigma interval is 780 AD to 811 AD	1170 BP to 1139 BP (6.4% of area)
843 AD to 973 AD	1107 BP to 977 BP (88.8% of area)



Calibration performed using Winscal v. 6.0 adapted from: Stuiver and Reimer (*Radiocarbon* 35(1): 215-230, 1993).

National Isotope Centre, GNS Science
 PO Box 31-312 Lower Hutt, New Zealand Phone +64 4 570 4644
 Email radiocarbon@gns.cri.nz Website www.RafterRadiocarbon.co.nz



Rafter Radiocarbon

Accelerator Mass Spectrometry Result

This result for the sample submitted is for the exclusive use of the submitter. All liability whatsoever to any third party is excluded.

NZA 61202

R 40891/6

Job No: 204435

Report issued: 13 Jun 2016

Sample ID RV01
Description Wood within organic silt. Same unit as RV02.
Fraction dated Wood
Submitter Nicola Litchfield
GNS Science

Conventional Radiocarbon Age (years BP)	1201	±	21	
$\delta^{13}\text{C}$ (‰) and type of measurement	-25.5	±	0.2	IRMS
Fraction modern	0.8612	±	0.0023	
$\Delta^{14}\text{C}$ (‰) and collection date	-145.7	±	2.3	8 Mar 2016

Measurement AMS measurement of this sample was performed at the Australian National University AMS facility. All preparation (pretreatment, combustion, graphitisation, target packing) and data reduction was performed at the Rafter facility in our usual way. The data quality meets our usual high standard, indicated by standard materials that agree with previous measurements of the same material made in our lab within one standard deviation.

Sample Treatment Details

1343.9mg of raw sample was received. Description of sample when received: Sample was submitted in a zip lock bag. The sample consists of a single piece of wood. The wood is coloured a ash grey with a darker coloured bark. There is a twig which is attached to the main part of the wood. The wood is quite soft as tweezers leave marks on it. 131.0mg was subsampled. Sample prepared by: Picking/Cut/Scrape. Pretreatment description: The wood was sub-sampled by taking the middle section of the main bulk. The bark was then removed and the sample was examined under the microscope, no visible contamination was seen. The wood was then cut up into small pieces. Chemical pretreatment was by cellulose extraction. Weight obtained after chemical pretreatment was 58.6mg. Carbon dioxide was generated by elemental analyser combustion and 1mgC was obtained. Carbon dioxide was generated by elemental analyser combustion and 1mgC was obtained. Sample carbon dioxide was converted to graphite by reduction with hydrogen over iron catalyst.

Conventional Radiocarbon Age and $\Delta^{14}\text{C}$ are reported as defined by Stuiver and Polach (*Radiocarbon* 19:355-363, 1977). $\Delta^{14}\text{C}$ is reported only if collection date was supplied and is decay corrected to that date. Fraction modern (F) is the blank corrected fraction modern normalized to $\delta^{13}\text{C}$ of -25‰, defined by Donahue et al. (*Radiocarbon*, 32(2):135-142, 1990). $\delta^{13}\text{C}$ normalization is always performed using $\delta^{13}\text{C}$ measured by AMS, thus accounting for AMS fractionation. Although not used in the ^{14}C calculations, the environmental $\delta^{13}\text{C}$ measured offline by IRMS is reported if sufficient sample material was available. The reported errors comprise statistical errors in sample and standard determinations, combined in quadrature with a system error based on the analysis of an ongoing series of measurements of standard materials. Further details of pretreatment and analysis are available on request.

National Isotope Centre, GNS Science
PO Box 31-312 Lower Hutt, New Zealand Phone +64 4 570 4644
Email radiocarbon@gns.cri.nz Website www.RafterRadiocarbon.co.nz



Rafter Radiocarbon Calibration Report

NZA 61203

R 40891/7

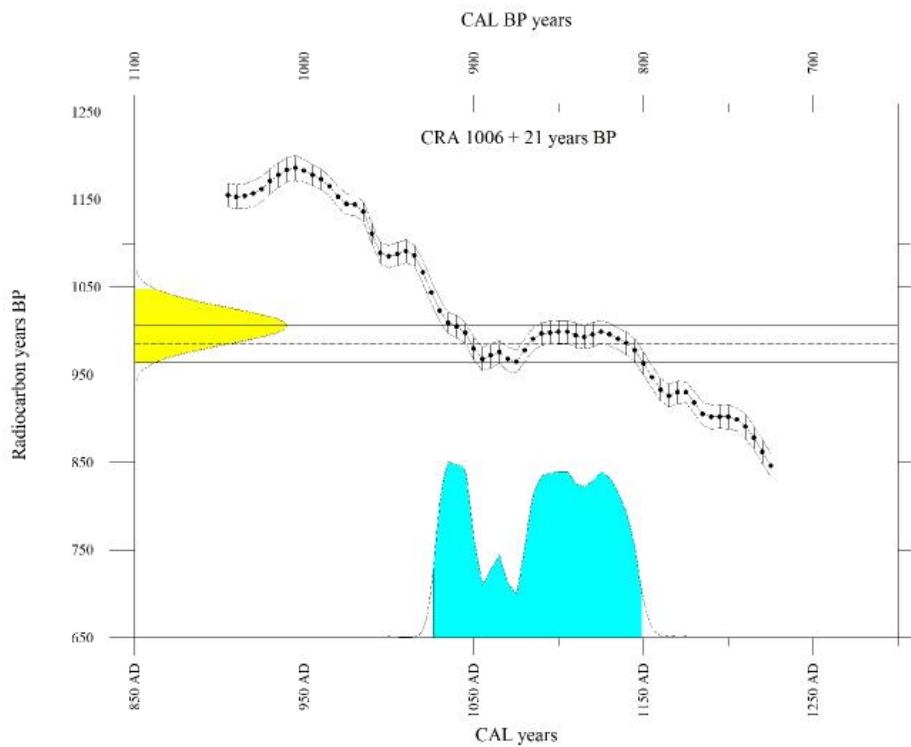
Report issued: 13 Jun 2016

CONVENTIONAL RADIOCARBON AGE 1006 ± 21 years BP

Calibrated with SHCal13 (Hogg et al., Radiocarbon 55(4):1889-1902, 2013).

CALIBRATED AGE in terms of confidence intervals

1 sigma interval is 1031 AD to 1048 AD	919 BP to 902 BP (17.7% of area)
1086 AD to 1136 AD	864 BP to 814 BP (49.6% of area)
2 sigma interval is 1026 AD to 1149 AD	924 BP to 801 BP (94.9% of area)



Calibration performed using Winscal v. 6.0 adapted from: Stuiver and Reimer (*Radiocarbon* 35(1): 215-230, 1993).

National Isotope Centre, GNS Science
 PO Box 31-312 Lower Hutt, New Zealand Phone +64 4 570 4644
 Email radiocarbon@gns.cri.nz Website www.RafterRadiocarbon.co.nz



Rafter Radiocarbon

Accelerator Mass Spectrometry Result

This result for the sample submitted is for the exclusive use of the submitter. All liability whatsoever to any third party is excluded.

NZA 61203

R 40891/7

Job No: 204436

Report issued: 13 Jun 2016

Sample ID RV02
Description Plant material within organic silt. Same unit as RV01.
Fraction dated Plant material
Submitter Nicola Litchfield
GNS Science

Conventional Radiocarbon Age (years BP)	1006	±	21	
$\delta^{13}\text{C}$ (‰) and type of measurement	-26.5	±	0.2	IRMS
Fraction modern	0.8823	±	0.0023	
$\Delta^{14}\text{C}$ (‰) and collection date	-124.8	±	2.3	8 Mar 2016

Measurement AMS measurement of this sample was performed at the Australian National University AMS facility. All preparation (pretreatment, combustion, graphitisation, target packing) and data reduction was performed at the Rafter facility in our usual way. The data quality meets our usual high standard, indicated by standard materials that agree with previous measurements of the same material made in our lab within one standard deviation.

Sample Treatment Details

55.6mg of raw sample was received. The sample was submitted in a plastic bag and consisted of single twig with its bark coated with a with pale yellow sediment. The inner core wood was a pale brown and soft. Sample prepared by: Cut/Scrape/Picking. Pretreatment description: A small section of each end and the bark was removed with a scalpel; and the inner core wood was then cleaned with a scalpel, then was sliced into pieces. Chemical pretreatment was done by acid, alkali, acid. Weight obtained after chemical pretreatment was 15.1 mg. Carbon dioxide was generated by elemental analyser combustion and 1 mgC was obtained. Sample carbon dioxide was converted to graphite by reduction with hydrogen over iron catalyst.

Conventional Radiocarbon Age and $\Delta^{14}\text{C}$ are reported as defined by Stuiver and Polach (*Radiocarbon* 19:355-363, 1977). $\Delta^{14}\text{C}$ is reported only if collection date was supplied and is decay corrected to that date. Fraction modern (F) is the blank corrected fraction modern normalized to $\delta^{13}\text{C}$ of -25‰, defined by Donahue et al. (*Radiocarbon*, 32(2):135-142, 1990). $\delta^{13}\text{C}$ normalization is always performed using $\delta^{13}\text{C}$ measured by AMS, thus accounting for AMS fractionation. Although not used in the ^{14}C calculations, the environmental $\delta^{13}\text{C}$ measured offline by IRMS is reported if sufficient sample material was available. The reported errors comprise statistical errors in sample and standard determinations, combined in quadrature with a system error based on the analysis of an ongoing series of measurements of standard materials. Further details of pretreatment and analysis are available on request.

National Isotope Centre, GNS Science
PO Box 31-312 Lower Hutt, New Zealand Phone +64 4 570 4644
Email radiocarbon@gns.cri.nz Website www.RafterRadiocarbon.co.nz



Rafter Radiocarbon Calibration Report

NZA 61663

R 40928/1

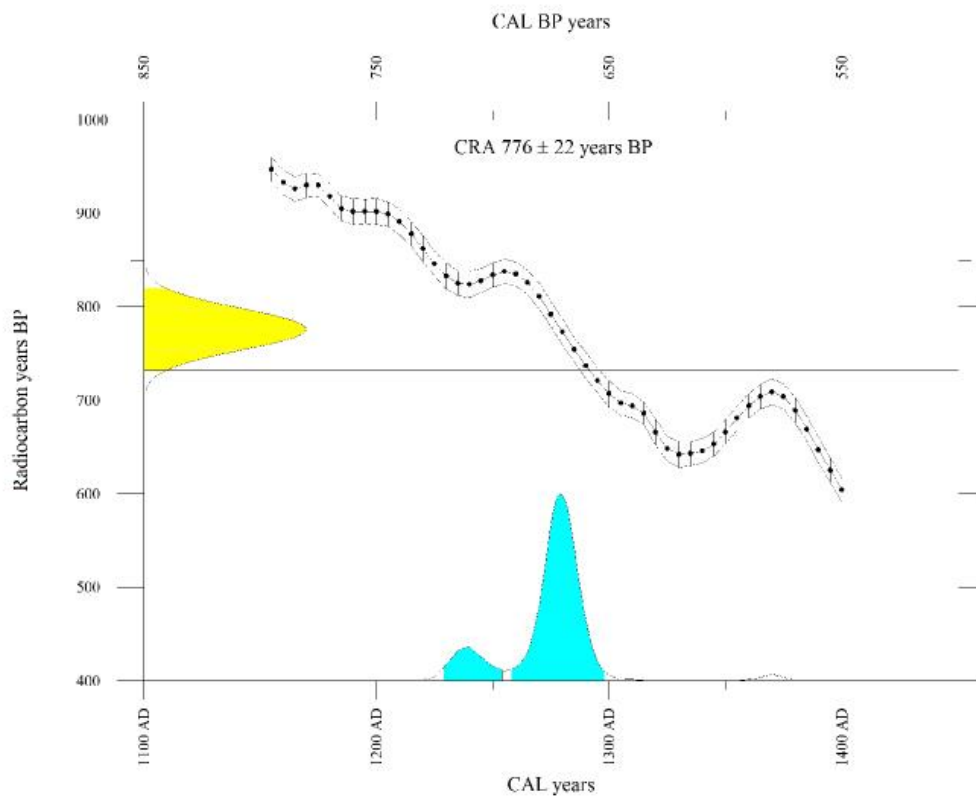
Report issued: 29 Aug 2016

CONVENTIONAL RADIOCARBON AGE 776 ± 22 years BP

Calibrated with SHCal13 (Hogg et al., Radiocarbon 55(4):1889-1902, 2013).

CALIBRATED AGE in terms of confidence intervals

1 sigma interval is 1270 AD to 1290 AD	680 BP to 660 BP (66.7% of area)
2 sigma interval is 1229 AD to 1254 AD	721 BP to 696 BP (14.0% of area)
1258 AD to 1298 AD	692 BP to 652 BP (81.0% of area)



Calibration performed using Winstcal v. 6.0 adapted from: Stuiver and Reimer (*Radiocarbon* 35(1): 215-230, 1993).

National Isotope Centre, GNS Science
 PO Box 31-312 Lower Hutt, New Zealand Phone +64 4 570 4644
 Email radiocarbon@gns.cri.nz Website www.RafterRadiocarbon.co.nz



Rafter Radiocarbon

Accelerator Mass Spectrometry Result

This result for the sample submitted is for the exclusive use of the submitter. All liability whatsoever to any third party is excluded.

NZA 61663

R 40928/1

Job No: 205305

Report issued: 29 Aug 2016

Sample ID RV09
Description Organic silt. Same unit as RV08 and RV06.
Fraction dated Soil
Submitter Nicola Litchfield
GNS Science

Conventional Radiocarbon Age (years BP)	776	±	22	
$\delta^{13}\text{C}$ (‰) and type of measurement	-27.6	±	0.2	IRMS
Fraction modern	0.9079	±	0.0025	
$\Delta^{14}\text{C}$ (‰) and collection date	-99.3	±	2.5	8 Mar 2016

Measurement
Comment:

Sample Treatment Details

59070 mg of raw sample was received. Sample was submitted in a plastic bag, and consisted of a big pile of brown sediment 5/6 7.5YR (Munsell). There were a lot of rootlets in the sediment (see pic). Under microscopic examination, revealed some orange patches in the sediment lumps with many rootlets present. Sample prepared by: Dry Sieve, Picking. Pretreatment description: Dry sieved the whole sample through 355 mic sieve, then sieved the fraction <355 mic through a 150 mic sieve. Picked out rootlets with tweezers as many as possible. The rest of fraction <150 mic were stored in a glass bottle. Chemical pretreatment was by acid, alkali, (which was repeated), acid. Weight obtained after chemical pretreatment was 892.5 mg. Carbon dioxide was generated by sealed tube combustion and 0.5 mgC was obtained. Sample carbon dioxide was converted to graphite by reduction with hydrogen over iron catalyst.

Conventional Radiocarbon Age and $\Delta^{14}\text{C}$ are reported as defined by Stuiver and Polach (*Radiocarbon* 19:355-363, 1977). $\Delta^{14}\text{C}$ is reported only if collection date was supplied and is decay corrected to that date. Fraction modern (F) is the blank corrected fraction modern normalized to $\delta^{13}\text{C}$ of -25‰, defined by Donahue et al. (*Radiocarbon*, 32(2):135-142, 1990). $\delta^{13}\text{C}$ normalization is always performed using $\delta^{13}\text{C}$ measured by AMS, thus accounting for AMS fractionation. Although not used in the ^{14}C calculations, the environmental $\delta^{13}\text{C}$ measured offline by IRMS is reported if sufficient sample material was available. The reported errors comprise statistical errors in sample and standard determinations, combined in quadrature with a system error based on the analysis of an ongoing series of measurements of standard materials. Further details of pretreatment and analysis are available on request.

National Isotope Centre, GNS Science
PO Box 31-312 Lower Hutt, New Zealand Phone +64 4 570 4644
Email radiocarbon@gns.cri.nz Website www.RafterRadiocarbon.co.nz

Luminescence Dating Technical Report

**Luminescence Dating Laboratory
School of Geography, Environment and Earth Sciences
Victoria University of Wellington
Wellington
New Zealand**

Reported by: Ms. Ningsheng Wang
Date of Issue: 16-08-2016
Contact: Room 414
Cotton Building
Victoria University of Wellington
Ph: (04) 463 6127

CONTENTS

1. Summary	3
2. Experimental Work	3
3. Results	6
4. References	8

1. SUMMARY

Five samples (Field code: BCK01, BCK02, BCK05, BCK06 and BCK07) were submitted for luminescence dating by Dr. Nicola Litchfield, GNS Science. The laboratory codes of the samples are WLL1202-WLL1206 respectively.

Due to the sample being fine material, the fine grain (4-11 μ m) preparation technique was used. The paleodose (the equivalent dose) of all samples was evaluated using the Multiple Aliquot Additive Dose method (MAAD) based on measurements of blue luminescence from the fine grain feldspar produced during infrared stimulation. The dose rate was determined on the basis of gamma spectrometry measurements.

2. EXPERIMENTAL WORK

A) Sample Preparation

Samples had their outer surfaces removed. "Fresh" sample material, that had outer surfaces removed earlier (unexposed light sample material), was treated in 10% HCl. This was carried out overnight until all carbonate was removed by the reaction. Following this treatment the sample was further reacted overnight with 10% H₂O₂ in order to remove organic matter. The next step involved 200ml CBD* solution being added to the sample for 12 hours to remove iron oxide coatings. Note, after every chemical treatment procedure distilled water was used to wash the sample several times. After chemical treatment, calgon solution (1g sodium hexametaphosphate per litre distilled water) was added to make thick slurry. This slurry was placed into an ultrasonic bath and mechanically agitated for an hour. The sample was then placed into a 1L measuring cylinder, filled with a certain amount of distilled water to separate out the 4-11 μ m grains according to Stokes' Law.

The 4-11 μ m grains were then rinsed with ethanol and acetone and a suspension of these grains were then deposited evenly onto 70 aluminium disks (diameter 9.8mm).

This removed outer scraping was then dried in an oven, milled, weighed and sealed in air tight perspex containers, then stored for at least four weeks before the gamma

spectrometer analysis. The storage time minimizes the loss of the short lived noble gas ^{222}Rn and allows ^{226}Ra to reach equilibrium with its daughters ^{214}Pb and ^{214}Bi .

A plastic cube was then filled with remaining scrapings in preparation for water content measuring.

*CBD solution: 71g sodium citrate, 8.5 g sodium bicarbonate, and 2g sodium dithionate per litre of distilled water

B) Measurements

Luminescence age was determined by two factors: the equivalent dose (D_e) and the dose rate. It involves measurements of luminescence for determination of D_e and concentrations of ^{238}U , ^{232}Th , ^{40}K and water contents (used to determine of dose rate).

Equivalent dose: obtained from the lab equivalents to the paleodose absorbed by samples during the burial time in the natural environment since their last exposure to the light.
Dose rate: amount dose received by the sample each year.

B1. Determination of Equivalent Dose (D_e)

D_e for all of these samples were obtained by using the *Multiple Aliquot Additive Dose Method (MAAD)*.

The test dose obtained from an initial test measurement was used for the MAAD. As luminescence vary between disks, all disks for MAAD need to be normalised before β irradiation. 0.1 second infrared measurements were taken before irradiation of all aliquots. Six groups (30 disks divided by five) were β irradiated up to five times of the test dose. Beta irradiation were done on the Riso TL-DA-15 $^{90}\text{Sr}/\text{Y}$ β irradiator, calibrated against ^{60}Co gamma source, SFU, Vancouver, Canada with about 3% uncertainty. Three groups (three disks per group) were α irradiated up to three times of the test dose. The α irradiation was carried out on a ^{241}Am irradiator, supplied and calibrated by ELSEC Littlemore, UK. The next step was that these 39

disks together with nine non-irradiated disks (total of 48 disks) were stored for four weeks to relax the crystal lattice after irradiation.

After storage, the 48 disks were preheated for five minutes at 230°C, then were measured using a Riso TL-DA-15 reader with infrared diodes at 880nm used to deliver a stimulated beam (30mW/cm²)at the room temperature for 100s. Blue luminescence centred about 410nm emission from feldspar was then detected by an EMI 9235QA photomultiplier fixed behind two filters consisting of a Schott BG-39 and Kopp 5-58.

Luminescence growth curve (β induced luminescence intensity versus added dose) was constructed by using the initial the 8 seconds of the shine down curves and subtracting the average of the last 20 seconds, along with the so called late light which was thought to be a mixture of background and hardly bleachable components. Extrapolation of this growth curve to the dose axis was obtained the equivalent dose D_e which was used as a paleodose. The shine plateau was checked to be flat after this manipulation.

Measurement of a-value

A similar plot for the alpha irradiated disks allows for an estimation of α efficiency, a-value (a-value is measured by comparing the luminescence induced by alpha irradiation with that induced by beta or gamma irradiation). The a-value was for dose rate calculation.

B2: Determination of Dose Rate

Dose rate consisted of two parts.

- (i) Dose rate from sample's burial environment
- (ii) Dose rate from cosmic rays.

(i) Dose rate from burial environment

Dose rate from sample's burial environment was determined by radionuclide contents of ²³⁸U, ²³²Th and ⁴⁰K, a-value and water content.

Determination of Contents of U, Th and K by Gamma spectrometry

Gamma rays produced from sample material was counted for a minimum time of 24 hours by a high resolution and broad energy gamma spectrometer. The spectra were then analysed using GENIE2000 software. The contents of U, Th and K were obtained by comparison with standard samples. The dose rate calculation was based on the activity concentration of the nuclides ^{40}K , ^{208}Tl , ^{212}Pb , ^{228}Ac , ^{214}Bi , ^{214}Pb , ^{226}Ra , using dose rate conversion factors published by Guérin, G., Mercier, N., Adamiec, G. 2011.

Measurement of Water Contents

Water content was measured as weight of water divided by dry weight of the sample taking into account a 25% uncertainty.

(ii) Dose rate from cosmic rays

Dose rate from cosmic rays were determined by the depth of sample below the surface along with its longitude, latitude and altitude, convention formula and factors published by Prescott, J.R. & Hutton, J.T. (1994).

3. RESULTS

Table 1 Cosmic dose rates

Table 2 Water contents, radionuclide contents

Table 3 a- Values, dose rates, equivalent doses and luminescence ages.

Table 1: Cosmic Dose Rates

Laboratory Code	Depth Below the Surface(m)	Cosmic Dose Rate (Gy/ka)	Field Code
WLL1202	1.5	0.1719±0.0086	BCK01
WLL1203	1.0	0.1841±0.0092	BCK02
WLL1204	2.5	0.1504±0.0075	BCK05
WLL1205	1.0	0.1841±0.0092	BCK06
WLL1206	0.75	0.1906±0.0095	BCK07

Table 2: Water Contents, Radionuclide Contents

Laboratory Code	Water Content (%)	U(ppm) from ²³⁴ Th	U(ppm) from ²²⁶ Ra, ²¹⁴ Pb, ²¹⁴ Bi	U(ppm) from ²¹⁰ Pb	Th(ppm) From ²⁰⁸ Tl, ²¹² Pb, ²²⁸ Ac	K(%)	Field Code
WLL1202	11.3	2.47±0.17	2.52±0.11	2.62±0.15	9.20±0.10	2.10±0.04	BCK01
WLL1203	19.9	2.81±0.20	3.07±0.13	2.71±0.16	10.62±0.12	1.31±0.03	BCK02
WLL1204	29.6	3.16±0.20	3.17±0.13	3.32±0.17	11.18±0.12	1.39±0.03	BCK05
WLL1205	22.4	3.06±0.19	2.89±0.12	3.13±0.16	7.41±0.08	0.96±0.02	BCK06
WLL1206	15.9	2.92±0.19	2.88±0.12	2.59±0.15	9.13±0.10	1.26±0.03	BCK07

Table 3: a-Values, Dose Rates, Equivalent Doses and Luminescence Ages

Laboratory Code	a-value	D _e (Gy)	Dose Rate(Gy/ka)	Luminescence Age(ka)	Field Code
WLL1202	0.08±0.01	54.30±6.59	4.11±0.17	13.2±1.7	BCK01
WLL1203	0.08±0.01	31.77±2.66	3.43±0.20	9.3±0.9	BCK02
WLL1204	0.08±0.02	33.84±4.82	3.25±0.28	10.4±1.7	BCK05
WLL1205	0.07±0.01	23.26±3.80	2.60±0.17	8.9±1.6	BCK06
WLL1206	0.08±0.01	33.22±1.83 33.16±0.78(SAR)	3.31±0.16	10.0±0.7 10.0±0.6(SAR)	BCK07

4. REFERENCES

Guérin, G., Mercier, N., Adamiec, G. 2011: Dose- rate conversion factors: update. *Ancient TL*, Vol.29, No.1, 5-8.

Prescott, J.R. & Hutton, J.T. 1994: Cosmic ray contributions to dose rates for luminescence and ESR dating: Large depths and long-term time variations. *Radiation Measurements*. Vol.23,Nos.2/3, 497-500.

APPENDIX 4: MODIFIED MERCALLI INTENSITY SCALE

The complete Modified Mercalli Intensity Scale of 1931 (Wood and Neumann, 1931).

- I.** Not felt except by a very few under especially favourable circumstances.
 - II.** Felt only by a few persons at rest, especially on upper floors of buildings. Delicately suspended objects may swing.
 - III.** Felt quite noticeably indoors, especially on upper floors of buildings, but many people do not recognize it as an earthquake. Standing motor cars may rock slightly. Vibration like passing of truck. Duration estimated.
 - IV.** During the day felt indoors by many, outdoors by few. At night some awakened. Dishes, windows, doors disturbed; walls made cracking sound. Sensation like heavy truck striking building. Standing motor cars rocked noticeably.
 - V.** Felt by nearly everyone; many awakened. Some dishes, windows, etc. broken; a few instances of cracked plaster; unstable objects overturned. Disturbance of trees, poles and other tall objects sometimes noticed. Pendulum clocks may stop.
 - VI.** Felt by all; many frightened and run outdoors. Some heavy furniture moved; a few instances of fallen plaster or damaged chimneys. Damage slight
 - VII.** Everybody runs outdoors. Damage negligible in buildings of good design and construction; slight to moderate in well-built ordinary structures; considerable in poorly built or badly designed structures; some chimneys broken. Noticed by persons driving motor cars.
 - VIII.** Damage slight in specially designed structures; considerable in ordinary substantial buildings with partial collapse; great in poorly built structures. Panel walls thrown out of frame structures. Fall of chimneys, factory stacks, columns, monuments, walls. Heavy furniture overturned. Sand and mud ejected in small amounts. Changes in well water. Disturbed persons driving motor cars.
 - IX.** Damage considerable in specially designed structures; well-designed frame structures thrown out of plumb; great in substantial buildings, with partial collapse. Buildings shifted off foundations. Ground cracked conspicuously, Underground pipes broken. X. Some well-built wooden structures destroyed; most masonry and frame structures destroyed with foundations; ground badly cracked. Rails bent. Landslides considerable from river banks and steep slopes. Shifted sand and mud. Water splashed (sloped) over banks.
 - XI.** Few, if any (masonry), structures remain standing. Bridges destroyed. Broad fissures in ground. Underground pipe lines completely out of service. Earth slumps and land slips in soft ground. Rails bent greatly.
 - XII.** Damage total. Waves seen on ground surfaces. Lines of sight and level distorted. Objects thrown upward into the air.
-